



FACHBEREICH PHYSIK  
BERGISCHE UNIVERSITÄT  
GESAMTHOCHSCHULE WUPPERTAL



# Low fermionic eigenmode dominance in QCD on the lattice

Dissertation  
zur Erlangung des Doktorgrades  
des Fachbereichs Physik  
der Bergischen Universität-Gesamthochschule Wuppertal

vorgelegt von

Hartmut Neff  
aus Tübingen

WUB-DIS 2001-16

Dezember 2001



FACHBEREICH PHYSIK  
BERGISCHE UNIVERSITÄT  
GESAMTHOCHSCHULE WUPPERTAL



# Low fermionic eigenmode dominance in QCD on the lattice

PhD Thesis

Hartmut Neff

WUB-DIS 2001-16

December 2001

# Abstract

The utility of a spectral approximation to the quark propagator will be demonstrated, using low-lying eigenmodes of the Hermitian Wilson-Dirac matrix,  $Q = \gamma_5 M$ . The investigation is based on a total of 400 full QCD vacuum configurations, with two degenerate flavors of dynamical Wilson fermions at  $\beta = 5.6$ , at two different sea quark masses. The spectral approach is successful in accessing both the topological charge and disconnected diagrams, as they appear in the  $\eta'$  correlation function. A suitable partial summation technique is proposed that provides sufficient saturation for  $\text{Tr } Q^{-1}$ , which is a quantity directly related to the topological charge. In the effective mass plot of the  $\eta'$  meson a consistent early plateau formation is achieved, by ground state projecting the connected piece of the propagator.

# Contents

<b>1</b>	<b>Introduction</b>	<b>5</b>
<b>I</b>	<b>BASICS</b>	<b>8</b>
<b>2</b>	<b>The Dirac Matrix</b>	<b>9</b>
2.1	The Dirac Matrix in Space-Time Continuum . . . . .	9
2.1.1	The Dirac Matrix in Minkowskian Space-Time Continuum . .	9
2.1.1.1	The Eigenmodes . . . . .	10
2.1.2	The Dirac Matrix in Euclidean Space-Time Continuum . . . .	11
2.1.2.1	The Eigenmodes . . . . .	11
2.1.2.2	The $\gamma_5$ Hermiticity Property . . . . .	13
2.1.2.3	The Hermitian Dirac Matrix . . . . .	13
2.2	The Dirac Matrix on the Lattice . . . . .	13
2.2.1	The Wilson-Dirac Matrix . . . . .	14
2.2.1.1	The Eigenmodes . . . . .	14
2.2.1.2	The Left and Right Eigenvectors . . . . .	17
2.2.1.3	Determination of the Eigenmodes for the Free Case .	18
2.2.2	The Hermitian Wilson-Dirac Matrix . . . . .	19
2.2.2.1	The Eigenmodes . . . . .	19
2.2.2.2	Determination of the Eigenmodes for the Free Case .	20

<b>II</b>	<b>THE NUMERICAL PROBLEM: How to Determine Low-Lying Eigenmodes</b>	<b>21</b>
<b>3</b>	<b>Numerical Determination of Eigenmodes</b>	<b>22</b>
3.1	The Eigenmodes of $M$ . . . . .	24
3.1.1	Even-odd Preconditioning . . . . .	28
3.1.2	Results . . . . .	29
3.1.3	Acceleration of the Arnoldi Algorithm . . . . .	30
3.2	The Eigenmodes of $Q$ . . . . .	32
3.2.1	Acceleration of the Lanczos Algorithm . . . . .	33
<b>III</b>	<b>THE PHYSICAL PROBLEM: Quantities that depend on the Quark Propagator</b>	<b>35</b>
<b>4</b>	<b>Dominance of the low-lying eigenmodes</b>	<b>36</b>
4.1	The dependence of $Q$ 's low-lying eigenvalues on $\kappa$ . . . . .	38
<b>5</b>	<b>The topological charge</b>	<b>40</b>
5.1	Introduction . . . . .	40
5.1.1	The Dirac matrix and the topological charge . . . . .	41
5.1.2	The standard approach . . . . .	42
5.1.2.1	Cooling . . . . .	42
5.1.2.2	The Stochastic Estimator (SET) . . . . .	42
5.2	The Hermitian Dirac matrix and the topological charge . . . . .	44
5.2.1	Comparison with the standard methods . . . . .	48
5.3	The non-Hermitian Dirac matrix and the topological charge . . . . .	49
5.3.1	Level crossing . . . . .	51
5.3.1.1	Level crossing and even-odd preconditioning . . . . .	52
<b>6</b>	<b>The Pion</b>	<b>57</b>
6.1	Basics for mass determinations . . . . .	57
6.1.1	Correlation functions . . . . .	57

6.1.2	Smearing . . . . .	59
6.2	The correlation function of the $\pi$ . . . . .	60
6.2.1	The standard method . . . . .	60
6.2.2	The Hermitian approach . . . . .	61
6.2.3	The non-Hermitian approach . . . . .	63
<b>7</b>	<b>The <math>\eta'</math></b>	<b>66</b>
7.1	The $U(1)$ problem . . . . .	66
7.2	The mass analysis . . . . .	67
7.2.1	The Hermitian approach . . . . .	67
7.2.2	Chiral extrapolation of the lattice $\eta'$ masses . . . . .	71
7.3	The non-Hermitian approach . . . . .	73
<b>8</b>	<b>Discussion and summary</b>	<b>81</b>
<b>A</b>	<b>Eigenvalues and Eigenvectors</b>	<b>83</b>
A.1	The Definition of Eigenmodes . . . . .	83
A.2	Left and Right Eigenvectors . . . . .	83
A.3	Normal Matrices . . . . .	84
A.4	Eigenmodes and Matrix Inversion . . . . .	85
A.5	Eigenmodes and Polynomial Transformations . . . . .	85
A.6	Spectral Decompositions . . . . .	85
<b>B</b>	<b>The Lanczos/Arnoldi Algorithm</b>	<b>87</b>
B.1	The Basic Idea . . . . .	87
B.2	The Krylov Subspace . . . . .	87
B.3	The Rayleigh Quotient or why does the Lanczos Method work . . . . .	88
B.4	Orthonormal Bases for the Krylov Subspaces . . . . .	90
B.5	The Implicitly Restarted Lanczos/Arnoldi Method . . . . .	91
<b>C</b>	<b>Gamma convention</b>	<b>94</b>
<b>D</b>	<b>Properties of the Dirac matrices</b>	<b>95</b>

# Chapter 1

## Introduction

The formulation of gauge theory on an Euclidean space-time lattice has been established as a viable framework to deal with quantum chromodynamics beyond the limitations of perturbation theory [1]. These limitations are due to the large value of the coupling constant in the low energy regime, i.e. around  $\Lambda_{QCD}$ , and thus to the breakdown of the perturbation series approximation around free fields. It is therefore the task of lattice QCD to provide unbiased (without resorting to phenomenological models) theoretical predictions of the low energy behavior of QCD, such as, for instance, the hadronic spectrum [2].

In QCD, the quark propagator (here given in Euclidean space-time)

$$S(x, y) \equiv \int dU M_U^{-1}(x, y) e^{-S_{QCD}^{eff}}, \quad (1.1)$$

where  $M$  is the Dirac matrix, is invariant under translations in space and time, i.e.

$$S(x - y) = S(x, y). \quad (1.2)$$

In lattice gauge theory one is limited to work with a finite number of gauge fields  $U_i$ , generated such that

$$\lim_{n \rightarrow \infty} \sum_{i=1}^n M_{U_i}^{-1} = \int dU M_U^{-1} e^{-S_{QCD}^{eff}} \quad (1.3)$$

holds. Consequently, the translational invariance is not satisfied (it holds only in the limit  $n \rightarrow \infty$ ). Thus a more appropriate definition of the lattice quark propagator is

$$S(\Delta x) \equiv \frac{1}{V} \sum_x \sum_{i=1}^n M_{U_i}^{-1}(x, x + \Delta x), \quad (1.4)$$

i.e. one enforces the invariance *by hand*. The right hand side of Eq. (1.4) requires the knowledge of the quark propagator from all lattice sites to all lattice sites, i.e. an *all-to-all propagator*. In this manner one extracts the full information offered by the gauge fields  $U_i$ , which is welcome since they are expensive to generate.

For the standard approach to the inverse Dirac matrix, namely solving a corresponding linear system of equations [3], the computation of Eq. (1.4) is a prohibitively demanding task. This is due to the fact that it provides a propagator from a chosen starting point only. Therefore, on typical lattice sizes, one would have to solve the linear system  $V = \mathcal{O}(10^6)$  times (i.e. for all starting points).

Fortunately, there are observables which only depend weakly on fluctuations in the vacuum gauge fields and thus do not require the all-to-all propagator. Instead, they can be well approximated by a single one at a fixed starting point. The masses of the light baryons and non-singlet mesons belong to this class of observables [2].

On the other hand, there are indeed physical quantities that show high sensitivity to gauge fluctuations, such as for instance the mixing phenomena between fermionic and glueball states [4], exotic hadronic states [5], disconnected quark loop diagrams occurring in flavor singlet matrix elements [6, 7], and the infamous  $\eta'$  propagator [8, 9, 10]. For all these cases the standard approach, i.e. solving linear systems, appears to be insufficient, in the sense that it renders results with large statistical errors. Therefore the all-to-all propagator is indispensable.

One way to overcome this hurdle is the stochastic estimator technique (SET) [11, 12, 13, 5, 14, 15, 9]. It provides estimates for each entry of  $M^{-1}$ , i.e. for each propagator, by solving linear systems of equations on stochastic sources. In recent years it has been successfully applied only to the computation of quark loops, which have a diagonal structure in spin space [6, 7, 8, 9, 10]. This is due to the fact that the diagonal elements of  $M^{-1}$  can be extracted reliably, whereas the off-diagonal elements carry large statistical errors. Thus SET is so far only helpful for a restricted class of the above described 'all-to-all' problems.

In this thesis a different approach to the all-to-all propagator is considered. The idea is to employ the spectral representation of  $M^{-1}$ ,

$$M^{-1}(x, y) = \sum_i \frac{1}{\lambda_i} |\psi_i(x)\rangle \langle \psi_i(y)|, \quad (1.5)$$

where  $(\lambda_i, |\psi_i\rangle)$  are the eigenmodes of  $M$ . Due to the weight factor  $1/\lambda$ , it is hoped that only a few low-lying eigenmodes (i.e. eigenmodes with small eigenvalues) contain the important features of long range physics, i.e. that they are dominating and thus saturate the spectral sum Eq. (1.5) [16, 17, 18]. Work in this direction has been presented in [19] (for staggered fermions) and in [20] (for an overlap action in the quenched approximation). The thesis is meant to be a feasibility study of this truncated eigenmode approach (TEA) within the SESAM parameter setting, i.e. employing Wilson fermions on a  $16^3 \times 32$  quenched lattice for  $\beta = 5.6$  and quark masses yielding an  $m_\pi/m_\rho$  ratio ranging from 0.83 to 0.57.

The observables considered here are the topological charge and the correlation functions of the  $\pi$  (flavor octet) and the  $\eta'$  (flavor singlet). The first and the last quantity depend strongly on the fluctuations in the gauge fields and thus represent prime examples for the investigation of the potential of the spectral method. The  $\pi$  is meant

to convey a more general picture of TEA's performance and thus to give clues for the assessment of its validity in other all-to-all problems.

The thesis is structured in the following way:

- In the first part the spectra of the Dirac operator in Minkowskian and Euclidean space-time continuum are compared to the one of the lattice Wilson-Dirac matrix. The mathematical basics about eigenmodes and the employed eigenmode algorithm are given in the first two chapters of the appendix.
- The second part describes how the low-lying eigenmodes of the quark propagator can be determined numerically, i.e. how the mathematical algorithm can be matched to the given eigenmode problem.
- Finally, the third part addresses the potential of the spectral method by considering the topological charge, the pion and the  $\eta'$  correlation functions.

# Part I

## BASICS

# Chapter 2

## The Dirac Matrix

In this chapter the Wilson-Dirac operator will be introduced. But it is instructive to consider first the Dirac operator both in Minkowskian and Euclidean space-time continuum. The focus will be on a comparison of the eigenmode structure of the different matrices.

### 2.1 The Dirac Matrix in Space-Time Continuum

#### 2.1.1 The Dirac Matrix in Minkowskian Space-Time Continuum

The elementary particles of quantum chromodynamics are the quarks and the gluons. The quarks are fermions, carrying a spin of  $1/2$ , whereas the gluons, the transmitters of the quark interaction, are bosonic with spin 1. The fields describing these particles are denoted by  $\psi(x, \alpha)$  and  $A_\mu(x)$  respectively, where  $x$  is the space-time index and  $\alpha = 1, 2, 3, 4$  the spin index. The gluon fields  $A_\mu(x)$  are linear combinations of the generators  $\lambda^i$ ,  $i = 1, \dots, 8$  of the group  $SU(3)$ ,  $A_\mu(x) = A_\mu^i(x)\lambda^i$ . To enable the coupling of the gluons to the quarks, the fields of the latter carry an additional 'SU(3)' index, denoted by  $a$ .

The Dirac operator  $M$  is given by

$$\begin{aligned} [M\psi](x, \alpha, a) &\equiv i\gamma^\mu(\alpha; \beta) (\partial_\mu - igA_\mu(a, b)) \psi(x, \beta, b) - m\psi(x, \alpha, a) \quad (2.1) \\ &= [(i\gamma^\mu D_\mu - m)\psi](x, \alpha, a) . \end{aligned}$$

The  $\gamma$  matrices describe the spin of the quarks,  $D_\mu \equiv \partial_\mu - igA_\mu$  are the covariant derivatives,  $m$  the quark mass and  $g$  the coupling constant.

Suppressing the indices,  $M$  takes the compact form

$$M = i\gamma^\mu D_\mu - m . \quad (2.2)$$

For massless fermions,  $m = 0$ , the Dirac matrix is denoted by  $D$

$$D = i\gamma^\mu D_\mu , \quad (2.3)$$

i.e.

$$M = D - m . \quad (2.4)$$

### 2.1.1.1 The Eigenmodes

Let the eigenmodes, i.e. the eigenvalues and eigenvectors, of  $M$  and  $D$  be denoted by  $\psi^M, \lambda^M$  and  $\psi^D, \lambda^D$  respectively:

$$M |\psi^M\rangle = \lambda^M |\psi^M\rangle , \quad (2.5)$$

$$D |\psi^D\rangle = \lambda^D |\psi^D\rangle . \quad (2.6)$$

By considering the  $\gamma$  matrices a symmetry property of these eigenmodes can be derived.

The  $\gamma$  matrices satisfy an anti-commutation relation

$$\{\gamma^\mu, \gamma^\nu\} \equiv \gamma^\mu \gamma^\nu + \gamma^\nu \gamma^\mu = 2g^{\mu\nu} , \quad (2.7)$$

with  $g^{\mu\nu} = \text{diag}(1, -1, -1, -1)$ .

Furthermore Hermitian conjugation of the  $\gamma$  matrices leads to

$$\gamma^{0\dagger} = \gamma^0 \quad (2.8)$$

$$\gamma^{k\dagger} = -\gamma^k, \quad k = 1, 2, 3. \quad (2.9)$$

Using  $\gamma^5 \equiv i\gamma^0\gamma^1\gamma^2\gamma^3$  and (2.7) it follows that

$$\{\gamma^5, \gamma^\mu\} = 0 \quad (2.10)$$

$$(\gamma^5)^2 = 1. \quad (2.11)$$

Hence the massless Dirac matrix  $D$  anti-commutes with  $\gamma^5$

$$D\gamma^5 = -\gamma^5 D . \quad (2.12)$$

$M$  itself does not inherit this property since its mass term  $m$  does not anti-commute, but commutes with  $\gamma^5$ .

It follows from (2.12) that

$$D\gamma^5 |\psi^D\rangle = -\gamma^5 D |\psi^D\rangle = -\lambda^D \gamma^5 |\psi^D\rangle. \quad (2.13)$$

Hence the eigenvalues of  $D$  come in pairs  $\lambda^D, -\lambda^D$ . The corresponding eigenvectors are  $|\psi^D\rangle$  and  $\gamma^5 |\psi^D\rangle$ .

Defining a polynomial  $p(x) = x - m$ , it follows that  $p(D) = M$  and, according to the first chapter, that the eigenmodes of  $D$  and  $M$  satisfy the relations

$$\lambda^M = \lambda^D - m , \quad (2.14)$$

$$|\psi^M\rangle = |\psi^D\rangle . \quad (2.15)$$

## 2.1.2 The Dirac Matrix in Euclidean Space-Time Continuum

Since the lattice Dirac matrix will be formulated in Euclidean space-time, it is instructive to study the eigenmodes of the Dirac matrix in Euclidean space-time continuum.

The transition from Minkowskian to Euclidean space is defined via the introduction of imaginary times,

$$x_0 \rightarrow -ix_4 . \quad (2.16)$$

The scalar product of two four-vectors then takes the form

$$x_\mu y_\mu = \sum_{i=1}^3 x_i y_i + x_4 y_4 \quad (2.17)$$

As a result the Dirac matrix transforms into (with  $A_4 = A_0$ )

$$M^E = -\gamma^0 (\partial_4 + igA_4) + i\gamma^k (\partial_k + igA_k) - m . \quad (2.18)$$

Introducing Euclidean  $\gamma$  matrices,  $\gamma_4^E \equiv \gamma^0, \gamma_i^E \equiv -i\gamma^i$ , leads to

$$M^E = -\gamma_4^E (\partial_4 + igA_4) - \gamma_k^E (\partial_k + igA_k) - m . \quad (2.19)$$

Dropping the minus sign and the index  $E$ , the Euclidean Dirac matrix reads

$$M = \gamma_\mu D_\mu + m , \quad (2.20)$$

with  $D_\mu = \partial_\mu + igA_\mu$ . The massless Euclidean Dirac matrix will be denoted by  $D$

$$D = \gamma_\mu D_\mu , \quad (2.21)$$

i.e.

$$M = D + m . \quad (2.22)$$

### 2.1.2.1 The Eigenmodes

The plus-minus symmetry of the eigenmodes of  $D$  holds in the Euclidean world as well. As in the last section the  $\gamma$  matrices have to be considered.

The  $\gamma$  matrices, as in Minkowskian space (2.7), satisfy an anti-commutation relation

$$\{\gamma_\mu, \gamma_\nu\} = 2\delta_{\mu\nu}, \quad (2.23)$$

with  $g_{\mu\nu}$  replaced by  $\delta_{\mu\nu}$ .

Again a  $\gamma_5$  matrix can be defined,  $\gamma_5 = \gamma_1\gamma_2\gamma_3\gamma_4$ . It follows easily that

$$\{\gamma_5, \gamma_\mu\} = 0, \quad (2.24)$$

$$\gamma_5^2 = 1. \quad (2.25)$$

Using the same arguments as in Minkowskian space one can show that the eigenvalues of  $D$  come in pairs  $\lambda^D, -\lambda^D$ . The corresponding eigenvectors are again  $|\psi^D\rangle$  and  $\gamma^5|\psi^D\rangle$ .

So far everything has been as in Minkowskian space. An additional characteristic of the eigenvalue distribution arises from the difference in the Hermitian conjugation properties of the  $\gamma$  matrices. In the Euclidean world they read

$$\gamma_0^\dagger = \gamma_0 \quad (2.26)$$

$$\gamma_k^\dagger = \gamma_k, \quad k = 1, 2, 3. \quad (2.27)$$

Here all four  $\gamma$  matrices are Hermitian, whereas in Minkowskian space only  $\gamma_0$  has this property.

It follows from

$$p^\mu = \left( i \frac{\partial}{\partial x_0}, -i \frac{\partial}{\partial x_k} \right) \quad (2.28)$$

that the partial derivatives are antihermitian. Since the generators of the  $SU(3)$  group  $\lambda^a$  are Hermitian (and thus  $i\lambda^a$  antihermitian), the covariant derivatives  $D_\mu$  and the massless Dirac matrix  $D$  are antihermitian as well

$$D^\dagger = -D. \quad (2.29)$$

It follows directly from

$$D^\dagger D = -DD = DD^\dagger \quad (2.30)$$

that  $D$  is normal. According to the first chapter the eigenvectors of  $D$  are orthogonal and the left and right eigenvectors are equal. Let  $U$  be the matrix that diagonalizes  $D$ ,

$$U^\dagger D U = \Lambda. \quad (2.31)$$

It follows that

$$\Lambda^\dagger = (U^\dagger D U)^\dagger = - (U^\dagger D U) = -\Lambda \quad (2.32)$$

and hence that the eigenvalues are purely imaginary.

Since  $M$  and  $D$  are again connected through a polynomial,  $p(x) = x + m$ , the eigenmodes satisfy the relation

$$\lambda^M = \lambda^D + m, \quad (2.33)$$

$$|\psi^M\rangle = |\psi^D\rangle. \quad (2.34)$$

Owing to this the eigenvectors of  $M$  are orthogonal as well. Its eigenvalues come in pairs  $m + \lambda^D$  and  $m - \lambda^D$ , or in complex notation  $(m, \lambda^D)$  and  $(m, -\lambda^D)$ .

### 2.1.2.2 The $\gamma_5$ Hermiticity Property

In the last section the following properties of  $D$  were shown

$$D^\dagger = -D, \quad (2.35)$$

$$\gamma_5 D \gamma_5 = -D. \quad (2.36)$$

It follows directly that

$$\gamma_5 D \gamma_5 = D^\dagger \quad (2.37)$$

and

$$\gamma_5 M \gamma_5 = \gamma_5 D \gamma_5 + m \gamma_5^2 = D^\dagger + m = M^\dagger \quad (2.38)$$

The last relation is called  $\gamma_5$  Hermiticity property of  $M$ . It is an important equation since it holds in identical form on the lattice as well.

### 2.1.2.3 The Hermitian Dirac Matrix

It follows from

$$\gamma_5 M \gamma_5 = M^\dagger, \quad (2.39)$$

that

$$\gamma_5 M = (\gamma_5 M)^\dagger. \quad (2.40)$$

Hence  $\gamma_5 M$  is a Hermitian matrix and thus has real eigenvalues and orthogonal eigenvectors. This is again a relation important for the lattice.

## 2.2 The Dirac Matrix on the Lattice

After the discussion of the Dirac operator in the continuum, the eigenmode structure of its lattice discretization according to Wilson, the Wilson-Dirac matrix, will be considered and compared to the continuum case. Furthermore the Hermitian Wilson-Dirac matrix will be introduced. For the free case the full spectrum for both matrices, Hermitian and non-Hermitian, will be determined.

## 2.2.1 The Wilson-Dirac Matrix

The Wilson-Dirac matrix is given by

$$\begin{aligned}
M(n, \alpha, a; m, \beta, b) &= (\hat{M} + 4)\delta(n, \alpha, a; m, \beta, b) \\
&- \frac{1}{2} \sum_{\mu=1}^4 \left[ \left( \delta(\alpha; \beta) - \gamma_{\mu}(\alpha; \beta) \right) U_{n, \mu}(a; b) \delta(n + \hat{\mu}; m) \right. \\
&\quad \left. + \left( \delta(\alpha; \beta) + \gamma_{\mu}(\alpha; \beta) \right) U_{n - \hat{\mu}, \mu}^{\dagger}(a; b) \delta(n - \hat{\mu}; m) \right].
\end{aligned} \tag{2.41}$$

where  $\hat{M}$  stands for the quark mass,  $n, m$  for the lattice sites,  $\alpha, \beta$  for the Dirac and  $a, b$  for the color indices,  $\gamma_{\mu}$  are the  $\gamma$  matrices,  $\delta$  the Kronecker delta function and  $\hat{\mu}$  denotes a unit vector in a space or time direction.

The second term, denoted by  $D$ ,

$$\begin{aligned}
D(n, \alpha, a; m, \beta, b) &= \sum_{\mu=1}^4 \left[ \left( \delta(\alpha; \beta) - \gamma_{\mu}(\alpha; \beta) \right) U_{n, \mu}(a; b) \delta(n + \hat{\mu}; m) \right. \\
&\quad \left. + \left( \delta(\alpha; \beta) + \gamma_{\mu}(\alpha; \beta) \right) U_{n - \hat{\mu}, \mu}^{\dagger}(a; b) \delta(n - \hat{\mu}; m) \right].
\end{aligned}$$

describes, due to the factors  $\delta(n + \mu; m)$  and  $\delta(n - \mu; m)$ , the interaction with  $n$ 's eight nearest lattice neighbors in space and time.

Usually the Wilson-Dirac matrix is normalized such that

$$M = I - \kappa D \tag{2.42}$$

with  $\kappa = 1/(2\hat{M} + 8)$ .

### 2.2.1.1 The Eigenmodes

Let the eigenmodes of  $M$  and  $D$  be denoted by  $(\lambda^M, |\psi^M\rangle)$  and  $(\lambda^D, |\psi^D\rangle)$  respectively

$$M |\psi^M\rangle = \lambda^M |\psi^M\rangle, \tag{2.43}$$

$$D |\psi^D\rangle = \lambda^D |\psi^D\rangle. \tag{2.44}$$

With the normalization of equation (2.42), the relation between the eigenmodes of  $M$  and  $D$  reads

$$\lambda^M = 1 - \kappa \lambda^D, \tag{2.45}$$

$$|\psi^M\rangle = |\psi^D\rangle \equiv |\psi\rangle. \tag{2.46}$$

In contrast to the Euclidean continuum case, the massless Wilson-Dirac matrix is not antihermitian

$$D^{\dagger} \neq -D. \tag{2.47}$$

The  $\gamma_5$  Hermiticity property, on the other hand, survived the discretization

$$\gamma_5 M \gamma_5 = M^\dagger , \tag{2.48}$$

$$\gamma_5 D \gamma_5 = D^\dagger . \tag{2.49}$$

This can be seen as follows:

$$\begin{aligned}
\gamma_5 D \gamma_5 &= \sum_{\mu=1}^4 \gamma_5 \left[ (1 - \gamma_\mu) U_{n,\mu} \delta(n + \hat{\mu}; m) + (1 + \gamma_\mu) U_{n-\hat{\mu},\mu}^\dagger \delta(n - \hat{\mu}; m) \right] \gamma_5 \\
&= \sum_{\mu=1}^4 \left[ (1 + \gamma_\mu) U_{n,\mu} \delta(n + \hat{\mu}; m) + (1 - \gamma_\mu) U_{n-\hat{\mu},\mu}^\dagger \delta(n - \hat{\mu}; m) \right] \\
&= \left( \sum_{\mu=1}^4 \left[ (1 + \gamma_\mu) U_{n,\mu}^\dagger \delta(n; m + \hat{\mu}) + (1 - \gamma_\mu) U_{n-\hat{\mu},\mu} \delta(n; m - \hat{\mu}) \right] \right)^\dagger \\
&= \left( \sum_{\mu=1}^4 \left[ (1 + \gamma_\mu) U_{n-\hat{\mu},\mu}^\dagger \delta(n - \hat{\mu}; m) + (1 - \gamma_\mu) U_{n,\mu} \delta(n + \hat{\mu}; m) \right] \right)^\dagger \\
&= D^\dagger .
\end{aligned} \tag{2.50}$$

Hence

$$\gamma_5 M \gamma_5 = \gamma_5 (D + m) \gamma_5 = D^\dagger + m = M^\dagger . \tag{2.51}$$

It follows from the  $\gamma_5$  Hermiticity property that the eigenvalues of  $M$  and  $D$  come in complex pairs. This can be seen as follows.

Since  $\gamma_5 M \gamma_5$  is a similarity transformation,  $M$  and  $M^\dagger$  have an identical set of eigenvalues. Let  $S$  be the matrix that diagonalizes  $M$

$$S^{-1} M S = \Lambda , \tag{2.52}$$

where  $\Lambda$  is the diagonal matrix with the eigenvalues on its diagonal. By Hermitian conjugation of (2.52) one obtains

$$S^\dagger M^\dagger S^{\dagger-1} = \Lambda^\dagger . \tag{2.53}$$

It follows directly that for each eigenvalue  $\lambda_i$  there exists a corresponding complex conjugated eigenvalue  $\lambda_i^*$ . Apparently the same holds for  $D$  as well.

The eigenvalues of  $D$  possess an additional structure, which follows from the fact that  $D$  only couples neighboring lattice sites ( $M$  itself does not have this property, owing to its identity term  $I$ ). To see how this property influences the structure of the spectrum even and odd lattice sites have to be introduced. They are defined through

- all nearest neighbors of an even site are odd,
- all nearest neighbors of an odd site are even.

The  $n$  lattice sites can be reordered, such that  $1, 2, \dots, n/2$  are even and  $n/2 + 1, n/2 + 2, \dots, n$  are odd. Let the eigenvectors in this ordering be denoted by

$$|\psi\rangle = \begin{vmatrix} \psi^e \\ \psi^o \end{vmatrix}, \tag{2.54}$$

where  $e$  and  $o$  stand for even and odd respectively. Then  $D$  takes the form

$$D = \begin{pmatrix} 0 & D_{eo} \\ D_{oe} & 0 \end{pmatrix}. \quad (2.55)$$

Squaring  $D$  leads to two invariant subspaces of dimension  $n/2$

$$D^2 = \begin{pmatrix} D_{eo}D_{oe} & 0 \\ 0 & D_{oe}D_{eo} \end{pmatrix}. \quad (2.56)$$

If an eigenmode in one of the subspaces is known, e.g.

$$D_{eo}D_{oe}|\psi^e\rangle = \lambda^2|\psi^e\rangle, \quad (2.57)$$

two eigenmodes of  $D$  can be constructed in the following way

$$\begin{aligned} D \begin{vmatrix} \pm\lambda\psi^e \\ D_{oe}\psi^e \end{vmatrix} &= \begin{pmatrix} 0 & D_{eo} \\ D_{oe} & 0 \end{pmatrix} \begin{vmatrix} \pm\lambda\psi^e \\ D_{oe}\psi^e \end{vmatrix} \\ &= \begin{vmatrix} D_{eo}D_{oe}\psi^e \\ \pm\lambda D_{oe}\psi^e \end{vmatrix} = \pm\lambda \begin{vmatrix} \pm\lambda\psi^e \\ D_{oe}\psi^e \end{vmatrix}. \end{aligned} \quad (2.58)$$

Hence the eigenvalues of  $D$  come in pairs  $\lambda$  and  $-\lambda$ . Together with the complex conjugation symmetry, one can see that the eigenvalues of  $D$  actually form quadruples  $(\lambda, -\lambda, \lambda^*, -\lambda^*)$ .

### 2.2.1.2 The Left and Right Eigenvectors

$M$  is not a normal matrix

$$MM^\dagger \neq M^\dagger M. \quad (2.59)$$

Hence  $M$ 's left and right eigenvectors are not equal. But is there a relation between them anyway?

From

$$M|\psi\rangle = \lambda|\psi\rangle, \quad (2.60)$$

it follows that

$$\langle\psi|\gamma_5 M = (M^\dagger \gamma_5 |\psi\rangle)^\dagger = (\gamma_5 M |\psi\rangle)^\dagger = (\lambda \gamma_5 |\psi\rangle)^\dagger = \lambda^* \langle\psi|\gamma_5. \quad (2.61)$$

Hence  $\langle\psi|\gamma_5$  is a left eigenvector of  $M$  with eigenvalue  $\lambda^*$ .

Let the right eigenvectors corresponding to the eigenvalues  $\lambda_i$  and  $\lambda_i^*$  be denoted by  $|\psi_i\rangle$  and  $|\psi_{\bar{i}}\rangle$ . It follows that

$$\langle\phi_i| = \langle\psi_{\bar{i}}|\gamma_5, \quad (2.62)$$

where  $\langle\phi_i|$  denotes the left eigenvector corresponding to the eigenvalue  $\lambda_i$ . With this finding the spectral representations of  $M$  and  $M^{-1}$  reads

$$M = \sum_i \lambda_i \frac{|\psi_i\rangle\langle\psi_{\bar{i}}|\gamma_5}{\langle\psi_{\bar{i}}|\gamma_5|\psi_i\rangle}, \quad (2.63)$$

$$M^{-1} = \sum_i \frac{1}{\lambda_i} \frac{|\psi_i\rangle\langle\psi_{\bar{i}}|\gamma_5}{\langle\psi_{\bar{i}}|\gamma_5|\psi_i\rangle}. \quad (2.64)$$

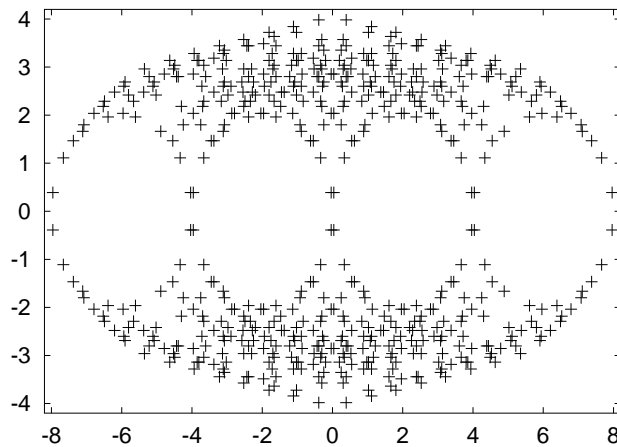


Figure 2.1: Full spectrum of  $D$  on a free  $8^3 \times 16$  lattice

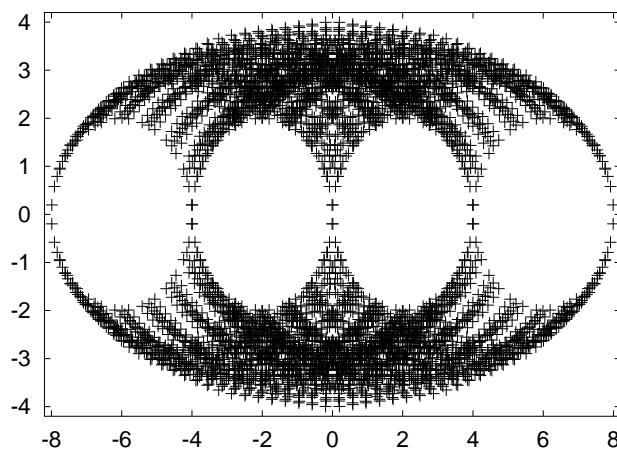


Figure 2.2: Full spectrum of  $D$  on a free  $16^3 \times 32$  lattice

### 2.2.1.3 Determination of the Eigenmodes for the Free Case

If there is no interaction between the quarks present ( $U = 1$ ), the entire set of eigenmodes of the Wilson-Dirac matrix can be determined. This is accomplished the easiest in momentum space. For these calculations the following two relations are required

$$\delta(p - k) = \frac{1}{2\pi} \sum_n e^{-in(p-k)}, \quad (2.65)$$

$$\delta(n - m) = \int_{-\pi}^{\pi} \frac{dp}{2\pi} e^{ip(n-m)}. \quad (2.66)$$

Inserting these representations of the  $\delta$  function into the free massless Wilson-Dirac

matrix  $D$  one obtains

$$\begin{aligned}
D(n; m) &= \sum_{\mu=1}^4 \left[ (1 - \gamma_{\mu})\delta(n + \hat{\mu}; m) + (1 + \gamma_{\mu})\delta(n - \hat{\mu}; m) \right] \\
&= \int_{-\pi}^{\pi} \frac{d^4 p_{\mu}}{(2\pi)^4} \left[ (1 - \gamma_{\mu})e^{-ip_{\mu}\hat{\mu}} + (1 + \gamma_{\mu})e^{ip_{\mu}\hat{\mu}} \right] e^{-ip_{\mu}(n-m)} \\
&= \int_{-\pi}^{\pi} \frac{d^4 p_{\mu}}{(2\pi)^4} \left[ e^{ip_{\mu}\hat{\mu}} + e^{-ip_{\mu}\hat{\mu}} + \gamma_{\mu} (e^{ip_{\mu}\hat{\mu}} - e^{-ip_{\mu}\hat{\mu}}) \right] e^{-ip_{\mu}(n-m)} \\
&= \int_{-\pi}^{\pi} \frac{d^4 p_{\mu}}{(2\pi)^4} \left[ 2 \cos(p_{\mu}\hat{\mu}) + 2i\gamma_{\mu} \sin(p_{\mu}\hat{\mu}) \right] e^{-ip_{\mu}(n-m)}
\end{aligned}$$

Acting with  $D$  on a vector  $\phi e^{-ik_{\mu}m}$ , where  $\phi$  depends on the spin index only, leads to

$$\begin{aligned}
D(n; m) \phi e^{-ik_{\mu}m} & \tag{2.67} \\
&= \sum_m \int_{-\pi}^{\pi} \frac{d^4 p_{\mu}}{(2\pi)^4} \left[ 2\phi \cos(p_{\mu}\hat{\mu}) + 2i\gamma_{\mu}\phi \sin(p_{\mu}\hat{\mu}) \right] e^{-ip_{\mu}n} e^{-i(k_{\mu}-p_{\mu})m} \\
&= \left[ 2 \cos(k_{\mu}\hat{\mu}) + 2i\gamma_{\mu} \sin(k_{\mu}\hat{\mu}) \right] \phi e^{-ik_{\mu}n}
\end{aligned}$$

Since the lattice is finite  $k_{\mu}$  has to satisfy certain boundary conditions, namely periodic boundary conditions in space and antiperiodic boundary conditions in time. Let the length of the lattice in space and time direction be denoted by  $s$  and  $t$ . Then

$$k_{\mu} = \frac{2\pi n_{\mu}}{s}, \quad \text{for } \mu = 1, 2, 3 \tag{2.68}$$

$$k_4 = \frac{2\pi(n_4 + \frac{1}{2})}{t}, \tag{2.69}$$

where  $n_{\mu}$ ,  $\mu = 1, \dots, 4$  are integer numbers. The eigenmodes of the free Wilson-Dirac matrix can then be found by an insertion of Eq. (2.68) and Eq. (2.69) into Eq. (2.67), followed by a diagonalization in spin space.

Two examples of such spectra are shown in Fig. (2.1) and Fig. (2.2). Their structure will be discussed later.

## 2.2.2 The Hermitian Wilson-Dirac Matrix

### 2.2.2.1 The Eigenmodes

The Hermitian Wilson-Dirac matrix is defined through a matrix multiplication between  $\gamma_5$  and  $M$

$$Q \equiv \gamma_5 M. \tag{2.70}$$

That  $Q$  is Hermitian can be seen easily

$$Q^{\dagger} = (\gamma_5 M)^{\dagger} = M^{\dagger} \gamma_5 = \gamma_5 M \gamma_5 \gamma_5 = \gamma_5 M = Q. \tag{2.71}$$

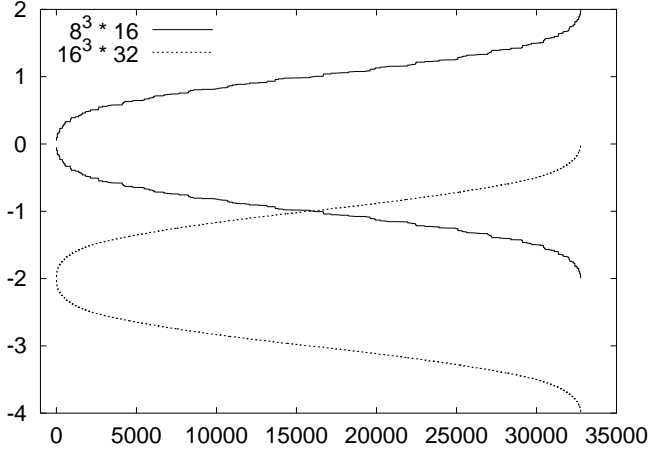


Figure 2.3: Distribution of  $Q$ 's eigenvalues. The dependence of  $\lambda_i$  on  $i$  is plotted. The upper curve corresponds to a  $8^3 \times 16$  the lower to a  $16^3 \times 32$  lattice. The latter is normalized in direction of the abscissa, such that the largest eigenvalue for both lattices have the same  $x$ -value and shifted in direction of the ordinate.

$Q$ 's eigenvalues are thus real and the eigenvectors are orthogonal.

In general  $Q$  does not possess the  $\lambda \leftrightarrow -\lambda$  symmetry. This is due to the fact that the term  $\gamma_5 I$  destroys the interaction of only nearest neighbors.

To get an idea of  $Q$ 's eigenvalue distribution, the full spectrum for the free case will be determined in the following. There the  $\lambda \leftrightarrow -\lambda$  symmetry exists.

### 2.2.2.2 Determination of the Eigenmodes for the Free Case

The calculation of  $Q$ 's eigenmodes works exactly like for  $M$ , except for an additional multiplication with  $\gamma_5$ :

$$\begin{aligned}
 & Q(n, m) \phi e^{-ik_\mu m} & (2.72) \\
 & = \sum_m \int_{-\pi}^{\pi} \frac{d^4 p_\mu}{(2\pi)^4} (\gamma_5 \phi - \kappa [2\gamma_5 \phi \cos(p_\mu) + 2i\gamma_5 \gamma_\mu \phi \sin(p_\mu)]) e^{-ip_\mu n} e^{-im(k_\mu - p_\mu)} \\
 & = (\gamma_5 \phi - \kappa [2\gamma_5 \phi \cos(k_\mu) + 2i\gamma_5 \gamma_\mu \phi \sin(k_\mu)]) e^{-ik_\mu n}
 \end{aligned}$$

To obtain the eigenmodes the last equation has to be diagonalized in spin space.

Two examples are given in Fig. (2.3). There the dependence of  $\lambda_i$  on  $i$  on a  $8^3 \times 16$  (rough curve) and a  $16^3 \times 32$  (smooth curve) lattice is shown. The latter is normalized in direction of the abscissa, such that the largest eigenvalue for both lattices have the same  $x$ -value and shifted in the direction of the ordinate.

## Part II

# **THE NUMERICAL PROBLEM: How to Determine Low-Lying Eigenmodes**

# Chapter 3

## Numerical Determination of Eigenmodes

In this chapter it will be shown how the physically most important eigenmodes of the Wilson-Dirac matrix  $M$  and the Hermitian Wilson-Dirac matrix  $Q$  can be calculated. The respective matrices were given in the sections (2.2.1) and (2.2.2). For the free case ( $U = 1$ ) the eigenmodes for both cases could be calculated through a Fourier transformation to momentum space. This method fails when the interaction is turned on and the eigenmodes are then only accessible through numerical calculations.

*What kind of algorithms are appropriate for this numerical calculations?*

On typical lattice sizes the dimension of the Wilson-Dirac matrix is of order  $10^6$ . Therefore it is impossible to employ algorithms that determine the whole set of eigenmodes, such as the  $QR$  algorithm [21]. Since in this case only storing all the eigenvectors would require a memory size of the order of TBytes, not mentioning the time that would be needed for their computation.

Hence a different strategy is required. One has to employ an algorithm that is capable of determining only a few eigenmodes. For this purpose the Lanczos/Arnoldi algorithm [22] is used here.

*How does the Lanczos/Arnoldi algorithm work in principle?*

The basic mathematical ingredient of the Lanczos/Arnoldi algorithm are the Krylov subspaces  $\mathcal{K}(A, q, k)$ . Considering a matrix  $A$  and a starting vector  $q$ ,  $\mathcal{K}(A, q, k)$  is defined through

$$\mathcal{K}(A, q, k) = \text{span}\{q, Aq, A^2q, \dots, A^{k-1}q\} . \quad (3.1)$$

$A$  is orthogonally projected on the subspaces  $\mathcal{K}(A, q, k)$ , resulting in small matrices  $T_k$  of dimension  $k$ . The crucial property of the Krylov subspaces is that with increasing  $k$ , the eigenmodes of  $T_k$  become increasingly better estimates for the extremal eigenmodes of  $A$ , i.e. for the eigenmodes of largest and/or smallest modulus. In

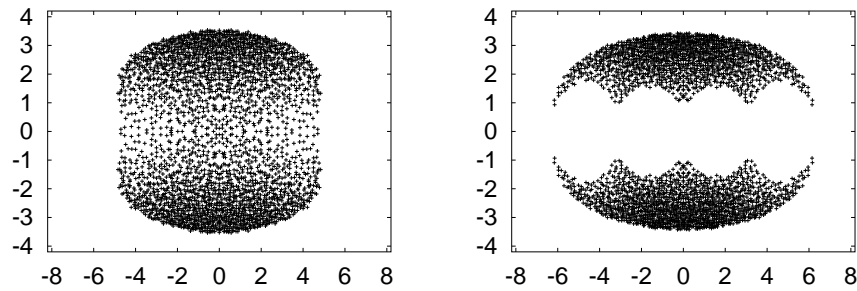


Figure 3.1: Full spectrum of  $D$  on a quenched  $4^4$  lattice for  $\beta = 5.0$  (left) and  $\beta = 6.0$  (right)

general the estimates for the extremal eigenmodes of  $A$  converge fast, turning this algorithm into being practicable.

The memory size of the computer used limits the dimension of the Krylov subspaces. This problem can be eluded by restarting the iteration once the critical Krylov subspace dimension is reached. For this purpose a new starting vector is created, based on the estimates for the searched for eigenmodes emerged hitherto. This means that the new starting vector will be closer to the subspace spanned by the searched for eigenvectors than the old one. Like this the convergence of the iteration can even be guided to eigenmodes other than the ones of largest/smallest modulus.

There exists a clever variant of this procedure, called the implicitly restarted Lanczos/Arnoldi method (IRAM). Lets assume that  $k$  eigenmodes are wanted and that the dimension of the Krylov subspace before restarting is  $l > k$ . Based on the eigenmodes of the small matrix  $T_k$  a new starting vector can be constructed. The difference to normal restarting is that this construction is done such that the Krylov subspace of dimension  $k$ , corresponding to this new starting vector, is directly obtained, without further matrix vector multiplications involving  $A$ .

In other words, in a first step the dimension of the Krylov subspaces is increased from 1 to  $l$ . In the restarting step a Krylov subspace of dimension  $k$  is constructed, which then has to undergo the dimension increasing step again, and so on. Thus each implicit restarting step saves  $k$  matrix vector multiplications compared to normal restarting.

More about the Lanczos/Arnoldi algorithm and implicit restarting can be found in appendix(B).

An important argument for the use of the Lanczos/Arnoldi algorithm for this kind of calculations is that there exists a parallel IRAM software package, called PARPACK. It provides all the necessary IRAM routines, apart from the user defined matrix vector multiplication [22].

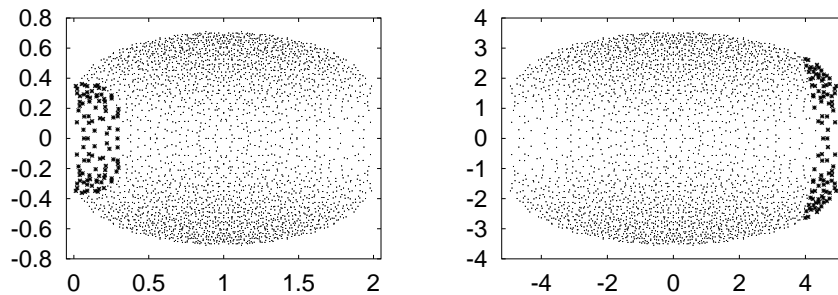


Figure 3.2: 100 eigenmodes (fat points), determined on a quenched  $4^4$  lattice for  $\beta = 5.0$ . Left: the Arnoldi algorithm determined the eigenmodes of smallest modulus of  $M$  (with  $\kappa = 0.2$ ), right: eigenmodes of largest modulus of  $D + 5I$ . Both sets of eigenmodes were determined without even-odd preconditioning.

### 3.1 The Eigenmodes of $M$

In this section a polynomial transformation for non-hermitian matrices will be presented, which provides access to wedge-shaped spectral windows. For the Wilson-Dirac matrix this procedure not only allows the determination of the physically interesting low-lying eigenmodes but also provides a substantial acceleration of the Arnoldi algorithm.

In Fig. (2.1) and Fig. (2.2) the spectra of the Wilson-Dirac matrix for the free case on lattices of different sizes were shown.

*How does the interaction influence the spectrum?*

The entire spectrum of the interacting Wilson-Dirac matrix can only be determined on small lattices. Therefore a  $4^4$  lattice is chosen to convey a qualitative idea of how the interaction influences the eigenvalue distribution. Fig. (3.1) shows spectra on a quenched  $4^4$  lattice for two different  $\beta$  values. It can be seen that the elliptic shape persists for both cases. For the smaller  $\beta$  value however the eigenvalues populate the circles that are empty when no interaction is present. Thus the distinction between doublers and physical eigenvalues becomes washed out for small  $\beta$ s.

This statements hold on larger lattices as well (as can be seen by calculating appropriate parts of the spectrum), only the density of the eigenvalues increase.

*Which is the physically interesting part of the spectrum?*

The large eigenvalues of  $M$  correspond to the doublers and thus do not contain physical information, but only  $a$ -dependent lattice artefacts. This means that the small eigenmodes are physical and therefore of interest. Apart from this general statement, the observables to be described by the eigenmodes determine the required part of the spectrum. In some cases the eigenvalues of smallest modulus are expected to contain the relevant information, as for instance for the spectral representation of the quark propagator. Other cases constrain the imaginary part of the eigenvalues,

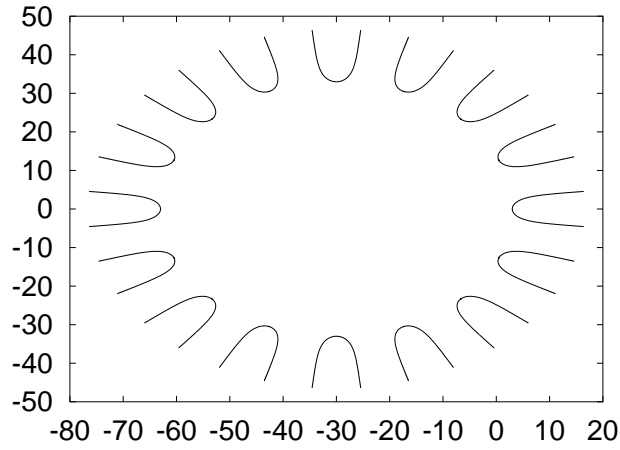


Figure 3.3: Spectral windows of sensitivity with  $n = 16$ ,  $\sigma = 30$  and  $c = (\sigma + 3)^n$ .

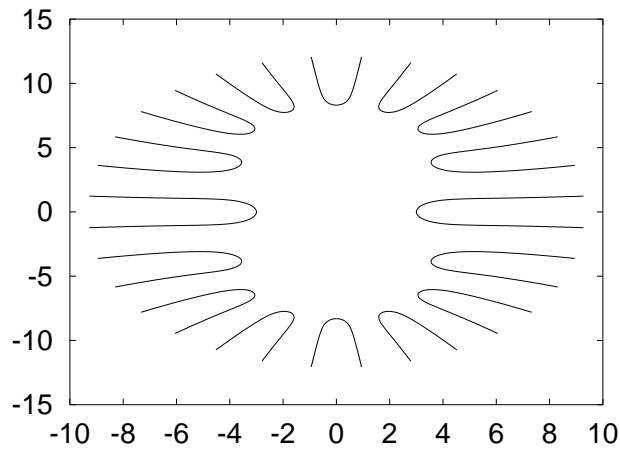


Figure 3.4: Spectral windows of sensitivity for even-odd preconditioning, with  $n = 8$ ,  $\sigma = 30$  and  $c = (\sigma + 3)^n$ .

i.e. here only the small eigenvalues close to the real axis are needed [23, 24, 25, 26, 27]. In short, those types of spectral regions will be referred to as the low-lying eigenmodes.

*Which part of the spectrum is accessible through the Arnoldi algorithm?*

The straight forward approach to the described eigenproblem is to ask the algorithm for the eigenmodes of smallest modulus. This immediately provides the searched for part of the spectrum, see the left frame in Fig. (3.2). By introducing shifts along the real axis ( $M + \sigma I$ ), the part of the spectrum to be found by the algorithm can be influenced. The term  $\sigma I$  represents a simple shift of the eigenvalues,  $\lambda^M \rightarrow \lambda^M + \sigma$ .

The numerical calculations however show that the Arnoldi algorithm converges much faster when determining the eigenmodes of largest modulus or largest real part

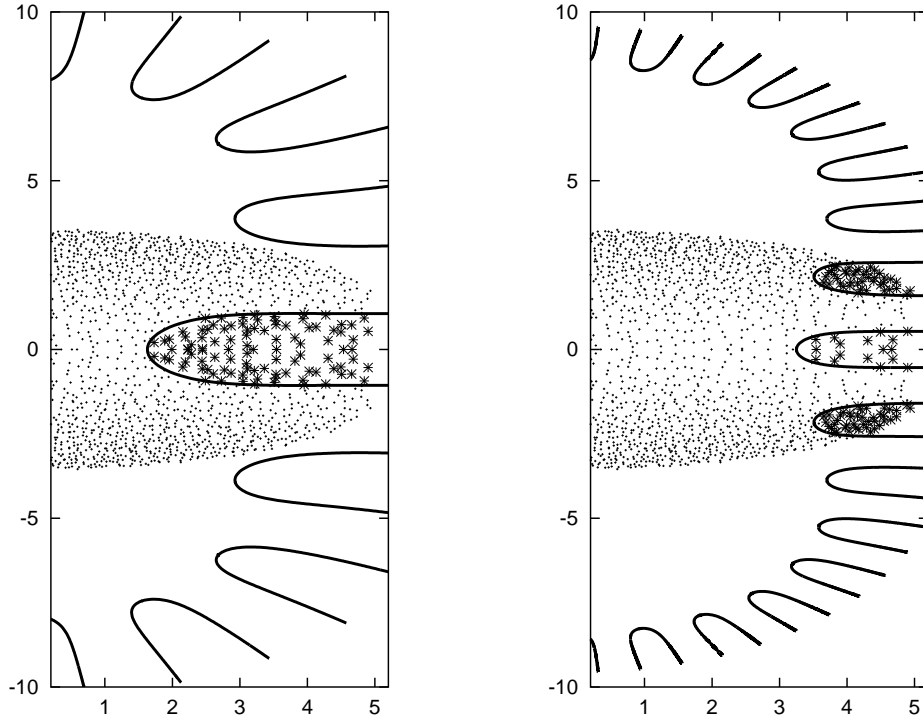


Figure 3.5: 100 eigenvalues (fat points) on an even-odd preconditioned quenched  $4^4$  lattice for  $\beta = 5.0$ . Left:  $p_{\sigma,n}$  with  $\sigma = 30$  and  $n = 8$ , right:  $p_{\sigma,n}$  with  $\sigma = 30$  and  $n = 16$ .

instead, where on a  $4^4$  ( $8^4$ ) lattice a gain factor of 2(5) was found.

This empirical fact can easily be exploited by calculating the eigenmodes of largest modulus of  $D + \sigma I$  (where  $M = I - \kappa D$ ).  $\sigma$  has to be chosen large enough ( $\sigma \geq 4$  will do) such that the eigenvalues at the right end of  $D$ 's spectrum become the ones of largest modulus.

The disadvantage of this procedure is that the eigenmodes found by the algorithm are not so close to the real axis anymore, i.e. they are not as 'low-lying' as before (see the right frame in Fig. (3.2)). This problem can be cured by a modified approach. For this the algorithm is asked to determine *large* eigenmodes of a polynomial of  $D$ ,  $p(D)$ , instead. It is shown in section (A.5) that then the eigenmodes of  $D$  can be easily achieved from the ones of  $p(D)$ .

The suggested procedure is then the following:

Determine the eigenmodes of *largest real part* of

$$p_{\sigma,n}(D) = (D + \sigma I)^n . \quad (3.2)$$

Applying the polynomial  $p_{\sigma,n}$  to  $D$  instead of  $M$  is only a matter of notation. One could as well work with  $p_{\sigma,n}(M)$ .

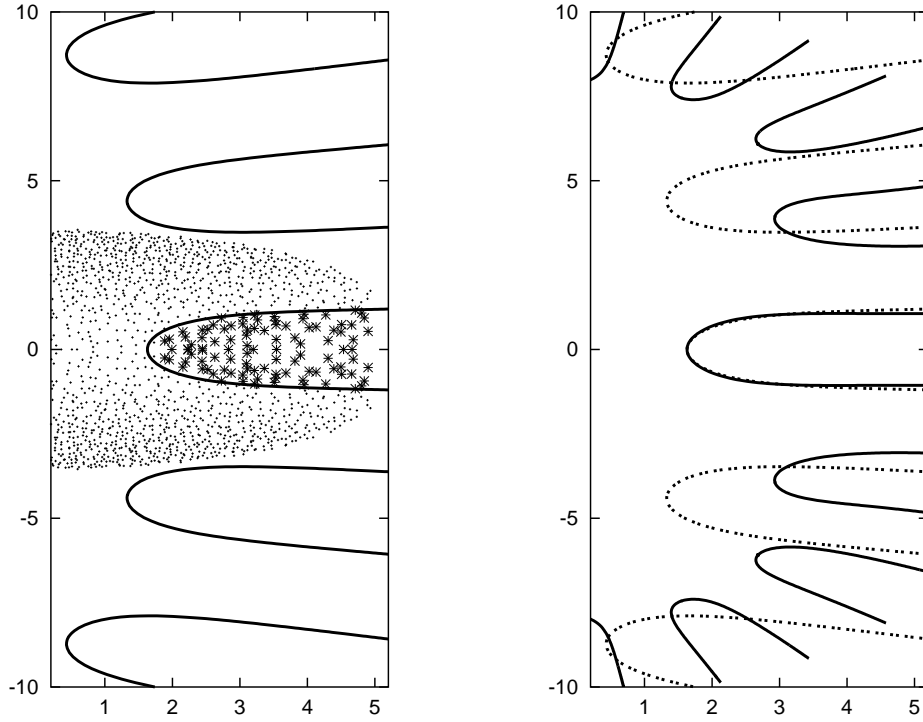


Figure 3.6: Left: 100 eigenvalues (fat points) on a quenched  $4^4$  lattice for  $\beta = 5.0$ , without even-odd preconditioning,  $p_{\sigma,n}$  with  $\sigma = 30$  and  $n = 46$ , right: comparison of  $p_{30,46}$  (full lines) with  $p_{30,8}$  for the even-odd preconditioned matrix.

The eigenmodes of largest real part are found through an appropriate sorting in the restarting routine. The convergence of a search for the eigenmodes of largest modulus and the ones of largest real part is comparable.

*Which part of the spectrum is amenable through this polynomial transformation  $p_{\sigma,n}(D)$ ?*

The spectral windows amenable to  $p_{\sigma,n}$  can be identified by determining the complex numbers that achieve, under the polynomial  $p_{\sigma,n}$ , a real part larger than a chosen number  $c$ , i.e. which are mapped into

$$S = \{a \in \mathbb{C} \mid \text{real}(p_{\sigma,n}(a)) \geq c\}, \quad (3.3)$$

where  $c$  depends on the number of eigenmodes to be determined. This is illustrated in Fig. (3.3). The curves enclose the complex numbers belonging to  $S$ , with their shape being fixed by  $\sigma$  and  $n$ . With respect to the eigenmode algorithm,  $S$  represents the windows of sensitivity, i.e. the algorithm is capable to find eigenmodes lying inside the wedge-like regions  $S$ .

Let the curves be numbered counterclockwise from 0 to  $n - 1$ , starting with the curve cutting the real axis on the right side. The curve 0 is the one to be employed. This means that the exponent  $n$  and the shift  $\sigma$  have to be chosen such that only this curve cuts the spectrum. In general  $n$  should not be chosen too large and  $\sigma$  not

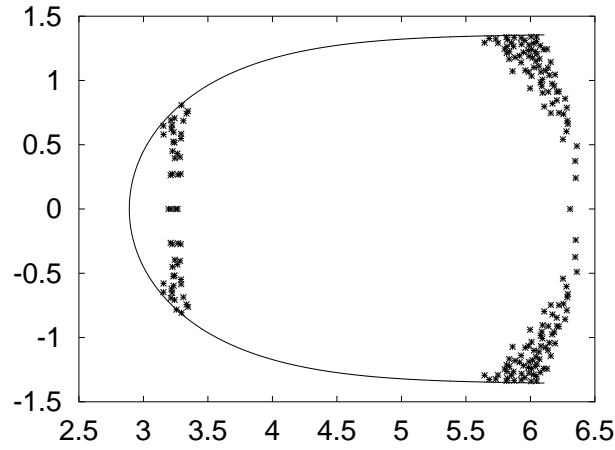


Figure 3.7: 200 eigenvalues on a  $8^4$ ,  $\beta = 6.0$ ,  $\sigma = 50$ ,  $n = 8$ , with even-odd preconditioning.

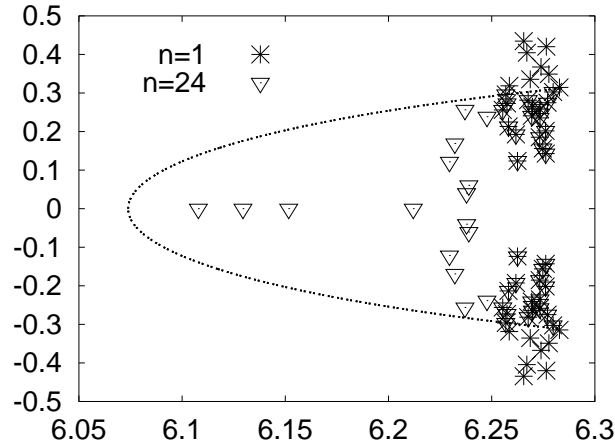


Figure 3.8: 50 eigenvalues on a  $16^3 \times 32$ ,  $\beta = 5.6$ ,  $\sigma = 50$ , with even-odd preconditioning.

too small, since then the curves 1 and  $n - 1$  could cut the spectrum as well. Then unwanted eigenmodes with large imaginary part would be found by the algorithm.

The shape of the curve 0 shows that indeed the low-lying eigenmodes, i.e. the ones close to the real axis, are amenable through this algorithm.

### 3.1.1 Even-odd Preconditioning

The situation is slightly different when using the even-odd preconditioned matrix  $D_{eo}D_{oe}$  (see section (2)). There the matrix is squared before applying the shift and the subsequent exponentiation. This results in different shapes of the windows of sensitivity. This can be seen in Fig. (3.4). That the curves are now symmetric to

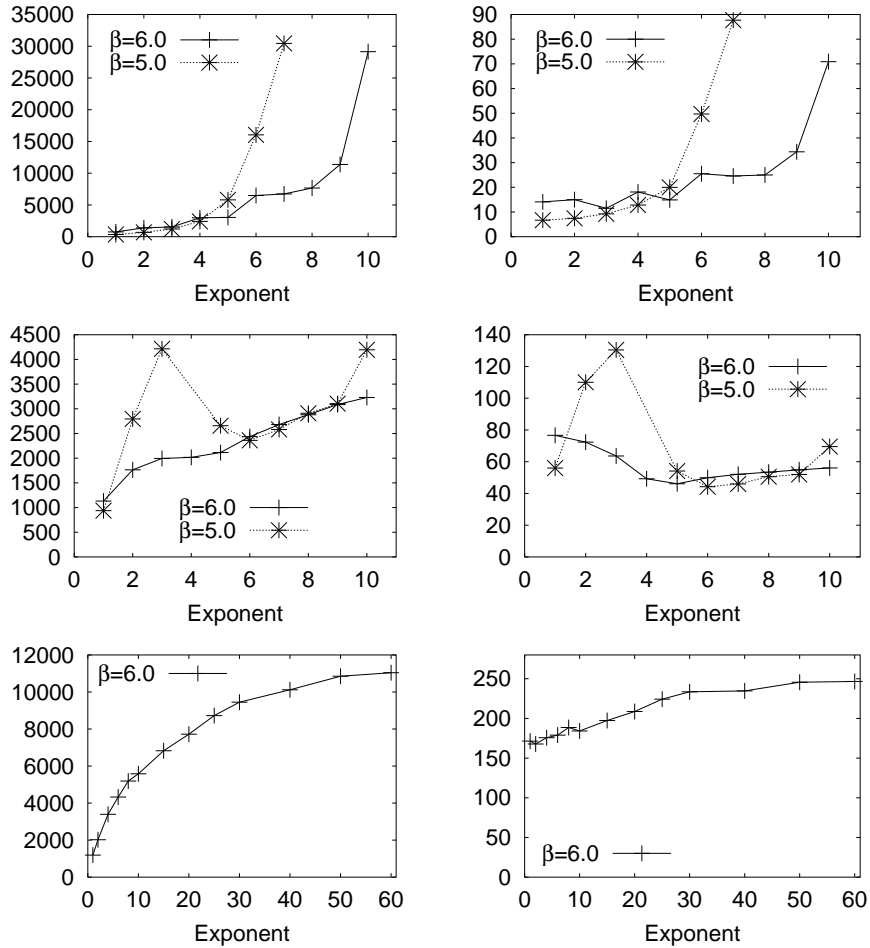


Figure 3.9: Dependence of the number of matrix vector multiplications (left frames) and the CPU time (right frames) on the exponent  $n$ . 50 eigenmodes with  $\sigma = 50$  were determined. From top to bottom the results for a quenched  $4^4$  lattice, a quenched  $8^4$  lattice without and with clover improvement.

the origin is due to the fact that from an eigenvector of  $D_{eo}D_{oe}$  corresponding to the eigenvalue  $\lambda^2$ , two eigenvectors of  $D$  corresponding to  $\lambda$  and  $-\lambda$  can be constructed.

### 3.1.2 Results

Fig. (3.5) and Fig. (3.6) illustrate the above. The first three frames show that the determined eigenvalues are indeed enclosed by the curves defined through  $S$  and that they are close to the real axis, i.e. low-lying.

Furthermore the right frame of Fig. (3.5) illustrates that with too large an exponent  $n$ , physically uninteresting eigenmodes with large imaginary parts will be computed by the algorithm.

Finally the right frame of Fig. (3.6) demonstrates that preconditioning can help to

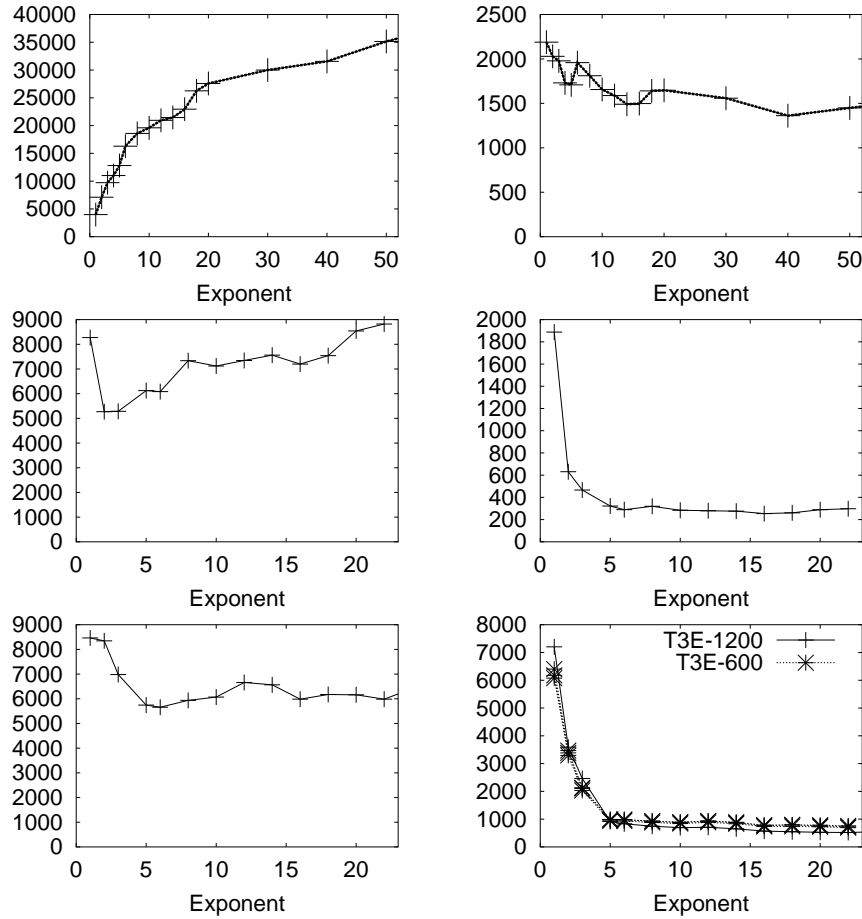


Figure 3.10: Dependence of the number of matrix vector multiplications (left frames) and the CPU time (right frames) on the exponent  $n$ . 50 eigenmodes with  $\sigma = 50$  were determined. From top to bottom the results for a quenched  $12^3 \times 24$  ( $\beta = 5.7$ ), with and without clover improvement, and for a full QCD  $16^3 \times 32$  lattice ( $\beta = 5.6$ ) are displayed.

substantially reduce  $n$  without spoiling the interesting window of sensitivity, as the curves cutting the real axis nearly coincide.

In Fig. (3.8) further such examples are presented. One shows a  $8^4$ -lattice, where the doublers can be seen, the other, on a full QCD  $16^3 \times 32$  lattice, compares the eigenvalues obtained for the exponents  $n = 1$  and  $n = 24$ . The plotted curves enclose the regions of the complex plane that were searched for eigenvalues, i.e. inside the curves all eigenvalues are captured.

### 3.1.3 Acceleration of the Arnoldi Algorithm

One might suspect that the polynomial transformation  $p_{\sigma,n}(D)$  goes along with a polynomial increase of the execution time due to additional matrix vector multi-

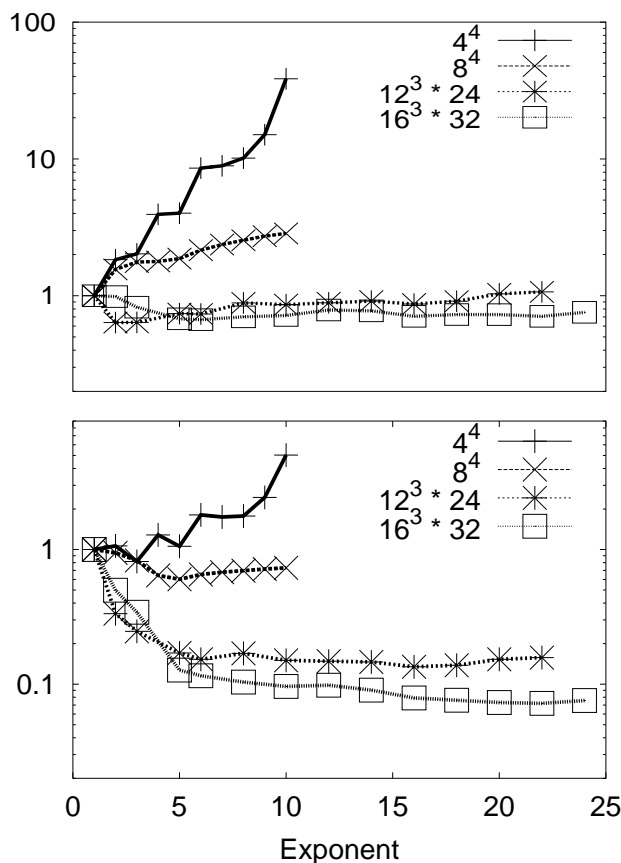


Figure 3.11: Dependence of the number of matrix vector multiplications (upper frame) and the CPU time (lower frame) on the exponent  $n$  (normalized such that for  $n = 1$  all values are equal to 1). 50 eigenmodes of the even-odd preconditioned Wilson-Dirac matrix were determined with  $\sigma = 50$ . The  $4^4$ ,  $8^4$  and  $12^3 \times 24$  lattices are quenched, whereas the  $16^3 \times 32$  lattice is unquenched.

plications. That this is not so can be seen, both for the even-odd preconditioned and the clover improvement [28, 29, 30, 31] Wilson-Dirac matrices in Fig. (3.9), Fig. (3.10) and Fig. (3.11). There the dependence of the number of matrix vector multiplications and the CPU time, required to determine 50 eigenmodes, on the exponent  $n$  are displayed.<sup>1</sup>

For the even-odd preconditioned Wilson-Dirac matrix one can see that the run time increases strongly on the  $4^4$  and is almost stable on the  $8^4$  lattice, whereas a dramatic decrease is found on the realistic lattice sizes  $12^3 \times 24$  and  $16^3 \times 32$ . For the last two lattices the CRAY T3E-1200 found an acceleration factor of 8, whereas the CRAY T3E-600 produced a gain factor of 9 and 14, respectively.

For the clover improved Wilson-Dirac matrix this systematics seems to be delayed. On the  $8^4$  lattice an increase in computing time is detected, whereas on the  $12^3 \times 24$  an acceleration factor of 1.6 was found.

<sup>1</sup>Surprisingly in some cases only for  $n = 4$  no convergence was found.

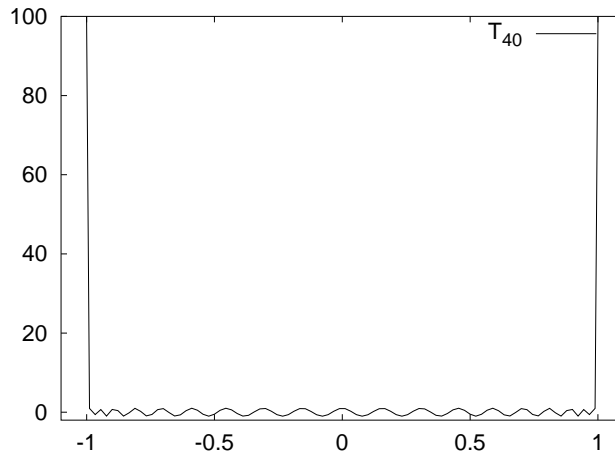


Figure 3.12: Chebyshev polynomial of order 40.

Furthermore the results indicate that the factor of acceleration grows with the size of the lattice.

*Why does the polynomial transformation accelerate the algorithm?*

At first one might expect that through the polynomial transformation the density of the eigenvalues is decreased. This would explain the acceleration, since the convergence is sensitive to this quantity. But if that is the correct explanation, the number of matrix vector multiplications would be decreasing as well. Since this is not always the case (as can be seen in the left frames of Fig. (3.9) and Fig. (3.10)), a different mechanism must be at work. Taking a look at the time spent in the Arnoldi subroutines for different exponents  $n$  immediately provides the answer: When employing the polynomial  $p_{\sigma,n}$  one has to enter the Arnoldi subroutines less often, since in one Arnoldi step one performs  $n$  matrix vector multiplications instead of only one, and thus saves the time normally spent in the Arnoldi routines. This means that for large  $n$ , the computing time is almost exclusively used for the matrix vector multiplications. Hence the optimal choice of polynomial is met, if just one Arnoldi factorization has to be performed, i.e. if the Krylov subspace dimension is increased in one stroke from 1 to  $l$ .

## 3.2 The Eigenmodes of $Q$

$Q$  is a Hermitian matrix and thus has real eigenvalues and orthogonal eigenvectors. This allows for a natural ordering of the eigenvalues and thus for a straight forward definition of low-lying eigenmodes. Again a polynomial transformation (Chebyshev polynomials) is employed to accelerate the convergence of the Arnoldi algorithm.

*Which is the physically interesting part of  $Q$ 's spectrum?*

As in the non-Hermitian case, the low-lying eigenmodes are expected to contain

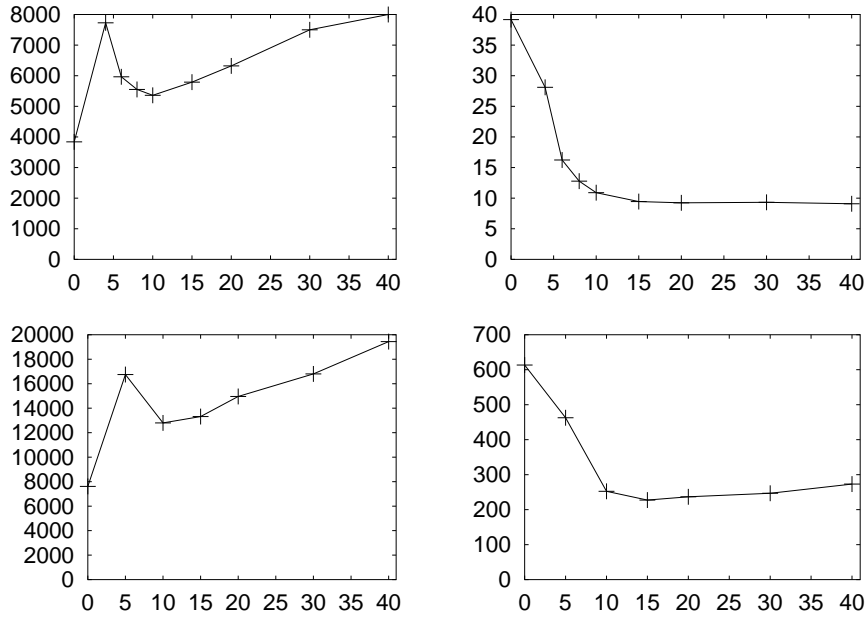


Figure 3.13: Dependence of the number of matrix vector multiplications (left frames) and the runtime (right frames) on the order of the Chebyshev polynomials. 50 eigenmodes of  $Q$  on a quenched  $4^4$  lattice for  $\beta = 5.0$  (upper frame) and on a quenched  $8^4$  for  $\beta = 6.0$  (lower frame) were determined.

the relevant physical information. But in contrast to the non-Hermitian case, the definition of low-lying eigenmodes of  $Q$  is non-ambiguous, since real eigenvalues allow for a natural ordering  $|\lambda_1| \leq |\lambda_2| \leq \dots \leq |\lambda_n|$ . In the spirit of long range physics, the eigenmodes closest to the origin are of interest.

The eigenmodes of  $Q$  are determined by use of the Lanczos algorithm. In contrast to the non-Hermitian case, the low-lying eigenmodes of  $Q$  are interior, i.e. inside the spectrum. But since the Lanczos algorithm only works efficiently when calculating eigenvalues on the surface of the spectrum, here around  $\lambda_{min}$  and  $\lambda_{max}$ , a preparational polynomial transformation  $p$  of  $Q$  has to be executed such that the low-lying eigenmodes of  $Q$  become exterior eigenmodes of  $p(Q)$ . This can readily be achieved through

$$p : Q \rightarrow p(Q) = Q^2, \quad (3.4)$$

where the eigenvalues on the left end of  $Q^2$ 's spectrum correspond to the low-lying eigenvalues of  $Q$ .

### 3.2.1 Acceleration of the Lanczos Algorithm

In principle the eigenmode calculations could start with Eq. (3.4), i.e. one could determine the eigenmodes of largest modulus of  $-Q^2 + \sigma I$  (with  $\sigma$  being chosen large enough). But it is observed that the convergence of the Lanczos algorithm

can be improved by a further polynomial transformation. For Hermitian matrices the acceleration is normally accomplished with Chebyshev polynomials  $T_n$  [32]. The reason for this can be seen in Fig. (3.12), where a Chebyshev polynomial of order 40 is plotted. In the interval  $[-1, 1]$  it's functional values are very small, whereas they increase rapidly outside of  $[-1, 1]$ . This rapid increase can be exploited to reduce the level density of the searched for eigenvalues. Since the convergence of the Arnoldi algorithm depends on the level density of the searched for eigenvalues the previous polynomial transformation  $p$  has to be adjusted such that the searched for eigenvalues of  $Q^2$  are mapped outside the interval  $[-1, 1]$  whereas the unwanted eigenvalues lie in  $[-1, 1]$ . This can be achieved with a modified polynomial  $p$

$$p : Q \rightarrow p(Q) = \frac{2}{s^2}Q^2 - (1+r)I, \quad (3.5)$$

The polynomial carries two parameters:

- (i) The scale factor  $s$  is the spectral radius of  $Q$ . Thus the eigenvalues of  $\frac{2}{s^2}Q^2$  lie in the interval  $[0, 2]$ . Since  $s$  fluctuates little with the gauge fields  $\{U\}$ , it can be computed in a first Arnoldi run on just a few vacuum configurations.
- (ii) The offset parameter  $r$  represents a simple shift operation and controls the number of eigenvalues being outside the interval  $[-1, 1]$ . The fastest convergence, with respect to  $r$ , was found with  $r$  chosen such that approximately only the searched for eigenvalues lie outside the interval  $[-1, 1]$ .

The procedure is then the following:

Determine the eigenmodes of largest modulus of

$$T_n(p(Q)) = T_n\left(\frac{2}{s^2}Q^2 - (1+r)I\right). \quad (3.6)$$

The fastest convergence, with respect to the order of the Chebyshev polynomial  $n$ , was found with  $n$  being chosen such that only one Arnoldi factorization was required, i.e. by avoiding to restart the algorithm.

The dependence of the execution time and the number of matrix vector multiplications on the order of the Chebyshev polynomials is presented in Fig. (3.13). The lattice sizes used are  $4^4$  and  $8^4$ . It can be seen that the execution time is considerably reduced through the application of the Chebyshev polynomials.

The reason why this experiments were not performed on larger lattices as well is that there the convergence, without applying the Chebyshev polynomials was extremely poor. This shows that, as in the non-Hermitian case, the acceleration factor grows with the size of the lattice and becomes crucial.

## Part III

# THE PHYSICAL PROBLEM: Quantities that depend on the Quark Propagator

# Chapter 4

## Dominance of the low-lying eigenmodes

For the remainder of the thesis the hitherto described mathematical concepts and numerical algorithms shall be applied to physical problems. In the following three chapters quantities that depend on the quark propagator  $M^{-1}$  will be considered, namely the topological charge of a gauge field, the  $\pi$  and  $\eta'$  correlation functions. The aim is to analyze whether those quantities can be reliably calculated from a truncated eigenmode approach (TEA) to  $M^{-1}$ . This means that  $M^{-1}$  will be approximated by a spectral representation constructed from a few low-lying eigenmodes only.

There are two options to proceed, based on the spectral representations of the

- non-Hermitian Wilson-Dirac matrix  $M$  (with  $M|\phi_i\rangle = \sigma_i|\phi_i\rangle$ )

$$M^{-1} = \sum_i \frac{1}{\sigma_i} \frac{|\phi_i\rangle\langle\phi_i|\gamma_5}{\langle\phi_i|\gamma_5|\phi_i\rangle}, \quad (4.1)$$

- and the Hermitian matrix  $Q = \gamma_5 M$  (with  $Q|\psi_i\rangle = \lambda_i|\psi_i\rangle$ )

$$M^{-1} = \gamma_5 \sum_i \frac{1}{\lambda_i} \frac{|\psi_i\rangle\langle\psi_i|}{\langle\psi_i|\psi_i\rangle}. \quad (4.2)$$

For TEA the above sums will be approximated by taking only the low-lying eigenmodes into account. Due to the weight factor  $1/\lambda$  ( $1/\sigma$ ), they are hoped to be dominating the spectral representation.

*Is there a relation between the eigenmodes of  $M$  and  $Q$ ?*

There is no relation known which would allow for a construction of the eigenmodes of the one matrix given the eigenmodes of the other. Only for an eigenvalue zero it follows trivially

$$M|\psi\rangle = 0|\psi\rangle \Leftrightarrow Q|\psi\rangle = 0|\psi\rangle. \quad (4.3)$$

This relation will be used later to identify purely real eigenvalues of  $M$ .

*What  $\kappa$ s are preferable for TEA?*

With  $\kappa$  increasing towards the critical  $\kappa_c$  the small eigenvalues of  $M$  move leftwards, i.e. towards the imaginary axis and thus become smaller (with  $\kappa > \kappa_c$  the smallest eigenvalues will have negative real parts). This suggests that the larger  $\kappa \leq \kappa_c$  is the more dominating the low-lying eigenmodes become. Eq. (4.3) suggests that the same holds for the Hermitian case as well, i.e. that the eigenvalues of  $Q$  will decrease with increasing  $\kappa$ . Hence large  $\kappa$ s, i.e. small quark masses, support the idea of low-lying eigenmode dominance.

*Which of the two representations is preferable for TEA?*

The advantage of  $M$  lies in its shiftable (with respect to  $\kappa$ ) structure  $M = 1 - \kappa D$ , i.e. an eigenvector of  $M = 1 - \kappa D$  is also an eigenvector of  $M = 1 - \sigma D$ , for any  $\sigma \in \mathbb{R}$ . This allows for a semiquenched analysis of the  $\pi$  and  $\eta'$  correlation functions (of course only if the TEA approximation is reliable at all). On the other hand  $M$  is not normal and thus requires to work with biorthogonal sets of left and right eigenvectors, which might be unfavorable in terms of low-lying eigenmode dominance. Here  $Q$  might perform better due to its orthogonal basis of eigenvectors. It can actually be shown that the eigenmodes of  $Q$  provide the best approximation to  $M^{-1}$ . But  $Q$  does not possess a shiftable structure with respect to  $\kappa$  since the first term of  $\gamma_5(I - \kappa M)$  is not a multiple of  $I$ .

*$M$  or  $Q$ ?*

For the calculation of the physical quantities the Hermitian matrix  $Q$  will be employed. The low-lying eigenmodes of  $M$  will only be determined on a few configurations just to compare with the Hermitian case. It will be found that the eigenmodes of  $M$  do not provide, in the quark mass regimes reachable by nowadays supercomputers, a reliable approximation to  $M^{-1}$ .

*What are the parameters for the actual numerical experiments?*

For the practical benchmarking 200 (195) SESAM lattices of size  $16^3 \times 32$  with  $\kappa = 0.1575$  (0.1560) will be used [2]. Thus the rank of  $Q$  is  $\dim(Q) = 1\,572\,864$ , which explains why a complete diagonalization of  $Q$  and the use of the *identity* as such, Eq. (4.2), is practically impossible. Instead the 300 lowest-lying eigenmodes will be calculated on each of the gauge fields. Since the size of such a vector is approximately 25 MBytes, an archive space of  $(200+195)*300*25$  MByte  $\approx 3$  TBytes is required to store the eigenvectors.

For the acceleration of the Arnoldi algorithm the optimal convergence with respect to CPU time was found for a Chebyshev polynomial  $T_n$  of order  $n = 80$  and  $r$  chosen such that approximately *only* the searched for 300 lowest-lying eigenvalues were captured in the interval  $[-1 - r, -1]$ . With this parameter setting only one Arnoldi factorization [21] was needed (i.e. no restarting was required). Since the size of the factorization was chosen to be 600, the calculation of the eigenmodes takes

$2 \times 80 \times 600 = 96000$  matrix-vector multiplications (where the factor 2 is due to the fact that  $Q^2$  enters the Chebyshev polynomial).

## 4.1 The dependence of $Q$ 's low-lying eigenvalues on $\kappa$

Fig. (4.1) shows the 300 lowest-lying eigenvalues of  $Q$  averaged over the SESAM configurations, at lightest and heaviest sea quark mass respectively, for which the dependence of  $|\lambda_i|$  on  $i$  is plotted. The ordering is chosen according to

$$|\lambda_1| \leq |\lambda_2| \leq |\lambda_3| \leq \dots \quad . \quad (4.4)$$

The upper (lower) line corresponds to the heaviest (lightest) sea quark mass of the SESAM sample. Their ratio,  $|\lambda_i(\text{lightest})/\lambda_i(\text{heaviest})|$  is plotted in Fig. (4.2) as a function of  $i$ . It shows a rather steep rise for  $i \leq 100$ , which illustrates the growing importance of the lowest-lying modes in the spectral representation of  $Q^{-1}$ , Eq. (4.2), when decreasing the sea quark mass. This feature should become even more pronounced for the imminent QCD simulations in the yet deeper chiral regime,  $m_{PS}/m_V < 0.5$ , i.e. for larger  $\kappa \leq \kappa_c$ .

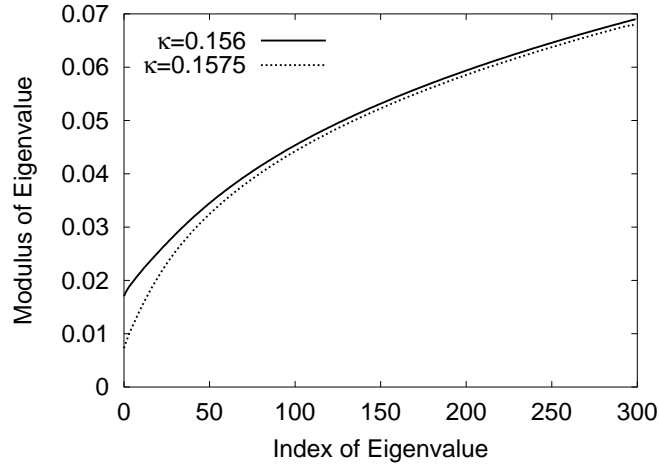


Figure 4.1: Distribution of moduli of the eigenvalues of  $Q$ , averaged over the configurations. The upper line corresponds to  $\kappa = 0.156$ , the lower to  $\kappa = 0.1575$ .

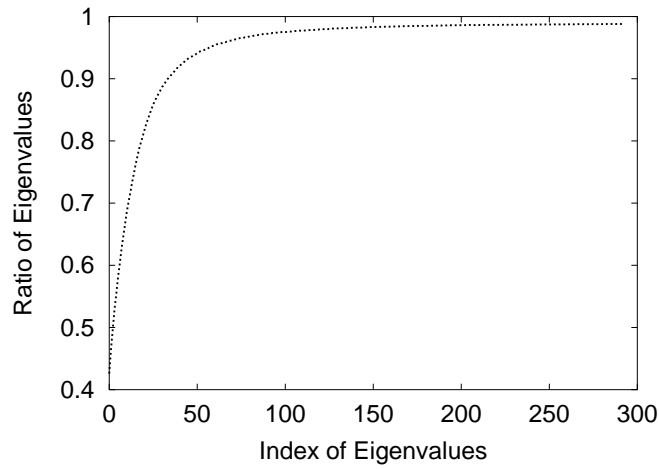


Figure 4.2: Same as Fig. 4.1, but plotted in terms of eigenvalue ratios,  $|\lambda_i(0.1575)/\lambda_i(0.1560)|$ , both ordered according to Eq. 4.4.

# Chapter 5

## The topological charge

### 5.1 Introduction

<sup>1</sup>In continuum gauge field theory the topological charge is a quantity that characterizes subsets of the set of all gauge fields that depend smoothly on space-time. The smoothness is not a constraint since it can always be achieved through an appropriate gauge fixing [34].

If a gauge field  $A_\mu(x)$  is a member of a certain subset, then all gauge fields that can be smoothly interpolated from  $A_\mu(x)$  are members of the same subset as well. In other words members of two different subsets cannot be smoothly transformed into each other (without having an infinite action at some stage of the transformation).

The subsets are in one to one correspondence with the set of integers  $\mathbb{N}$ . Due to this relation between a topological property of the gauge fields and the integer numbers, one speaks of the topological charge  $Q \in \mathbb{N}$  of the subsets. In other words all gauge fields belonging to the same subset carry the same topological charge.

For a given gauge field  $A_\mu(x)$  the corresponding topological charge  $Q$  can be measured through

$$Q = \frac{g^2}{64\pi^2} \int dx \epsilon_{\mu\nu\rho\sigma} F_{\mu\nu}(x) F_{\rho\sigma}(x) , \quad (5.1)$$

with

$$F_{\mu\nu}(x) = \partial_\mu A_\nu - \partial_\nu A_\mu - ig [A_\mu, A_\nu] , \quad (5.2)$$

and

$$A_\mu(x) = A_\mu^a(x) \lambda^a . \quad (5.3)$$

On the lattice however the situation is different. Each gauge field configuration  $U_\mu(x) \in SU(3)$  can be transformed into the trivial configuration  $U = 1$  through

$$U_\mu^\lambda(x) = \exp(i\lambda A_\mu(x)) , \quad (5.4)$$

---

<sup>1</sup>For a nice introduction to this subject, see [33]

with  $U_\mu^0(x) = 1$  and  $U_\mu^1(x) = U_\mu(x)$ . This means that the set of lattice gauge fields is simply connected. Hence the definition of a topological charge does not make sense on the lattice, but only in the continuum.

In spite of this findings one can work with the lattice remnants of the continuum concepts. For this one discretises (5.1) to test whether there is some kind of subset formation detectable, i.e. if this quantity shows a distribution over and an accumulation around the integer values. This would indicate the formation of topological non-trivial gauge field configurations when approaching the continuum limit. It can then be hoped, that quantities that are believed to depend strongly on the non-triviality of the gauge fields, such as the  $\eta'$  mass, are amenable to lattice calculations.

### 5.1.1 The Dirac matrix and the topological charge

In the continuum the topological density  $q(x)$ , defined through

$$Q = \int_V dx q(x) , \quad (5.5)$$

can be related to a fermionic quantity. This is done via the flavor singlet axial-vector current divergence relation (ABJ anomaly) [35, 36], given by

$$\partial_\mu \sum_{i=1}^{N_f} \bar{\psi}_i \gamma^5 \gamma^\mu \psi_i = 2m \sum_{i=1}^{N_f} \bar{\psi}_i \gamma^5 \psi_i + 2N_f q(x) , \quad (5.6)$$

where  $m$  is the quark mass and  $N_f$  the number of flavors.

This equation can be directly translated to the lattice. Since there periodic boundary conditions hold, the left hand side of (5.6) vanishes under the integration over space and time. It follows that

$$Q = \kappa_p \frac{m_q}{N_f} \sum_{i=1}^{N_f} \bar{\psi}_i \gamma^5 \psi_i = \kappa_p m_q \text{Tr} (\gamma_5 M^{-1}) , \quad (5.7)$$

where  $\kappa_p$  is a lattice renormalization constant. This equation shows that the topological charge is proportional to the trace of the quark propagator (multiplied by  $\gamma_5$ ).

In the following (5.7) (and not (5.1)) will be used to examine the potential of TEA in the topological charge case. Employing the Hermitian and non-Hermitian representation of  $M^{-1}$ , Eq. (5.7) reads

- Hermitian case

$$\text{Tr} Q^{-1} = \text{Tr} \sum_i \left( \frac{1}{\lambda_i} \frac{|\psi_i\rangle\langle\psi_i|}{\langle\psi_i|\psi_i\rangle} \right) = \text{Tr} \sum_i \left( \frac{1}{\lambda_i} \frac{\langle\psi_i|\psi_i\rangle}{\langle\psi_i|\psi_i\rangle} \right) = \sum_i \frac{1}{\lambda_i} \quad (5.8)$$

- non-Hermitian case

$$\text{Tr} (\gamma_5 M^{-1}) = \text{Tr} \left( \gamma_5 \sum_i \frac{1}{\lambda_i} \frac{|\psi_i\rangle\langle\psi_i|\gamma_5}{\langle\psi_i|\gamma_5|\psi_i\rangle} \right) = \text{Tr} \left( \sum_i \frac{1}{\lambda_i} \frac{\langle\psi_i|\psi_i\rangle}{\langle\psi_i|\gamma_5|\psi_i\rangle} \right) \quad (5.9)$$

The fact that the Hermitian approach to the topological charge only depends on the eigenvalues indicates that it is superior to the non-Hermitian case.

## 5.1.2 The standard approach

The two standard approaches to the topological charge of a lattice gauge field, cooling [37, 38, 39] and the stochastic estimator technique (SET) [11, 12, 13, 5, 14, 15, 9], make use of the equations (5.1) and (5.7) respectively.

### 5.1.2.1 Cooling

The Cooling method, an iterative, local minimization of the action, aims at a determination of the topological charge of a gauge field through Eq. (5.1). Since through the iteration the gauge fields converge to configurations satisfying the classical Euclidean equations of motion (instantons), Eq. (5.1) will produce integer values and thus reveal the topological sectors of the gauge fields.

A problem of cooling is that it cannot distinguish between an instanton-anti-instanton pair and the topologically trivial sector. This is because such a pair does not represent a classical solution of the Euclidean equations of motion. Thus the cooling process will remove them. This is problematic when it comes to measuring physical effects that, according to instanton based models, depend on instanton-anti-instanton pairs.

As can be seen in [39], cooling the SESAM configurations indeed yields values for the topological charges that accumulate around the integer values. This indicates that non-trivial gauge fields emerge close to the continuum limit.

In spite of this positive results the role of the cooling step is not obvious. Therefore this findings should be corroborated by a fermionic determination of the topological charge through (5.7), which does not require such a change of the gauge fields.

### 5.1.2.2 The Stochastic Estimator (SET)

The stochastic estimator technique is used to stochastically estimate entries of the matrix  $M^{-1}$  or  $Q^{-1}$ . The convergence of this method, i.e. the error of the estimates, depends on the size of the entry to be estimated, where large entries converge fast and small ones only slowly. Hence in praxis not all entries are accessible. Fortunately the elements around the diagonal of  $M^{-1}$  are the largest, which therefore makes a stochastic estimation of  $\text{Tr} (\gamma_5 M^{-1})$  possible.

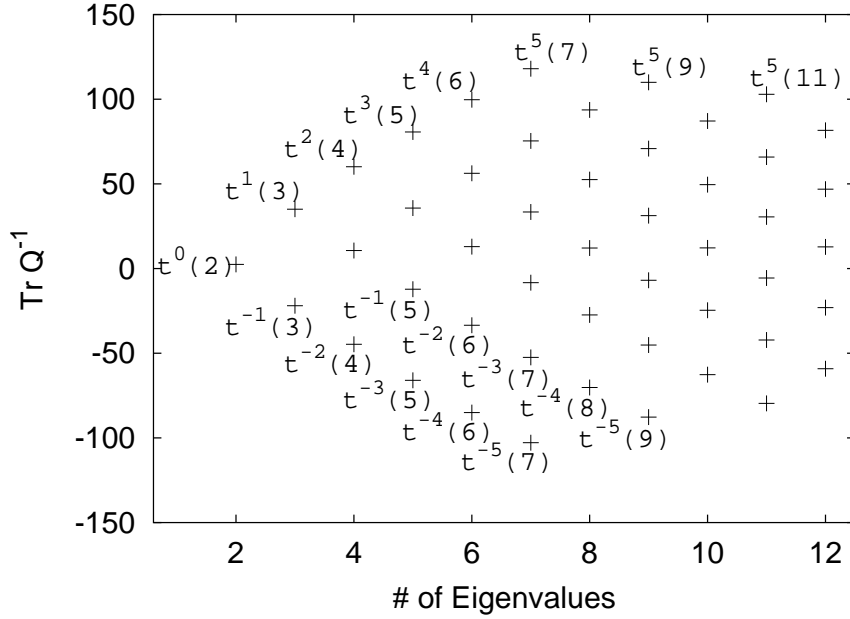


Figure 5.1: Partial sums, according to Eqs. (5.18) and (5.19), from a particular SESAM configuration at  $\kappa = 0.1575$ .

SET relies on solving linear systems of equations

$$M\xi = \phi^a, \quad (5.10)$$

with  $a \in \{1, 2, \dots, N_{est}\}$ . The source vectors  $\phi^a$  have stochastic entries, chosen such that

$$\langle \phi(x) \rangle = \frac{1}{N_{est}} \sum_{a=1}^{N_{est}} \phi^a \rightarrow 0, \quad (5.11)$$

$$\langle \phi(x)^\dagger \phi(y) \rangle \rightarrow \delta_{xy}. \quad (5.12)$$

It follows that

$$\langle \phi(x)^\dagger \xi(y) \rangle = \langle \phi(x)^\dagger M^{-1}(y, z) \phi(z) \rangle \rightarrow M^{-1}(y, x). \quad (5.13)$$

Hence  $\langle \phi(x)^\dagger \xi(y) \rangle$  is an estimate for  $M^{-1}(y, x)$ . It's quality depends on the size of the value  $M^{-1}(y, x)$  relative to the other entries and, apparently, on the number of estimates  $N_{est}$ .

To solve the linear system (5.10) on a SESAM lattice for  $\kappa = 0.1575$  about 180 matrix vector multiplications are required. Since  $N_{est} = 400$  provides reliable estimates, SET needs about  $180 * 400 = 72\,000$  matrix vector multiplications. This is comparable to TEA with its 96 000 multiplications.

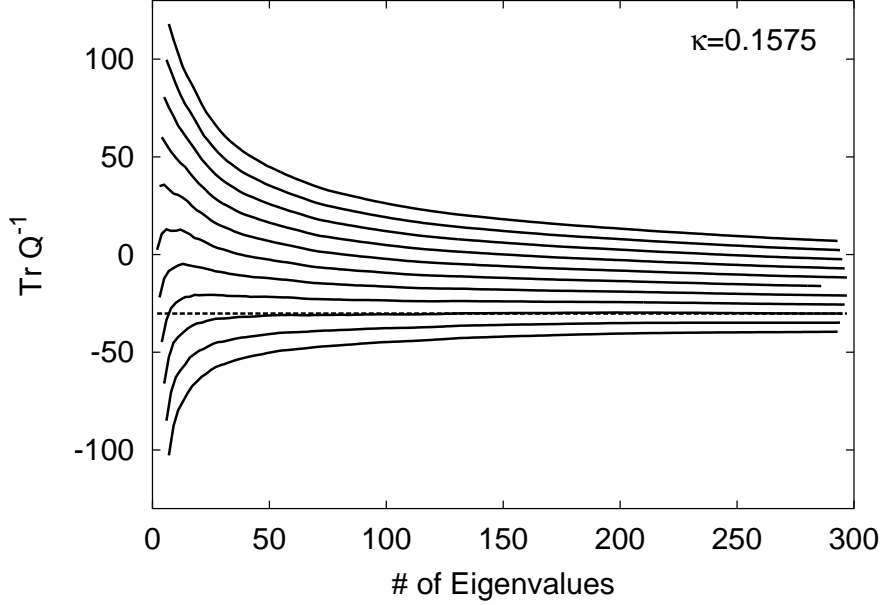


Figure 5.2: Same as in Fig. 5.1. The full lines connect the entries,  $t^j$ , with equal values of  $j$ . The horizontal line corresponds to the value  $t$  as defined in Eq. 5.22.

## 5.2 The Hermitian Dirac matrix and the topological charge

Let  $\mathcal{Q}$  be defined through

$$\mathcal{Q} = \text{Tr } Q^{-1} = \sum_i \frac{1}{\lambda_i}, \quad (5.14)$$

i.e.  $\mathcal{Q}$  is equal to the topological charge except for normalization factors. Physically, it is the low-lying modes that encapsulate the interesting information within the full sum of Eq. (5.14) while the large modes provide just nuisance by adding background noise to the infrared signal. In order to turn this qualitative proposition into a quantitative statement one would need to know the transition point between infrared and ultraviolet physics. For an approximate use of the spectral relation, Eq. (5.14), one needs a cunning technique to deplete the unwieldy background.

With this in mind a heuristic approach is taken and the pattern of eigenvalue distributions as obtained from the SESAM ensemble of vacuum configurations is studied. To reach the goal, it is useful to order the spectrum and perform certain partial summations in Eq. (5.14):

Let  $p_i$  denote the positive and  $n_i$  the negative eigenvalues,

$$\{\lambda_i\} = \{p_i\} \cup \{n_i\}, \quad (5.15)$$

and let them be ordered such that:

$$p_1 \leq p_2 \leq p_3 \leq \dots, \quad (5.16)$$

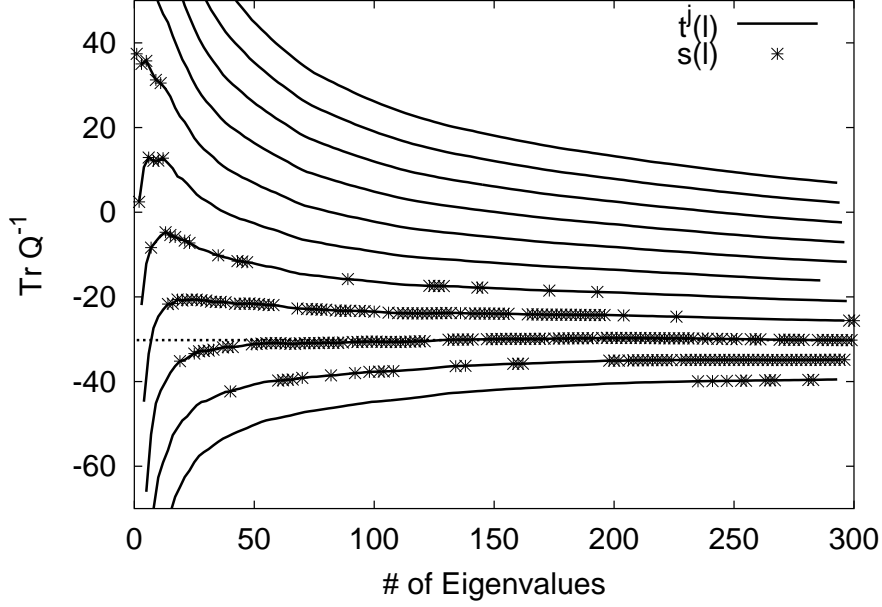


Figure 5.3: Partial sum, showing for each  $s(l)$  the associated  $j$  such that  $s(l) = t^j(l)$ .

$$|n_1| \leq |n_2| \leq |n_3| \leq \dots \quad (5.17)$$

In order to study convergence properties, let the following partial series be defined (see Fig. (5.1)):

$$t^j(l) = \sum_{i=1}^{j+k} \frac{1}{p_i} + \sum_{i=1}^k \frac{1}{n_i}, \quad j \geq 0 \quad (5.18)$$

$$t^j(l) = \sum_{i=1}^{j+k} \frac{1}{n_i} + \sum_{i=1}^k \frac{1}{p_i}, \quad j < 0 \quad (5.19)$$

$$l = |j| + 2k, \quad (5.20)$$

where, in obvious notation, the parameter  $j$  labels the excess number of entries with positive (negative) over the ones with negative (positive) eigenvalues. In Fig. (5.1) and Fig. (5.2) the values of  $t^j$  are plotted for the index range  $-5 \leq j \leq 5$ , as obtained from *one particular* SESAM configuration at the lightest available quark mass,  $\kappa = 0.1575$ . The partial sums appear to exhibit a certain convergence pattern which is displayed in Fig. (5.2), where the points to given  $j$ -values are connected.

Alternatively, one might organize the summation in the order of increasing moduli of the eigenvalues (Eq. (4.4)), independent of their signs, and define the truncated sums

$$s(l) = \sum_{i=1}^l \frac{1}{\lambda_i}. \quad (5.21)$$

The family of curves,  $\mathcal{F} = \{t^j(l)\}$  provides a suitable framework to disclose the asymptotic behavior of this inverse eigenvalue summation,  $s(l)$ . This is illustrated,

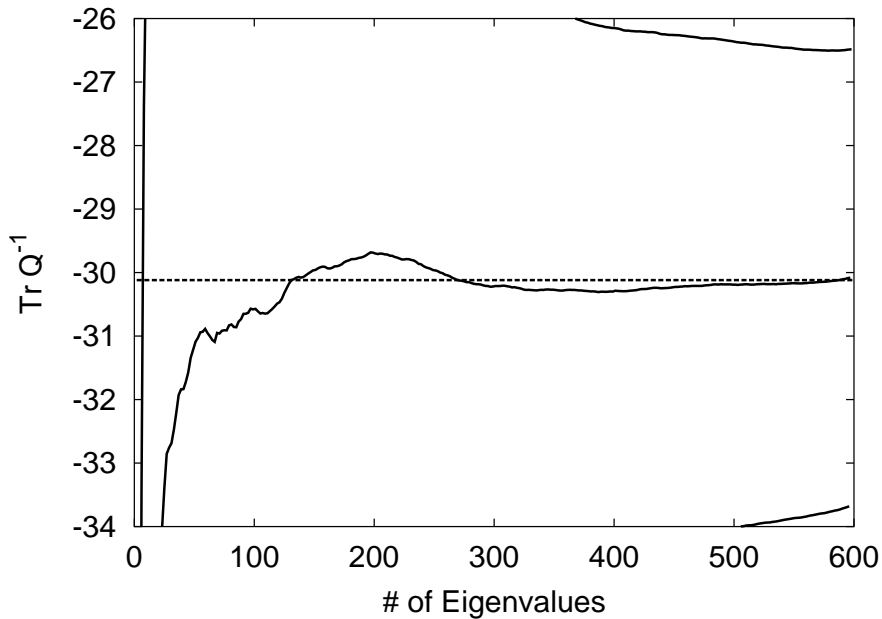


Figure 5.4: High resolution plot of  $t^p$  with 600 Eigenvalues

again for the particular gauge configuration, in Fig. (5.3), where the data points for  $s(l)$  in the range  $1 \leq l \leq 300$  are displayed. For reference the (slowly narrowing) band of the partial sums,  $t^j(l)$  are also shown. From  $s \approx 150$  onward,  $s(l)$  in this particular configuration jumps mostly between the two levels  $t^{-3}$  and  $t^{-4}$ . To put it differently: the asymptotic distribution of eigenvalues is characterized by alternating signs when proceeding according to the order given by Eq. (4.4). Moreover  $t^{-3}$  appears to be distinguished as lying between the asymptotically falling set of curves with  $j \geq -2$  and the rising ones,  $j \leq -4$ .

It is found that this scenario applies to all configurations in the sense that

- for each gauge field  $\{U\}$ ,  $\mathcal{F}$  contracts around a particular partial sum  $t^p(l)$  that levels to a plateau value beyond  $l \approx 150$ , with  $p$  depending on the choice of the gauge field  $[U]$ .

Next this observations will be quantified. The height of the supposed plateau will be denoted with  $t$ , setting

$$t := t^p(300), \quad (5.22)$$

where  $t$  varies with the underlying gauge configuration  $[U]$ . The question then arises how accurately one can extract the actual plateau height. In order to appreciate the numerical flatness of the plateau curve the eigenvalue computation was pushed to a number of 600 eigenmodes *on a single* SESAM configuration. In Fig. (5.4) the resulting plateau on a magnified scale is displayed. Assuming that the apparent remaining weak oscillation for  $l > 150$  is a *pars pro toto* feature for the entire SESAM sample and that with 300 eigenvalues one has already passed the first extremum on the entire sample of gauge fields  $U$ , one can estimate that from the lowest-lying 300

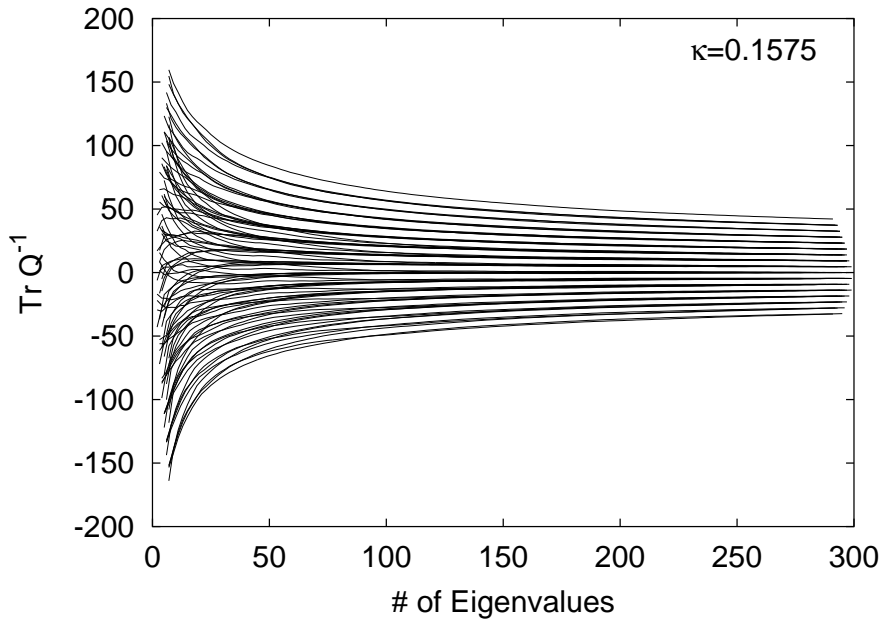


Figure 5.5: Functions as in Fig. 5.2 for 10 gauge fields such that their  $t$ -values are all equal to 0.

eigenvalues  $t$  can be determined with a *bona fide* accuracy of 1%.

Next it is argued that the plateau value,  $t[U]$ , provides an approximant for the complete trace, Eq. (5.14):

$$\mathcal{Q}[U] \approx t[U]. \quad (5.23)$$

What is the deviation from the complete trace in this situation? In the considered range of quark masses, zero-level crossings (see section (5.3.1)) of eigenmodes can be excluded. Therefore the matrix  $Q$  possesses an equal number of positive and negative eigenvalues. Hence, when adding up all  $n$  eigenvalues (with  $n = \dim(Q)$ ),  $s(n)$  will lie on the curve with superscript 0

$$\mathcal{Q} = s(n) = t^0(n), \quad \text{with } n = \dim(Q). \quad (5.24)$$

Thus  $\text{Tr } Q^{-1}$  is related to the plateau height  $t$  in the following way:

$$\mathcal{Q} = t + \frac{p}{|\lambda_n|}. \quad (5.25)$$

The second term on the right-hand side measures the distance between  $t^0$  and  $t^p$  at  $l = n$ . It can be neglected with respect to the error on  $t$  itself, since  $|1/\lambda_n \approx .15|$  is approximately equal to the error of  $t$ .

Another justification for the validity of this approximation, Eq. (5.23), comes from the observation that different field configurations  $[U_r]$  yield equal results when plotted with appropriate offsets  $t[U_r]$ , namely  $(t^j(l)[U_r] - t[U_r])$ . This is illustrated in Fig. (5.5) and Fig. (5.6) where 10 such series for  $U_r (r = 1, \dots, 10)$  were superimposed:

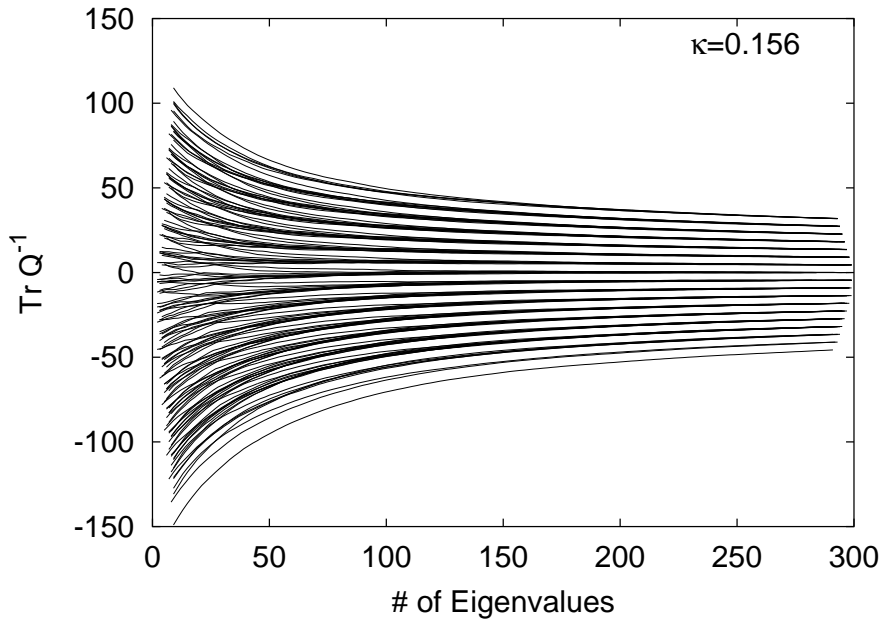


Figure 5.6: Functions as in Fig. 5.5, but for a heavier quark mass.

it strikes the eye that, for  $l > 150$ , the partial sums to the 10 gauge fields all *collapse onto a single, universal family of curves*:

$$t^{j+p_r}(l)[U_r] - t[U_r] = t^{j+p_s}(l)[U_s] - t[U_s]. \quad (5.26)$$

Hence there exists a set of  $U$ -independent functions  $\hat{t}^j(l)$  such that the following identity with respect to  $U$  applies:

$$t^{j+p[U]}(l)[U] - t[U] = \hat{t}^j(l). \quad (5.27)$$

This pattern strongly supports the picture that on the SESAM configurations the interesting physics with respect to the topological charge is indeed contained in the subset of the 150 smallest eigenvalues, while the remaining ones carry no information on  $\mathcal{Q}$ .

This result will be corroborated by considering a  $4^4$  lattice where all 3072 eigenvalues of  $Q$  in quenched QCD at  $\beta = 5.0$  were determined. In Fig. (5.7) the corresponding partial sums  $t^j$  are plotted. It can be seen that  $t^p$  (here  $p$  happens to be 0) remains absolutely flat after reaching its plateau value at around  $l \simeq 500$ .

### 5.2.1 Comparison with the standard methods

A comparison of the  $\mathcal{Q}$  values as produced by TEA with the ones obtained in Ref. [39] from SET on the entire  $\kappa = 0.1575$  sample is shown in Fig. (5.9). Whereas Fig. (5.8) shows, on a single configuration, the dependence of the stochastic estimate of  $\text{Tr } Q^{-1}$

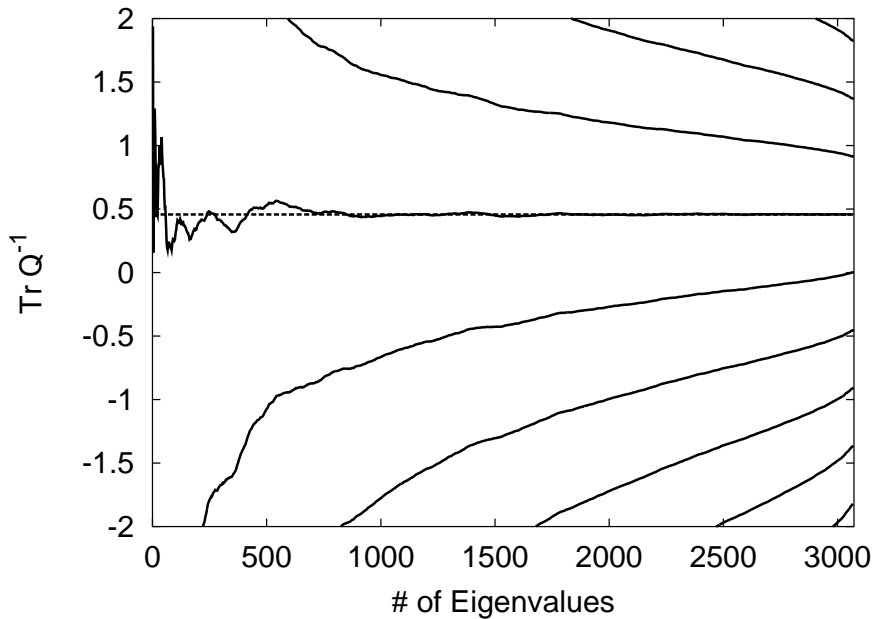


Figure 5.7: Pattern of partial series  $t^j$  on a quenched  $4^4$  lattice at  $\beta = 5.0$ , which allows for a calculation of the entire spectrum.

on the number  $N_{est}$  of source vectors  $\phi^a$  used and compares it to the TEA result. The data points in Fig. (5.9) seem to scatter rather nicely around the bisecting line. While the accuracy of the TEA results on individual configurations is about 1%, the uncertainty of the SET estimates turns out to be  $\Delta Q \approx \pm 50$ .

In Fig. (5.10) TEA's (normalized)  $Q$  values along the Monte Carlo history of the SESAM sample at  $\kappa = 0.1575$  is presented and compared to the result of the gluonic determination after cooling [39]. It shows that there is a close correlation between the gluonic and fermionic definitions of the net topological charge [40]. This corroborates the expectation that non-trivial gauge fields emerge on the lattice and thus that lattice QCD can deal with quantities that depend on the nontriviality of the topological charge.

### 5.3 The non-Hermitian Dirac matrix and the topological charge

The  $Q$  values as provided by the non-Hermitian approach are given by

$$Q = \text{Tr} \left( \sum_i \frac{1}{\lambda_i} \frac{\langle \psi_{\bar{i}} | \psi_i \rangle}{\langle \psi_{\bar{i}} | \gamma_5 | \psi_i \rangle} \right). \quad (5.28)$$

In the continuum limit the eigenvectors of  $M$  are orthogonal (see section (2.1.2)). Therefore only the real eigenmodes survive the scalar product in the denominator

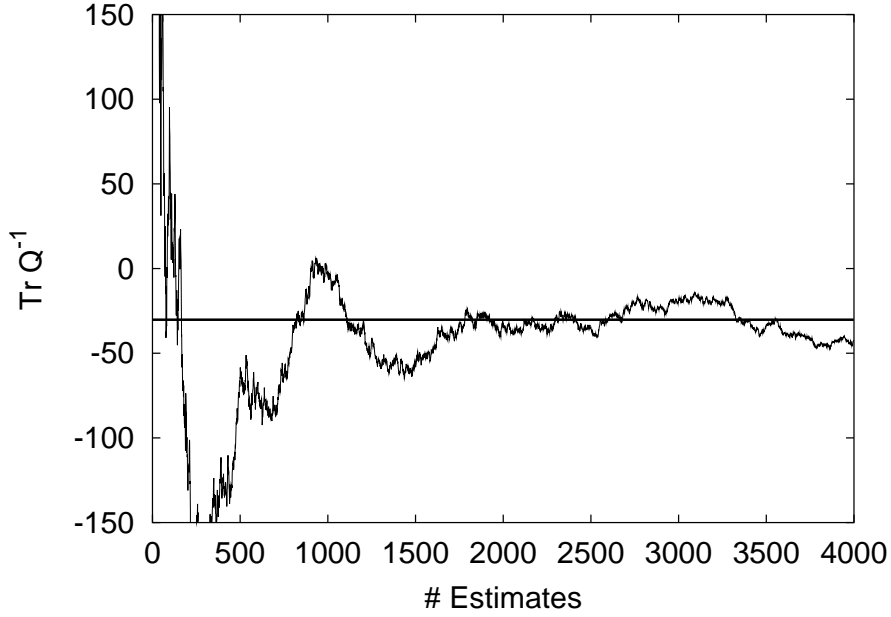


Figure 5.8: Comparing the results from TEA and SET on a single configuration at  $\kappa = 0.1575$ . The horizontal line represents the TEA result, whereas the curve shows the dependence of the stochastic estimate of  $\text{Tr } Q^{-1}$  on the number of source vectors  $\phi^a$  used.

of Eq. (5.28)

$$Q = \text{Tr} \left( \sum_{i, \lambda_i \text{ real}} \frac{1}{\lambda_i} \frac{1}{\langle \psi_i | \gamma_5 | \psi_i \rangle} \right) = \frac{1}{m_q} \sum_{i, \lambda_i \text{ real}} \langle \psi_i | \gamma_5 | \psi_i \rangle \quad \text{for } a \rightarrow 0, \quad (5.29)$$

where the real eigenvalues are equal to the quark mass  $m_q$ . The last equation holds since the eigenvectors can be chosen such that they are eigenvectors of  $\gamma_5$ , i.e. to have a definite chirality. Denoting the number of eigenvectors with positive (negative) chirality by  $n_+$  ( $n_-$ ) the topological charge is given by the so called index theorem

$$Q = n_+ - n_- . \quad (5.30)$$

On the lattice however  $|\psi_i\rangle$  and  $|\psi_i\rangle$  are not orthogonal. Therefore not only the purely real eigenmodes contribute to the sum Eq. (5.28).

Let the following series be defined

$$s(k+l) = \sum_{i=1}^k \frac{\langle \psi_i | \psi_i \rangle}{\lambda_i \langle \psi_i | \gamma_5 | \psi_i \rangle} + \sum_{j=1}^l \left( \frac{\langle \psi_{\bar{j}} | \psi_j \rangle}{\lambda_i \langle \psi_{\bar{j}} | \gamma_5 | \psi_j \rangle} + \frac{\langle \psi_j | \psi_{\bar{j}} \rangle}{\lambda_i \langle \psi_j | \gamma_5 | \psi_{\bar{j}} \rangle} \right), \quad (5.31)$$

to investigate the question whether Eq. (5.28) shows a convergence pattern similar to the one found for the Hermitian case. The first term includes the real eigenvalues

and the second term the complex ones. Since the eigenmodes are ordered according to  $|\lambda_1| \leq |\lambda_2| \leq \dots$ , the series (5.31) is well-defined.

Since Eq. (5.29) suggests that the real eigenmodes are the dominant terms in Eq. (5.31), in addition a series  $s_r$  derived from only the real eigenmodes is defined

$$s_r(k) = \sum_{i=1}^k \frac{\langle \psi_i | \psi_i \rangle}{\lambda_i \langle \psi_i | \gamma_5 | \psi_i \rangle}. \quad (5.32)$$

In Fig. (5.11)  $s(l)$  and  $s_r(l)$  are compared with the results derived from the eigenmodes of the Hermitian matrix  $Q$ .  $s_r(k)$  is plotted at  $k + l$  (see Eq. (5.31)). It can be seen that  $s(l)$  is far off and  $s_r$  pretty close to the  $Q$  value as determined from the Hermitian case. Thus the real eigenmodes indeed contain the dominating information about the topological charge, whereas the contribution of the complex eigenmodes can be viewed as lattice artefacts. In other words this findings suggest that the index theorem is applicable on the lattice as well.

It is now an interesting question for the applicability of the index theorem whether the real eigenmodes are separated from the doublers (real eigenmodes that only describe lattice artefacts). If this is so, the real eigenvalues of  $M$  must be accumulated around 0, 0.5, 1, 1.5 and 2, where the ones around 0 are physical.

To answer this question, the real eigenmodes lying in the interval  $[0; 0.5]$  for the SESAM configuration used in Fig. (5.11) and Fig. (5.12) will be determined.

As one can see in Fig. (5.12), the polynomial method  $p_{\sigma,n}$  can only search a part of the interval. For the remains the level crossing method will be employed.

### 5.3.1 Level crossing

For each real eigenmode  $(\lambda, |\psi\rangle)$  of  $M = I - \kappa D$  there exists a  $\sigma$  such that

$$(I - \sigma D) |\psi\rangle = 0. \quad (5.33)$$

It can easily be shown that

$$\sigma = \frac{\kappa}{1 - \lambda}. \quad (5.34)$$

It follows then that

$$\gamma_5(I - \sigma D) |\psi\rangle = 0, \quad (5.35)$$

holds as well.

Reversing the line of reasoning the real eigenmodes of  $M$  can be found by identifying the  $\kappa$ s for which  $Q$  has an eigenvalue 0. The corresponding eigenvalues of  $D$  are  $1/\kappa$  [41].

To simplify this search for the appropriate  $\kappa$ s one can make use of the derivatives of  $Q$ 's eigenvalues

$$\frac{\partial \lambda}{\partial (1/\kappa)} = \kappa (\langle \psi | \gamma_5 | \psi \rangle - \lambda). \quad (5.36)$$

In this manner one can follow the flow of  $Q$ 's low-lying eigenvalues, i.e. the dependence of the eigenvalues on  $1/\kappa$ , and search for a so called level crossing, i.e. for an eigenvalue that crosses the abscissa.

This method is now used to complete the above described search for the real eigenmodes in the interval  $[0; 0.5]$ . The result (for  $D$ s eigenvalues) is presented in Fig. (5.13). It can be seen, that the real eigenmodes are distributed all over the considered interval. This means that there is no clear separation of the physical and the doubler eigenmodes. This makes an application of the index theorem difficult, since it is not clear which of the eigenmodes should enter the sum Eq. (5.28).

### 5.3.1.1 Level crossing and even-odd preconditioning

For the level crossing analysis the size of the Dirac matrix can be halved through an even-odd preconditioning. For this the smallest eigenvalues of the Hermitian matrix  $\gamma_5(I - \kappa^2 D_{eo}D_{oe})$  are determined. It follows from

$$\gamma_5(I - \kappa^2 D_{eo}D_{oe})|\psi\rangle = 0|\psi\rangle \quad (5.37)$$

that

$$\kappa^2 D_{eo}D_{oe}|\psi\rangle = |\psi\rangle . \quad (5.38)$$

With the results derived for even-odd preconditioning in section (2) it follows directly that from  $|\psi\rangle$  one can construct a vector  $|\phi\rangle$  such that

$$(I - \kappa D)|\phi\rangle = 0|\phi\rangle . \quad (5.39)$$

The derivative for the preconditioned system now reads

$$\frac{\partial \lambda}{\partial(1/\kappa)} = 2\kappa (\langle \psi | \gamma_5 | \psi \rangle - \lambda) , \quad (5.40)$$

which shows that the eigenvalues of Eq. (5.37) are approximately twice as large as the ones obtained from  $Q$  itself (since both share eigenvalues 0 and the derivatives then show how fast this eigenvalues grow with changing  $\kappa$ ).

With this preconditioning the convergences of the algorithm can be accelerated by a factor of about 2.

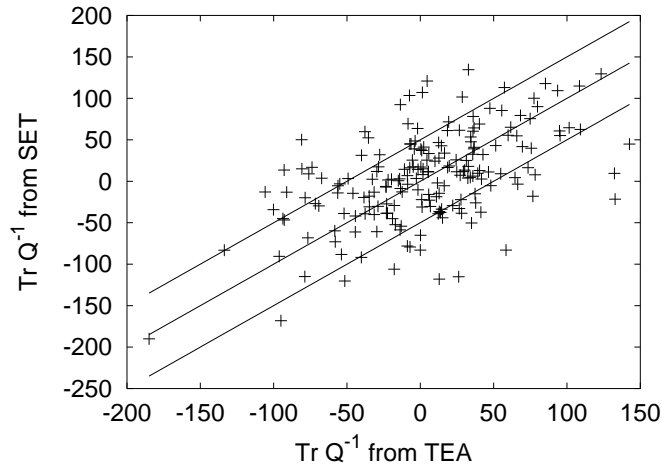


Figure 5.9: Scatterplot comparing the results from TEA and SET on all configurations at  $\kappa = 0.1575$ . The error band is chosen such that 67% of the data points lie within.

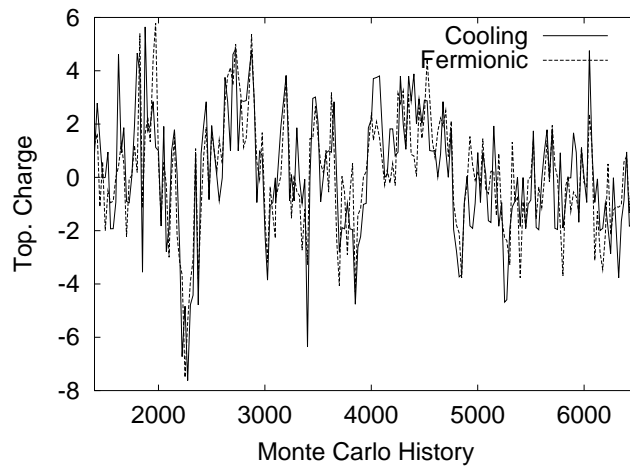


Figure 5.10: Comparison of TEA's estimates of the topological charge with the gluonic determination after cooling, on all SESAM configurations at lightest quark mass  $\kappa = 0.1575$ .

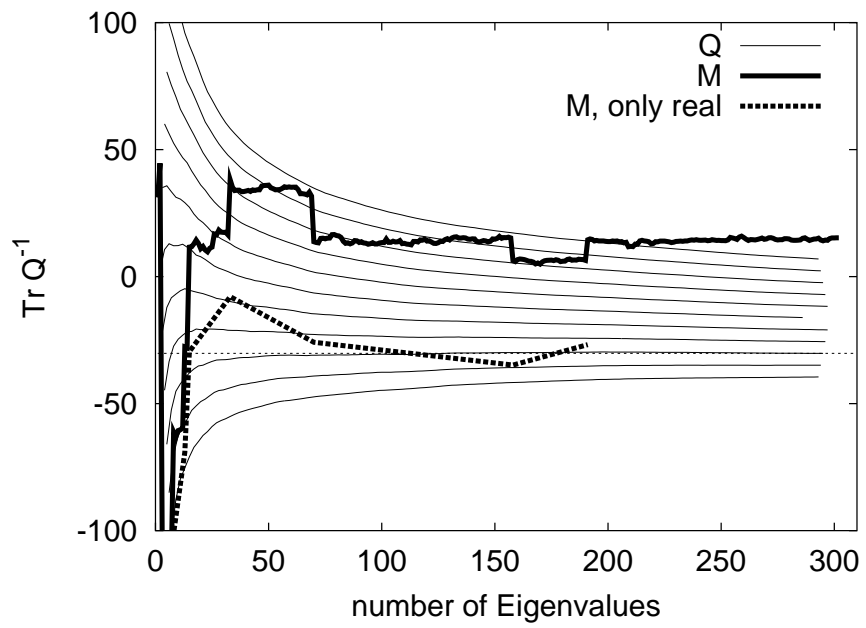


Figure 5.11: Comparison of the Hermitian and non-Hermitian approach to the topological charge.

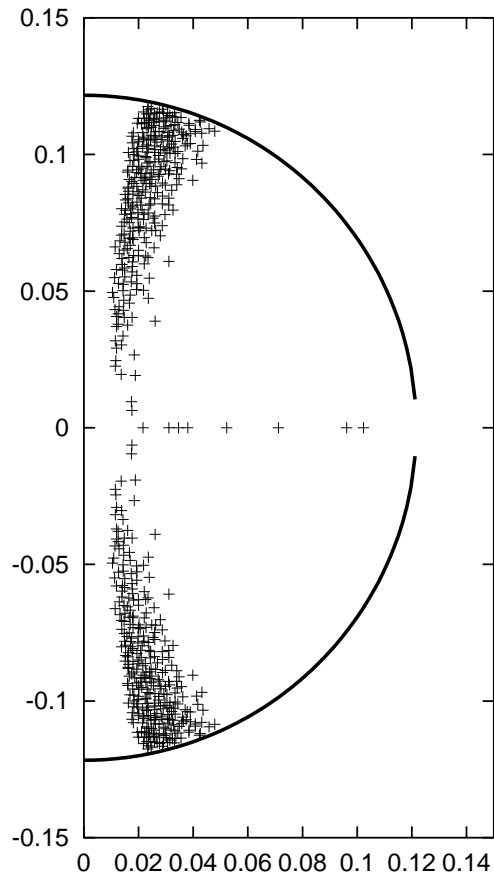


Figure 5.12: 600 eigenvalues of  $M$  as found through the application of  $p_{\sigma,\epsilon}$ . The curve represents a circle around the origin.

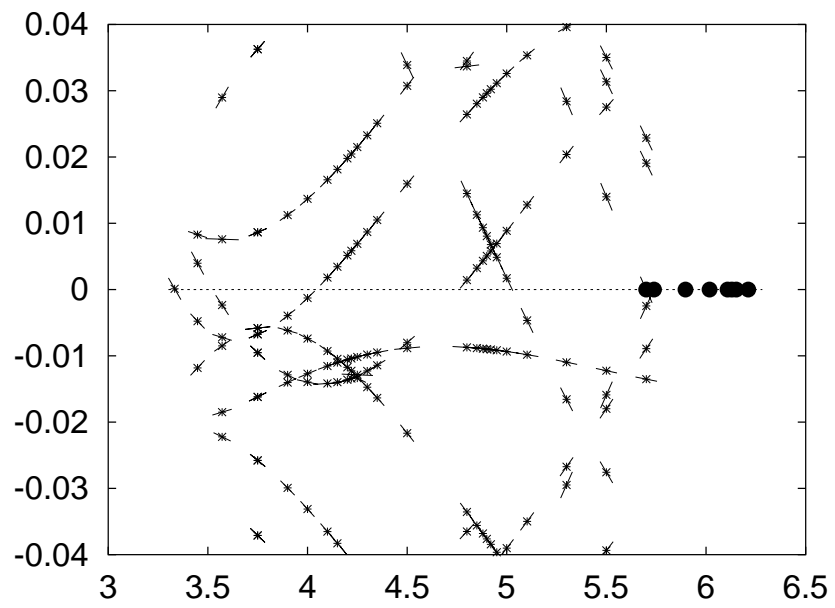


Figure 5.13: Level crossing diagram of a single configuration. It can be seen that for the SESAM configurations the physical eigenmodes are not separated from the doublers.

# Chapter 6

## The Pion

The aim of this and the following chapter is to employ TEA for the determination of the lattice masses of the  $\pi$  and the  $\eta'$ . It will be seen that the  $\pi$ , being a flavor octet particle, is a difficult quantity for TEA, whereas the standard approach can rather easily deal with it. The singlet particle  $\eta'$  however involves quark loops, which are numerically very demanding quantities. In this case TEA shows a convergence behavior, with respect to the number of eigenmodes used, that is comparable to the topological charge case. The computational demands of the standard approach to the quark loops is comparable to TEA's.

### 6.1 Basics for mass determinations

#### 6.1.1 Correlation functions

For each hadron a correlation function  $C$  can be constructed. For mesons products of two quark propagators  $M^{-1}$  enter  $C$ , whereas baryonic correlation functions are constructed from products of three  $M^{-1}$ s. Apart from that  $C$  has to carry the appropriate quantum numbers. For instance the  $\pi$  requires  $\gamma_5$  matrices to provide the right parity quantum number.

The correlation functions of the particles that will be considered here, the  $\pi$  and the  $\eta'$ , have the following form

$$\begin{aligned} C_\pi(\Delta t) &= \left\langle \sum_{s_i, \alpha_i, a_i, t} [Q^{-1}(s_1, t, \alpha_1, a_1; s_2, t + \Delta t, \alpha_2, a_2) \right. \\ &\quad \left. Q^{-1}(s_2, t + \Delta t, \alpha_2, a_2; s_1, t, \alpha_1, a_1)] \right\rangle_U \quad (6.1) \\ C_{\eta'}(\Delta t) &= C_\pi(\Delta t) - N_f \left\langle \sum_t \mathcal{Q}(t) \mathcal{Q}(t + \Delta t) \right\rangle_U, \end{aligned}$$

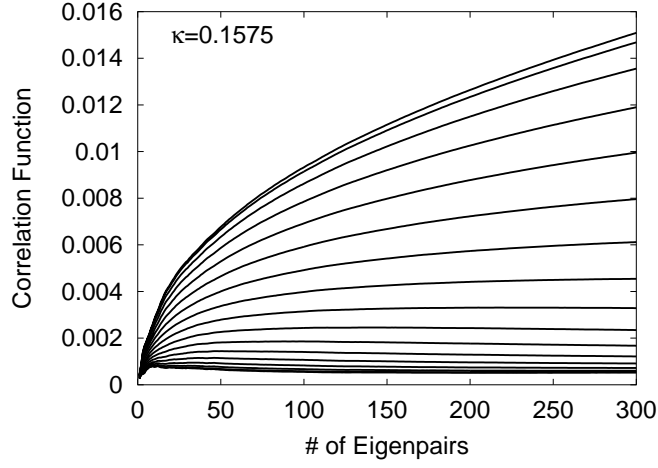


Figure 6.1: Set of  $\pi$  correlation function  $C^l(\Delta t)$  from TEA on local sinks and sources, plotted against the spectral cutoff,  $l$ .  $\Delta t$  increases as one steps down from the top curve which refers to  $\Delta t = 0$ .

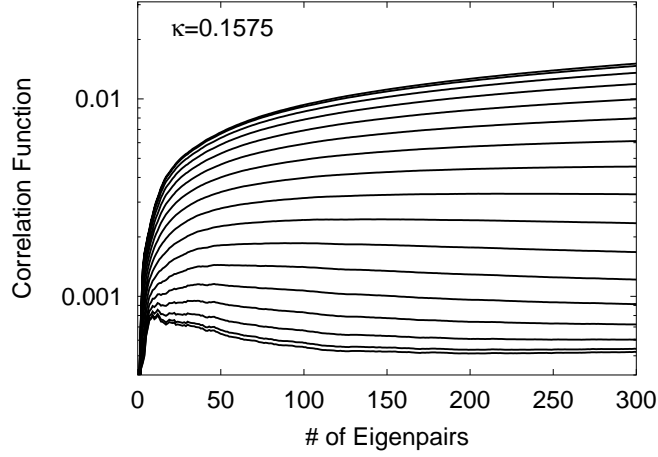


Figure 6.2: Same as above, but logarithmic in the ordinate

with  $\mathcal{Q}(t) = \sum_{s,\alpha,a} Q^{-1}(s, t, \alpha, a; s, t, \alpha, a)$  and  $N_f = 2$  flavors. The coordinate  $n$  is subdivided into a spatial  $s$  and a temporal part  $t$ .

By introducing energy eigenfunctions one can show that these correlation functions decay exponentially in time, with the particle mass being the decay constant  $C(\Delta t) \sim \exp(-m\Delta t)$ . On a toroidal lattice however with temporal extent  $T$  this exponential decay appears as a cosh,  $C(\Delta t) \sim \exp(-m\Delta t) + \exp(m(\Delta t - T))$ . Local masses  $m$  can be retrieved for every value of  $\Delta t$  by solving the implicit equations

$$\frac{C(\Delta t + 1)}{C(\Delta t)} = \frac{\exp(-m(\Delta t + 1)) + \exp(m(\Delta t + 1 - T))}{\exp(-m\Delta t) + \exp(m(\Delta t - T))}, \quad (6.2)$$

with respect to  $m$ . Plateaus in the time dependence of the local masses  $m(\Delta t)$  exhibit the masses of the particles.

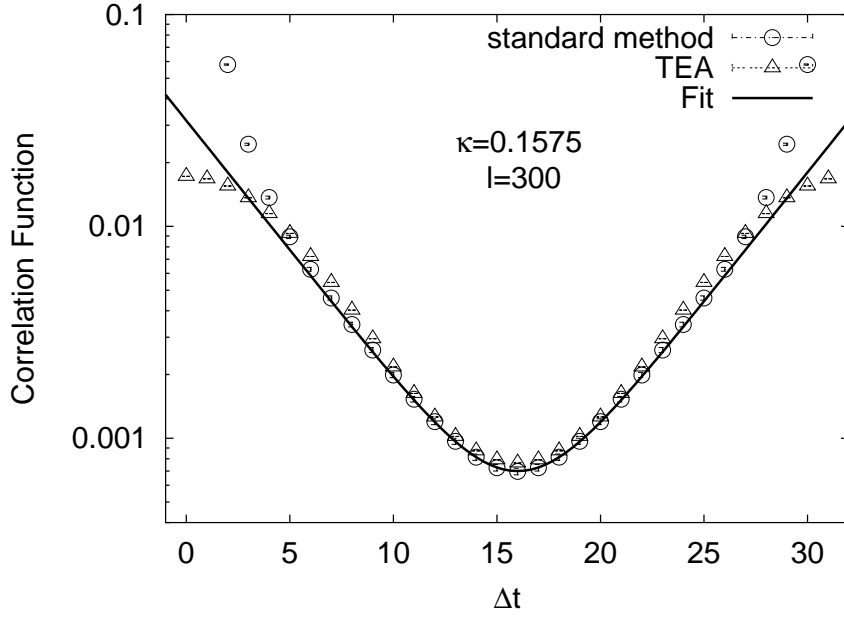


Figure 6.3: Comparison of the  $\pi$  correlation function as provided by TEA with  $l = 300$ , with the one obtained from the standard method (solving linear systems) on local sinks and sources.

### 6.1.2 Smearing

The extension of the local mass plateaus can be increased by enhancing the overlap with the ground state correlation function. By following Ref. [42] the smearing matrix  $S = (F)^k$  is applied, with

$$\begin{aligned}
 F(n, \alpha, a; m, \beta, b) &= \frac{1}{1 + 6l} \left[ \delta(n, \alpha, a; m, \beta, b) \right. \\
 &\quad \left. + l \sum_{\mu=1}^3 \left( U_{n,\mu}(a; b) \delta(n + \hat{\mu}; m) + U_{n-\hat{\mu},\mu}^\dagger(a; b) \delta(n - \hat{\mu}; m) \right) \right], \tag{6.3}
 \end{aligned}$$

choosing  $k = 50$  and  $l = 4$ .

Source and sink smearing are readily accomplished by the replacements

$$|\psi_i\rangle \rightarrow |\psi_i^s\rangle \equiv S|\psi_i\rangle \tag{6.4}$$

in the spectral propagator representation

- for  $Q$

$$Q_{sm}^{-1} = \sum_i \frac{1}{\lambda_i} \frac{|\psi_i^s\rangle \langle \psi_i^s|}{\langle \psi_i | \psi_i \rangle}, \tag{6.5}$$

- and for  $M$

$$M_{sm}^{-1} = \sum_i \frac{1}{\lambda_i} \frac{|\psi_i^s\rangle \langle \psi_i^s | \gamma_5}{\langle \psi_i | \gamma_5 | \psi_i \rangle}, \tag{6.6}$$

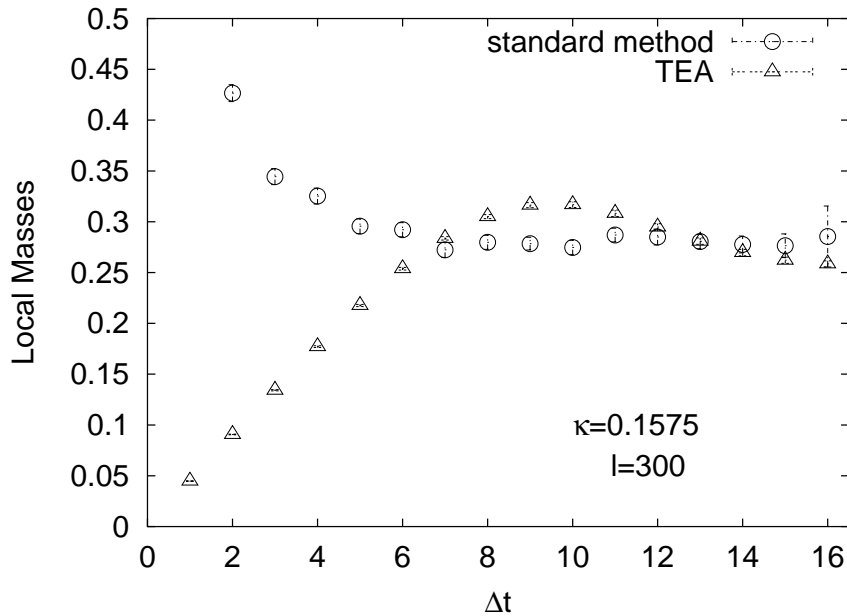


Figure 6.4: Local  $\pi$  masses from TEA and the standard method .

since  $F$  and  $\gamma_5$  commute.

## 6.2 The correlation function of the $\pi$

### 6.2.1 The standard method

The standard approach to the correlation function of the  $\pi$  is based on solving the linear systems

$$M(n, m)\xi(m) = \delta(n, c) . \quad (6.7)$$

The solution vector  $\xi(m)$  is equal to the  $c^{th}$  column of  $M^{-1}$ . Usually twelve such columns (for each spin and color index on a particular lattice site) are used for an approximate calculation of  $C_\pi$

$$\begin{aligned} C_\pi(\Delta t) &= \frac{1}{V} \sum_{s_i, t, \alpha_i, a_i} (M^{-1})^*(s_1, t, \alpha_1, a_1; s_2, t + \Delta t, \alpha_2, a_2) \\ &\quad M^{-1}(s_1, t, \alpha_1, a_1; s_2, t + \Delta t, \alpha_2, a_2) \\ &\approx \sum_{\alpha_1, a_1, s_2, t, \alpha_2, a_2} (M^{-1})^*(s_1, t, \alpha_1, a_1; s_2, t + \Delta t, \alpha_2, a_2) \\ &\quad M^{-1}(s_1, t, \alpha_1, a_1; s_2, t + \Delta t, \alpha_2, a_2) , \end{aligned} \quad (6.8)$$

where a normalization factor  $1/V$  was introduced.

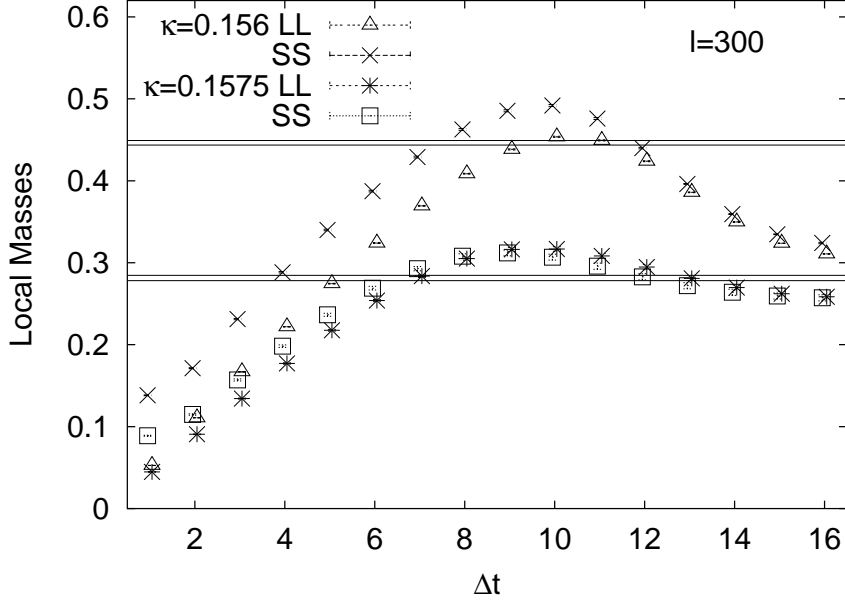


Figure 6.5: Local masses of the  $\pi$  from TEA. LL are the unsmeared results, whereas SS stands for smearing the sinks and sources. The horizontal lines show the error-bands of the  $\pi$  as obtained from the standard method (solving linear systems).

On the SESAM lattice solving the above linear systems take about 160 matrix vector multiplications  $N^{mv}$  (for  $\kappa = 0.1575$ ). Thus the determination of  $C_\pi$  on a single gauge field requires  $N^{mv} = 12 \times 160 = 1920$  multiplications, which is significantly smaller than TEA, requiring  $N^{mv} = 96000$ .

### 6.2.2 The Hermitian approach

Employing the eigenmodes of  $Q$ , the spectral representation of  $C_\pi(\Delta t)$  reads

$$\begin{aligned}
 C_\pi(\Delta t) &= \sum_{i,j,t} \frac{1}{\lambda_i \lambda_j} \frac{\langle \psi_i(t) | \psi_j(t) \rangle \langle \psi_j(t + \Delta t) | \psi_i(t + \Delta t) \rangle}{\langle \psi_i | \psi_i \rangle \langle \psi_j | \psi_j \rangle} \\
 &\equiv \sum_{i,j} \Psi(i, j, \Delta t), \tag{6.9}
 \end{aligned}$$

where the brackets that represent the average over the gauge fields are suppressed.

For  $C_\pi$  no early saturation, with respect to the number of eigenmodes used, over the entire  $\Delta t$ -range can be expected, as one can see by integrating Eq. (6.9)

$$\sum_{\Delta t} C_\pi(\Delta t) = \sum_i \frac{1}{\lambda_i^2}. \tag{6.10}$$

Since all the contributions on the *r.h.s.* of Eq. (6.10) are positive the series is monotonically increasing. Therefore – contrary to the case of the topological charge –

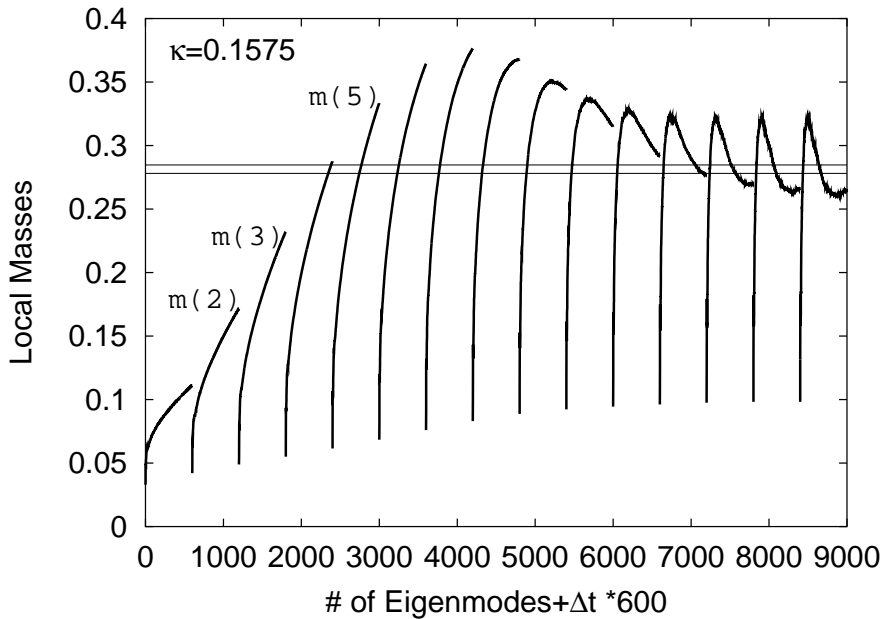


Figure 6.6: The dependence of the local masses  $m(\Delta t)$  on the spectral cutoff,  $l \leq l_{max} = 600$ , on a single configuration. The x-axis carries the parameter  $l_{\Delta t} = 600\Delta t + l$  with  $\Delta t = 1, 2, \dots, 15$ . The horizontal line shows the errorband of the  $\pi$  mass as obtained from the standard method (solving linear systems).

neither cancellation effects nor early saturation can be expected in this global quantity. But what about the regime of infrared physics described by the correlator, i.e. its asymptotic behavior in  $t$ ?

To analyze this a truncated spectral correlator is introduced

$$C_{\pi}^l(\Delta t) = \sum_{i,j=1}^l \Psi(i, j, \Delta t) . \quad (6.11)$$

In order to demonstrate the low-lying eigenmode dominance at large time separations Fig. (6.1) shows a family of curves,  $C_{\pi}^l(\Delta t)$ , for the various time slices  $\Delta t$ , plotted against the spectral cutoff,  $l$ , at the lightest SESAM quark mass. It is gratifying to find that  $C_{\pi}^l(\Delta t)$  for  $\Delta t \geq 7$  shows a flat behavior in the regime  $l > 100$ . On the other hand for small time separations higher eigenmodes continue to add – in accordance with the idea of excited state contaminations. In other words the monotonic increase of Eq. (6.10) is due to the behavior of  $C_{\pi}^l(\Delta t)$  for  $\Delta t < 7$ .

It is interesting to carry out a direct comparison of TEA with the standard propagator as computed by linear solvers on a local source, in order to see saturation occur in the region of interest, see Fig. (6.3). Good agreement in the asymptotic regime,  $7 \leq \Delta t \leq 25$  is found. It is also shown the fit (fit range:[8, 15]) to the data from the inverter to the usual cosh parameterization:

$$C_{\pi}^g(\Delta t) = A \cosh [m_{\pi}(\Delta t - T/2)] . \quad (6.12)$$

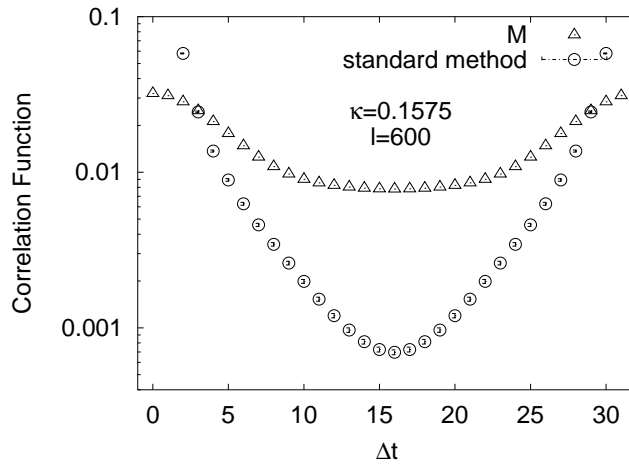


Figure 6.7: Pion correlation function from TEA with 600 eigenmodes of  $M$  on one configuration for  $\kappa = 0.1575$ . One observes strong deviations from the standard propagator (from linear solvers) determined on the entire gauge field ensemble.

A much more sensitive test of TEA is to look at local effective masses. In Fig. (6.4) a comparison, at the cutoff value  $l = 300$ , of the TEA results with the ones from standard propagator analysis, for the lightest SESAM quark mass is presented. The effects of smearing and varying quark masses are displayed in Fig. (6.5), again for  $l = 300$ . As anticipated, a clear tendency for improvement in the spectral approach with decreasing quark mass is observed. Yet there remains a marked oscillatory behavior over the entire SESAM range of quark masses. Moreover it can be seen that smearing slightly improves the signal, i.e. increases the effective masses for small  $\Delta t$ , whereas for large  $\Delta t$  the signal is not altered.

A synopsis on the cutoff dependence of  $m(\Delta t)$  is presented in Fig. (6.6), as obtained on a particular configuration at the lightest quark mass. To avoid cluttering of the data the different curves are spread out by means of the variable  $l_{\Delta t} = 600\Delta t + l$ . This survey plot is meant to convey an idea how the oscillation will dampen out with increasing cutoff  $l$ .

It follows from the above that in the sea quark mass regime of the SESAM configurations, there is insufficient dominance of the low-lying eigenmodes to utilize TEA for a sensible calculation of the  $\pi$  mass.

### 6.2.3 The non-Hermitian approach

For the non-Hermitian TEA 600 low-lying eigenmodes of  $M$  on a particular SESAM configuration were calculated. In Fig. (5.12) the corresponding eigenvalues are displayed. The exponent and the shift of the polynomial acceleration  $p_{\sigma,\epsilon}$  were tuned such that the algorithm found the eigenmodes of smallest modulus.

In Fig. (6.7) the  $\pi$  correlation function as obtained from  $M$ 's eigenmodes is compared

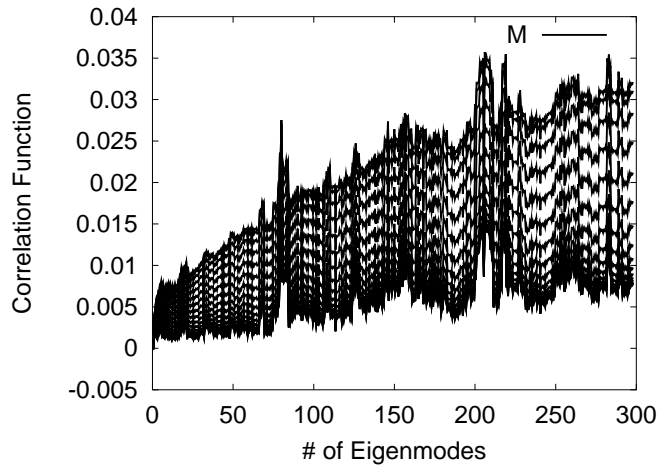


Figure 6.8: Pion correlation function from TEA for  $M$  and  $Q$  on a SESAM lattice at  $\beta = 5.0$ . The plot is analogous to Fig. 6.1.

to the standard method. It can be seen that the non-Hermitian approach does not provide a good approximation to  $C_\pi$  and thus that the eigenmodes of  $M$  contain less information about this function than the Hermitian ones. This conclusion is corroborated by Fig. (6.8) which shows the dependence of  $C_\pi$  on the cutoff  $l$ . The rather chaotic behavior of  $C^l(\Delta t)$  has to be compared with the smooth curves in Fig. (6.1).

To trace down this discrepancy a similar calculation was done on a quenched  $4^4$  lattice for  $\beta = 5.0$ , where all eigenmodes of  $M$  and  $Q$  were determined. In Fig. (6.9) the two results are displayed. Again a chaotic behavior for  $C^l(\Delta t)$  as determined from  $M$ 's eigenmodes all over the entire cutoff range can be seen. This is in contrast to the smooth curves as provided by the Hermitian approach to  $C^l(\Delta t)$ .

It can be concluded that all the eigenmodes of  $M$ , being non orthogonal, suffer interferences among each other. Thus, for the  $4^4$  test case and in the SESAM sea quark mass regime, a limited number of dominating eigenmodes cannot be identified.

To study whether lighter quark masses improve the quality of the non-Hermitian TEA, a semiquenched determination of  $C_\pi$  is presented in Fig. (6.10) and compared to the corresponding semiquenched standard analysis. The valence quark  $\kappa$  was chosen to be  $\kappa = 0.1585$ , very close to  $\kappa$  critical. Again the difference of the two signals is very large, showing that even for lighter valence quark masses an improvement of the non-Hermitian signal cannot be achieved.

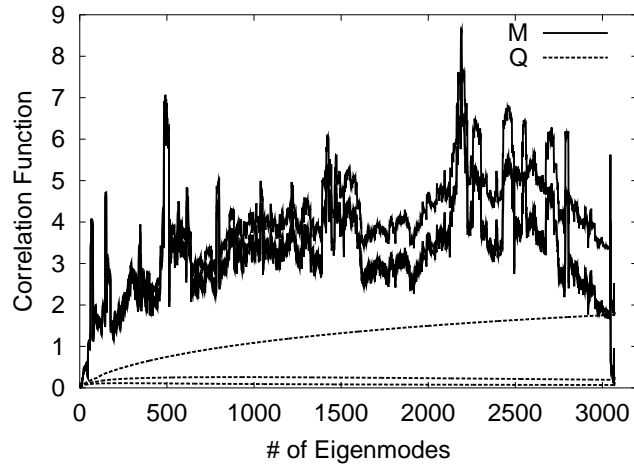


Figure 6.9: Pion correlation function from TEA for  $M$  and  $Q$  on a quenched  $4^4$  lattice at  $\beta = 5.0$ . The plot is analogous to Fig. 6.1.

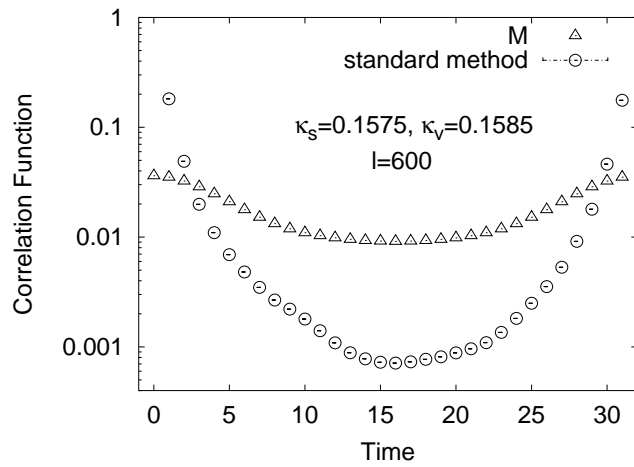


Figure 6.10: Semiquenched  $\pi$  correlation functions. One is obtained from  $M$ 's eigenmodes, the other from the standard linear solver technique.

# Chapter 7

## The $\eta'$

In this chapter the flavor singlet pseudoscalar channel with the ground state particle  $\eta'$  will be considered. At first it will be described why the  $\eta'$  plays a role of particular importance in QCD and thus why it is an interesting object to study, followed by a lattice  $\eta'$  mass analysis, similar to the one of the last chapter.

### 7.1 The $U(1)$ problem

In the chiral limit

$$m_u = m_d = m_s = 0 , \quad (7.1)$$

the QCD Lagrangian

$$\mathcal{L} = -\frac{1}{4}F_{\mu\nu}F^{\mu\nu} + \sum_{i=1}^3 (i\bar{q}_{iL}\gamma^\mu D_\mu q_{iL} + i\bar{q}_{iR}\gamma^\mu D_\mu q_{iR}) , \quad (7.2)$$

exhibits a global

$$SU_L(3) \times SU_R(3) \times U_V(1) \times U_A(1) , \quad (7.3)$$

flavour symmetry (for three light flavours).

But since the light hadron spectrum only manifests a  $SU_V(3)$  (represented by the meson octet) and a  $U_V(1)$  (represented by the baryon number conservation) symmetry, i.e. there is no parity hadron doubling (through the symmetries  $SU_A(3)$  and  $U_A(1)$ ), it is assumed that the symmetry Eq. (7.3) is spontaneously broken

$$SU_L(3) \times SU_R(3) \rightarrow SU_V(3) , \quad (7.4)$$

and

$$U_V(1) \times U_A(1) \rightarrow U_V(1) . \quad (7.5)$$

The breaking of the  $SU(3)$  symmetry results in 8 light Goldstone bosons, namely the pseudo scalar mesons ( $\pi^{0,\pm}, K^0, \bar{K}^0, K^\pm, \eta$ ). However there is no light pseudo

scalar meson which could be identified with the Goldstone boson corresponding to the breaking of the  $U(1)$  symmetry, Eq. (7.5). There exists a particle with the right quantum numbers, the  $\eta'$ , but its mass is too large. It was shown by Weinberg [43] that if the  $\eta'$  is a Goldstone boson then its mass would have to satisfy the relation

$$m_{\eta'} \leq \sqrt{3}m_{\pi} . \quad (7.6)$$

This is apparently not true. This contradiction to the described naive symmetry analysis is called the  $U(1)$  problem.

The solution of this  $U(1)$  puzzle is connected to the ABJ anomaly Eq. (5.6) [35, 36]. It shows that the conservation of the  $U(1)$  symmetry is formally violated by the presence of the axial anomaly  $2N_f q(x)$ . 't Hooft could show [44] that nontrivial topological excitations of the vacuum (instantons) can produce a nonvanishing contribution to physical observables. This observation solves the  $U(1)$  puzzle since now the  $\eta'$  is not realized as a Goldstone boson and thus does not have to be light. It achieves its large mass from the non-trivial topology of the vacuum.

Lattice QCD, being a tool suited to study the hadronic spectrum, should in principle be able to enlighten the connection between instantons, topology and the  $\eta'$  mass. In the following it will be described what TEA can contribute to this discussion.

## 7.2 The mass analysis

As described in Eq. (6.1) the correlation function of the  $\eta'$ ,  $C_{\eta'}$ , differs from  $C_{\pi}$  by the two-loop correlator  $T$ :

$$C_{\eta'}(\Delta t) = C_{\pi}(\Delta t) - N_f T(\Delta t) , \quad (7.7)$$

with

$$T(\Delta t) = \left( \sum_{s,\alpha,a} Q^{-1}(s,t,\alpha,a; s,t,\alpha,a) \right) \times \left( \sum_{s,\alpha,a} Q^{-1}(s,t+\Delta t,\alpha,a; s,t+\Delta t,\alpha,a) \right) \quad (7.8)$$

In the following TEA's potential for the determination of  $T(\Delta t)$  will be examined. The connected part of its correlation function, i.e.  $C_{\pi}$ , will be taken from the standard analysis, i.e. from the solutions of the corresponding linear systems of equations.

### 7.2.1 The Hermitian approach

The two-loop correlator is given in Eq. (7.7). Its spectral representation for the hermitian TEA reads

$$T(\Delta t) = \sum_t \sum_i \frac{1}{\lambda_i} \frac{\langle \psi_i(t) | \psi_i(t) \rangle}{\langle \psi_i | \psi_i \rangle} \sum_j \frac{1}{\lambda_j} \frac{\langle \psi_j(t+\Delta t) | \psi_j(t+\Delta t) \rangle}{\langle \psi_j | \psi_j \rangle} , \quad (7.9)$$

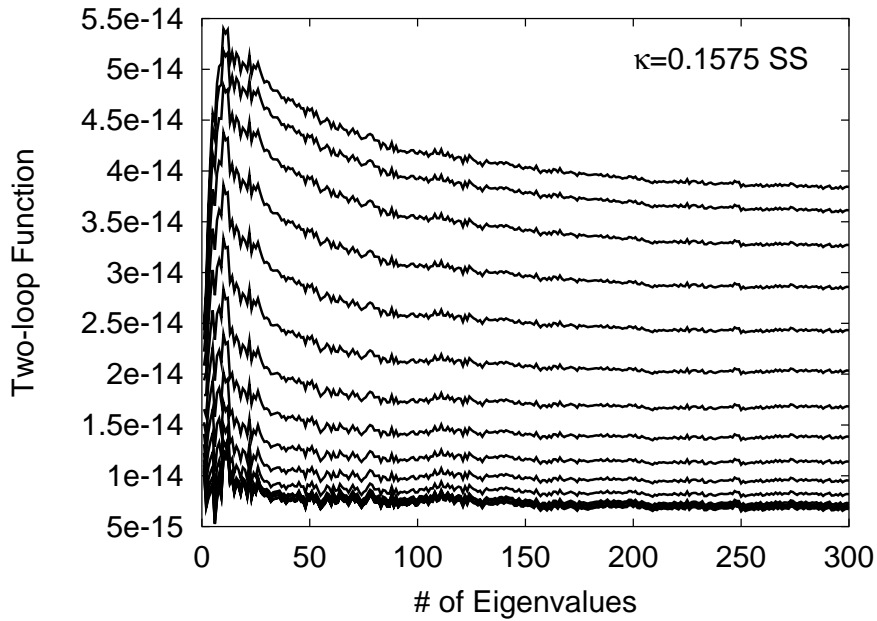


Figure 7.1: Set of two-loop functions  $T^l(\Delta t)$  on smeared sources and sinks plotted versus the cutoff  $l$ . As in Fig. 6.1,  $\Delta t$  increases as one steps down from the top curve.

where the brackets indicating the average over the gauge fields are again suppressed.

Again  $T(\Delta t)$  is summed over  $\Delta t$  in order to learn about TEA's potential in the two-loop situation

$$\sum_{\Delta t} T(\Delta t) = \left( \sum_i \frac{1}{\lambda_i} \right)^2. \quad (7.10)$$

This is just the square of the 'topological charge', see Eq. (5.14). Therefore it might be expected that TEA works as well as in section 5. In addition this shows the close relationship between the  $\eta'$  and the topological excitations of the vacuum.

The truncated two-loop correlator  $T^l$  is defined through

$$T^l(\Delta t) = \sum_t \sum_i^l \frac{1}{\lambda_i} \frac{\langle \psi_i(t) | \psi_i(t) \rangle}{\langle \psi_i | \psi_i \rangle} \sum_j^l \frac{1}{\lambda_j} \frac{\langle \psi_j(t + \Delta t) | \psi_j(t + \Delta t) \rangle}{\langle \psi_j | \psi_j \rangle}. \quad (7.11)$$

Fig. (7.1) shows the dependence of  $T^l(\Delta t)$  on the cutoff  $l$ . Contrary to the pion propagator (see Fig. (6.1)), Fig. (7.1) indeed reveals good saturation of the spectral representation by the low-lying eigenmodes over the entire  $\Delta t$ -range.

As a check for consistency the local two-loop correlators from TEA and standard SET at the light quark mass ( $\kappa = 0.1575$ ) is compared in Fig. (7.2). They are seen to agree very well within their errors, only that the TEA data show a much smoother behaviour in  $\Delta t$ . Additional smearing for SET diminishes those fluctuations. It can be seen that TEA and SET data bear errors of equal size. This is an independent

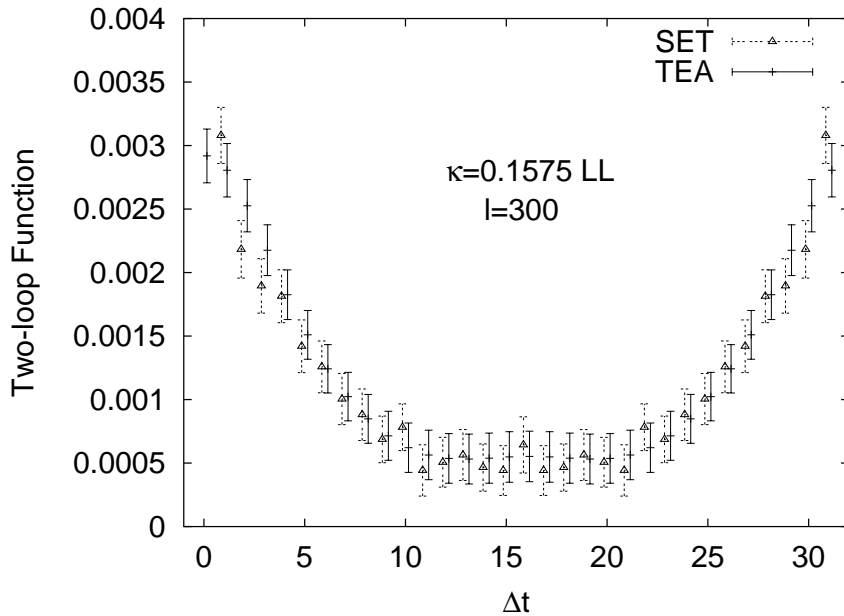


Figure 7.2: Two-loop correlator (Eq. 7.9), estimated with TEA and SET, for the lightest quark mass and local sources and sinks.

confirmation of previous claims that the errors on the  $\eta'$  mass from state of the art SET analyses are dominated by gauge field noise [10, 45].

Next the more stringent test is considered: local effective  $\eta'$ -masses. According to Eq. (7.7), the  $\eta'$ -propagator is the difference of one- and two-loop correlators,  $C_\pi$  and  $T$ . The ground state contribution to the former,  $C_\pi^g$ , can be determined very accurately by the standard methods (by iterative solvers) known from the octet spectrum [2]. Hence, it appears very natural to replace the one-loop correlator by its ground state component,  $C_\pi^g(\Delta t)$ , see Eq. (6.12). It can be hoped that, in this manner, the noise of the  $\eta'$  signal can be significantly reduced. Since the small time slices are then free of excited pion contributions, the mass fits could start at smaller time slices. Thus the problem of a vanishing signal for large time slices, which is due to the fact that the  $\eta'$  is the numerical difference between a connected and a disconnected piece, could be eluded.

Therefore it is suggested to perform a ‘one-loop groundstate analysis’ (OLGA) by the extraction of local masses,  $m_{\eta'}(\Delta t)$ , from the combination

$$\tilde{C}_{\eta'}(\Delta t) = C_\pi^g(\Delta t) - N_f T(\Delta t). \quad (7.12)$$

The results are presented in Fig. (7.3), both for the lightest and heaviest sea quark masses of SESAM, with and without smearing. A striking plateau formation from the very first time slice onwards is found.

To see the difference to the standard  $\eta'$  mass analysis, using  $C_\pi$ , in Fig. (7.4) the corresponding local effective  $\eta'$  masses are plotted. It can be seen, that in this

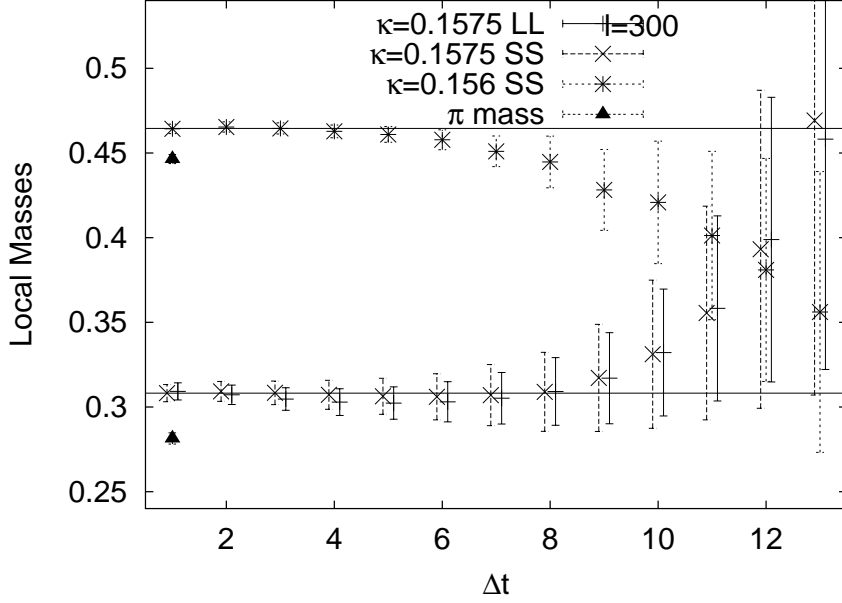


Figure 7.3: Local  $\eta'$  masses from TEA on local (LL) and smeared (SS) sources and sinks with ground state projection of its connected piece (OLGA). For comparison the  $\pi$  mass as obtained from the standard method is plotted.

situation the detection of a mass plateau is very difficult.

As a consistency check and first test of the synthetic data approach, Eq. (7.12), the local effective OLGA masses from TEA and SET in Fig. (7.5) are compared. The data points are seen to agree very well with each other, the TEA points being slightly less fluctuating. The horizontal lines in Fig. (7.3) and Fig. (7.5) refer to the fitted plateau values for the  $\eta'$  masses.

To corroborate the proposition that the OLGA mass plateaus give the lattice  $\eta'$  masses, in Fig. (7.6), Fig. (7.9) and Fig. (7.10) the OLGA masses as derived from SET on SESAM and T $\chi$ L lattices for 5 different quark masses are displayed. It can be seen that all show a plateau formation and thus support OLGA. In addition it should be noted that the statistical accuracy is sufficient to discriminate the flavour non-singlet pseudoscalar mass very well from the singlet one.

As yet another test on systematic errors – again for local and smeared wave functions and the lightest and heaviest quark masses – the dependence of the local masses  $m_{\eta'}(\Delta t)$  from TEA on the spectral cutoff  $l$  is plotted in Fig. (7.7). It appears that the systematic errors from this cutoff are well under control, once the spectral representation is truncated with  $l \simeq 150$  and higher. Furthermore the data appear to support the idea that TEA improves when decreasing the quark mass.

Finally the question, to what extent the  $\eta'$  mass is influenced by the topological content of the configurations is addressed. By applying the cuts in  $Q$ , the gauge field ensemble for the two  $\kappa$ -values are subdivided into two subsets each, with  $Q$  deter-

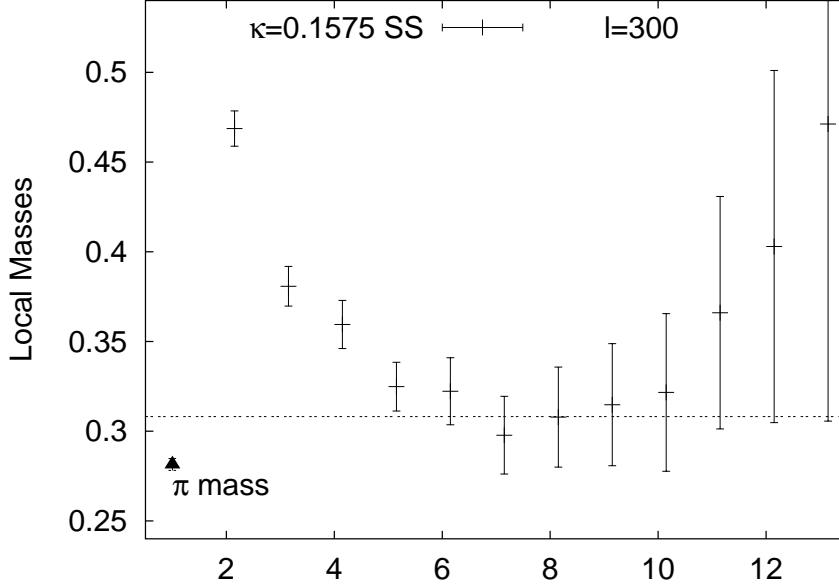


Figure 7.4: Local  $\eta'$  masses from TEA, employing  $C_\pi$  on smeared (SS) sources and sinks *without* ground state projection of its connected piece. For comparison the  $\pi$  mass as obtained from the standard method is plotted.

mined as described in section 5. The cuts are chosen such that each subset consists of about 100 configurations. The results from OLGA can be seen in Fig. (7.8). They clearly confirm the previous finding [10, 39], that topologically non-trivial gauge configurations are the origin for the large  $\eta'$  mass [46, 47].

## 7.2.2 Chiral extrapolation of the lattice $\eta'$ masses

In this section the  $\eta'$  OLGA masses will be extrapolated to quark mass zero, where the TEA and stochastic estimator data on the SESAM and T $\chi$ L lattices ( $24^3 \times 40$ ), as described in Table (7.1), will be employed. The masses will be derived from a single cosh fit to the correlation function of the  $\eta'$ . This is followed by an extrapolation of the resulting data to quark mass zero. It is assumed that either  $m_{\eta'}$  or  $m_{\eta'}^2$  to be linear in the quark mass.

The fitted lattice  $\eta'$ -masses for SET and TEA together with the fit ranges are listed in Table (7.2). There is perfect agreement between the SET and TEA data.

The lattice  $\eta'$  mass values are translated to physical units by employing the lattice spacing

$$a_\rho^{-1}(\kappa_{light}) = 2.302(64)\text{GeV} \quad (7.13)$$

as derived from a SESAM light spectrum analysis. The critical and physical light quark values are

$$\kappa_c = 0.158507(44) , \kappa_{light} = 0.158462(42) . \quad (7.14)$$

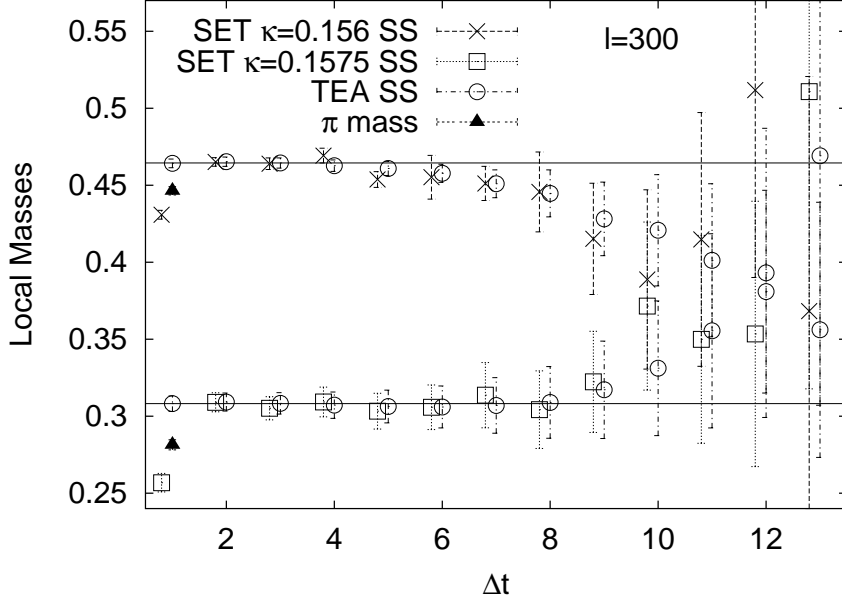


Figure 7.5: Comparison of the local OLGA  $\eta'$  masses from TEA and from Stochastic Estimations on smeared sources and sinks.

The chiral extrapolation is performed along  $\kappa_{sea} = \kappa_{val}$ , both for  $m_{\eta'}$  and  $m_{\eta'}^2$  linear in the quark mass, as illustrated in Fig. (7.11), Fig. (7.12) and Table (7.3). The fits favour the dependence  $m^2 = c + c'm_q$  from the  $\chi^2/d.o.f.$  in Table (7.3).

The physical  $\eta'$  mass value has to be translated from the three flavour world to the SESAM and T $\chi$ L simulations with its two flavours. This can be done by making use of the experimental mass splitting between flavour singlet and non-singlet states

$$M_{0;N_f=3}^2 = M_{\eta';N_f=3}^2 - (2M_K^2 - M_\eta^2) \quad (7.15)$$

and the Witten-Veneziano formula

$$M_0^2 = 2N_f\chi/F_\pi^2. \quad (7.16)$$

For  $N_f = 2$  all non-singlet masses are degenerate. Hence the above equations translate to

$$M_{\eta';N_f=2}^2 = 2/3M_{0;N_f=3}^2 + M_\pi^2 \quad (7.17)$$

The factor 2/3 stems from the flavour dependence of  $M_0$ , as shown in Eq. (7.16). Insertion of the physical mass values on the right hand side of Eq. (7.17) leads to the two flavour  $\eta'$  mass

$$M_{\eta';N_f=2} = 715\text{MeV}. \quad (7.18)$$

By inspection of Table (7.3) we find that (at the SESAM and T $\chi$ L lattice spacing) the linear (in quark mass) chiral extrapolations of both  $m_{\eta'}$  and  $m_{\eta'}^2$  are definitely above the pion mass, yet significantly below the two-flavour pseudoexperimental value estimated in Eq. (7.18).

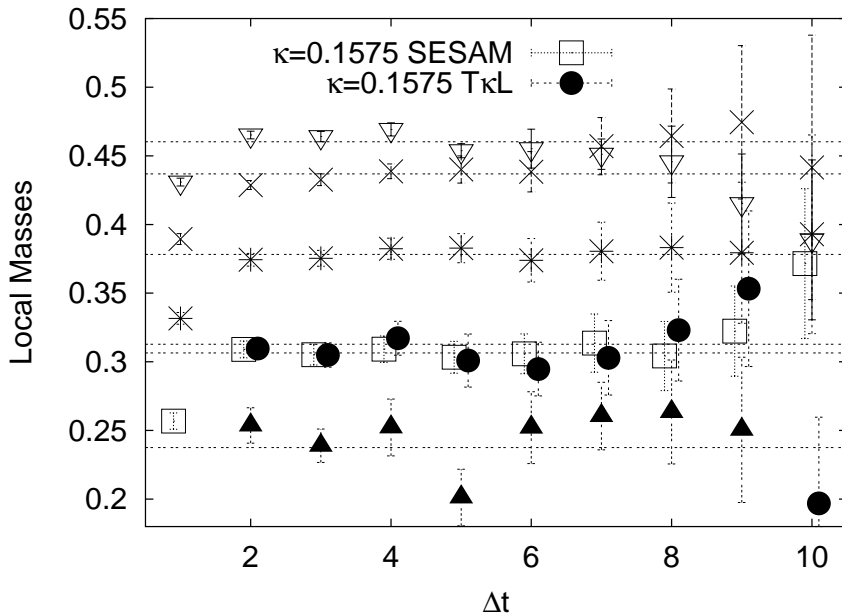


Figure 7.6: Mass plateaus from SET, top down for  $\kappa = 0.156$  S,  $0.1565$  S,  $0.157$  S,  $0.1575$  S and T,  $0.158$  T, where S stands for SESAM and T for  $T\chi L$ . The horizontal lines show the fitted mass values.

In spite of this findings the main point here is that the statistical errors of the loop contributions are well under control. This then leads to an 14 % statistical accuracy of the chirally extrapolated  $\eta'$  mass.

It can only be hoped that future  $N_f = 3$  lattice simulation will hopefully reproduce the large experimental  $\eta'$  mass.

For a nice summary of other lattice efforts in this direction see [48]

### 7.3 The non-Hermitian approach

In Fig. (7.13) and Fig. (7.14) the twoloop function  $T(\Delta t)$ , both for the Hermitian and non-Hermitian TEA, are displayed. The Hermitian case again employs 300 low-lying eigenmodes whereas the non-Hermitian one uses 600 (see Fig. (5.12)). It appears that the Hermitian case again provides the more reliable results as its dependence on the cutoff  $l$  is very stable. Surprisingly the real eigenmodes of  $M$  alone do not account for a good approximation of  $T(\Delta t)$ , in spite of the fact that they seemed to saturate the topological charge.

These results again indicate that the Hermitian TEA provides the much more reliable approximation and thus was the right choice.

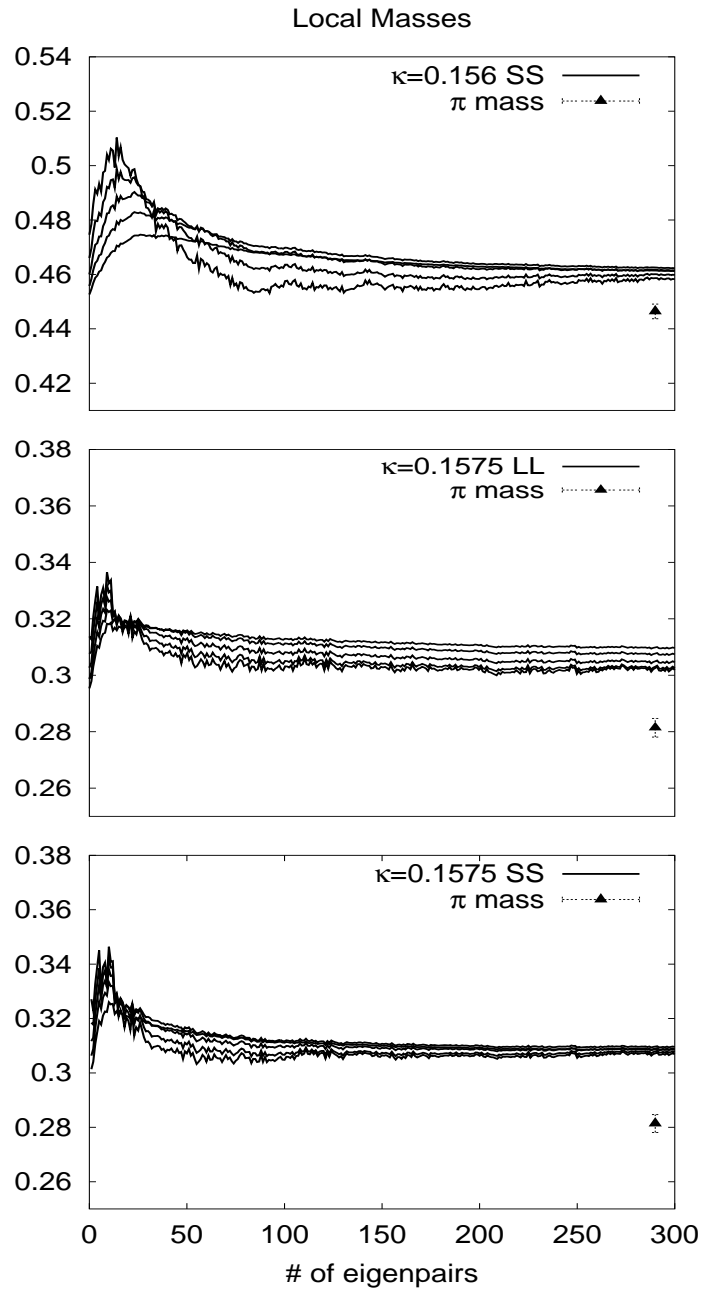


Figure 7.7: Dependence of the local  $\eta'$  masses  $m(\Delta t)$  for  $\Delta t = 1, 2, \dots, 5$  on the spectral cutoff.

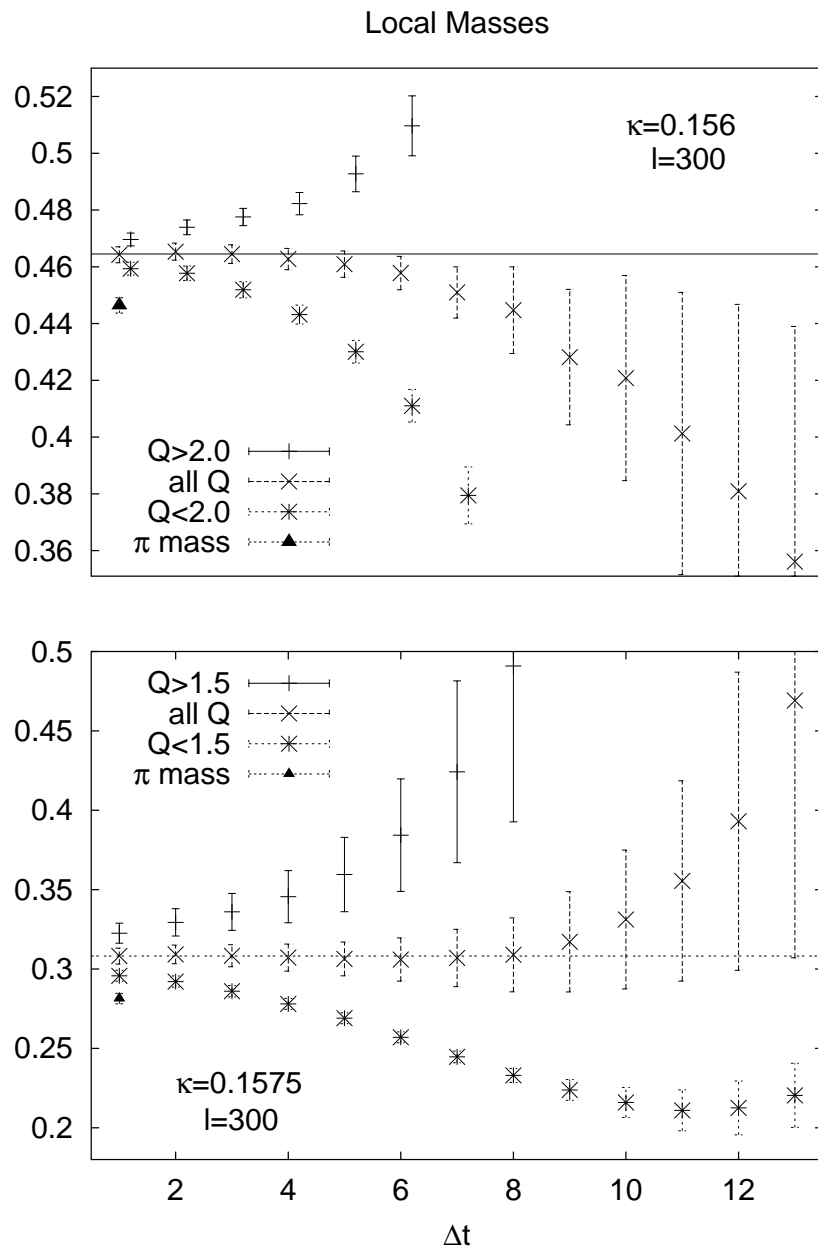


Figure 7.8: Dependence of the local OLGA  $\eta'$  mass on the topological charge work similarly well for the lightest and heaviest sea quark mass of SESAM.

Table 7.1: Simulation parameters used at  $\beta = 5.6$ . SS denotes smeared sources and sinks.  $N_{est}$  and  $N_{em}$  denotes the number of stochastic sources and eigenmodes respectively.  $N_{conf}$  are the number of decorrelated configurations.

$\kappa_{sea}$	$m_\pi/m_\rho$	lattice size	method	$N_{est}, N_{em}$	$N_{conf}$
0.1560	0.834(3)	$16^3 \times 32$	SET SS	400	195
0.1565	0.813(9)	$16^3 \times 32$	SET SS	400	200
0.1570	0.763(6)	$16^3 \times 32$	SET SS	400	200
0.1575	0.692(10)	$16^3 \times 32$	SET SS	400	200
0.1575	0.704(5)	$24^3 \times 40$	SET SS	100	180
0.1580	0.574(13)	$24^3 \times 40$	SET SS	100	155
0.1560	0.834(3)	$16^3 \times 32$	TEA SS	300	195
0.1575	0.692(10)	$16^3 \times 32$	TEA SS	300	200

Table 7.2: Fit ranges and local effective  $\eta'$  masses

$\kappa_{sea}$	method	lattice size	$m_{\eta'}$ -fit	$m_{\eta'}$
0.1560	SET SS	$16^3 \times 32$	2-4	0.4648(29)
0.1565	SET SS	$16^3 \times 32$	2-6	0.0.4326(39)
0.1570	SET SS	$16^3 \times 32$	2-10	0.3775(72)
0.1575	SET SS	$16^3 \times 32$	2-8	0.3071(87)
0.1575	SET SS	$24^3 \times 40$	2-8	0.3068(69)
0.1580	SET SS	$24^3 \times 40$	2-8	0.2414(115)
0.1560	TEA SS	$16^3 \times 32$	1-4	0.4645(28)
0.1575	TEA SS	$16^3 \times 32$	1-8	0.3080(70)

Table 7.3: Chiral extrapolation of the lattice  $\eta'$  masses. The errors stem from a  $\chi$  square fit to the measured  $\eta'$  masses.

Fit	$m_{\eta'}$	$M_{\eta'}[\text{MeV}]$	$\chi^2/d.o.f.$
$m$ -fit	0.214(7)	493(30)	5.6
$m^2$ -fit	0.138(15)	318(43)	2.2

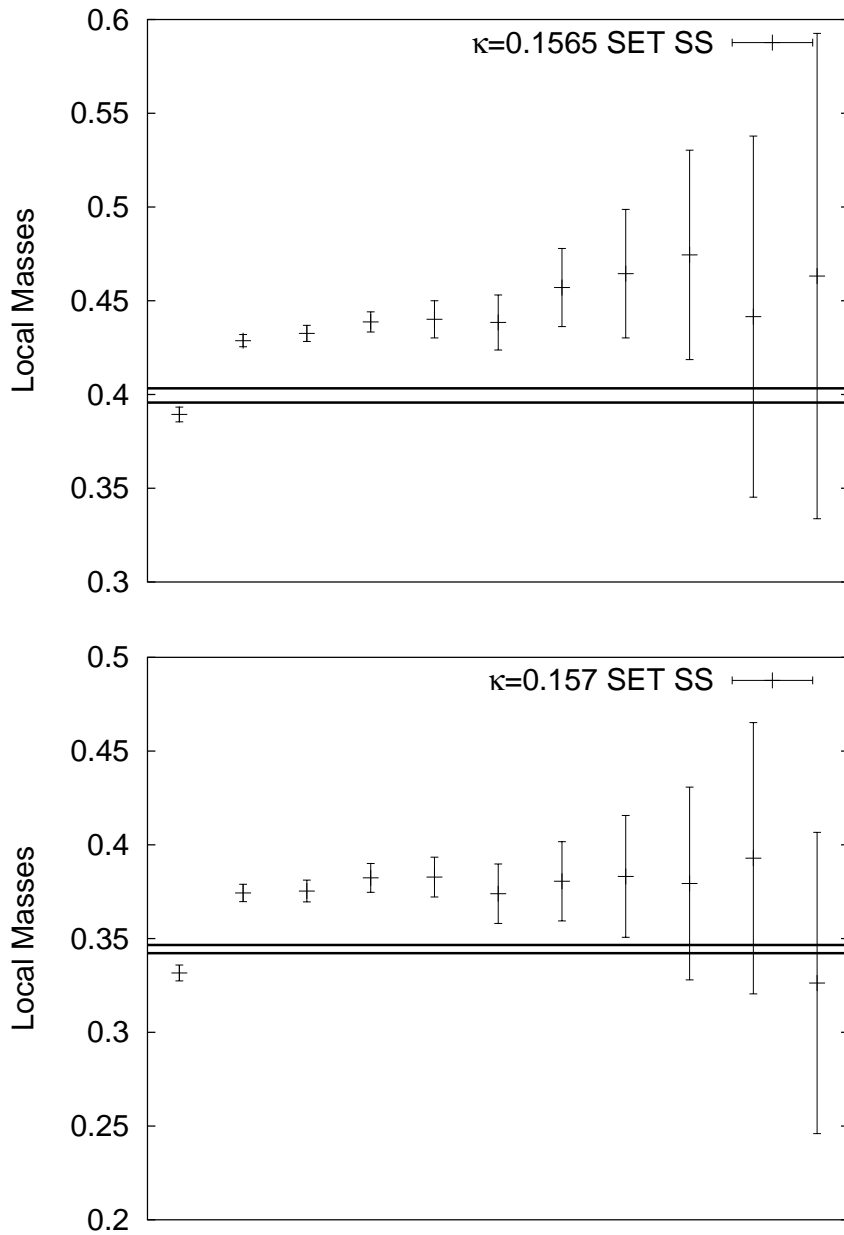


Figure 7.9: OLGA  $\eta'$  masses as derived from the stochastic estimator for smeared sinks and sources on the SESAM lattice. The horizontal lines show the error bars for the  $\pi$  mass.

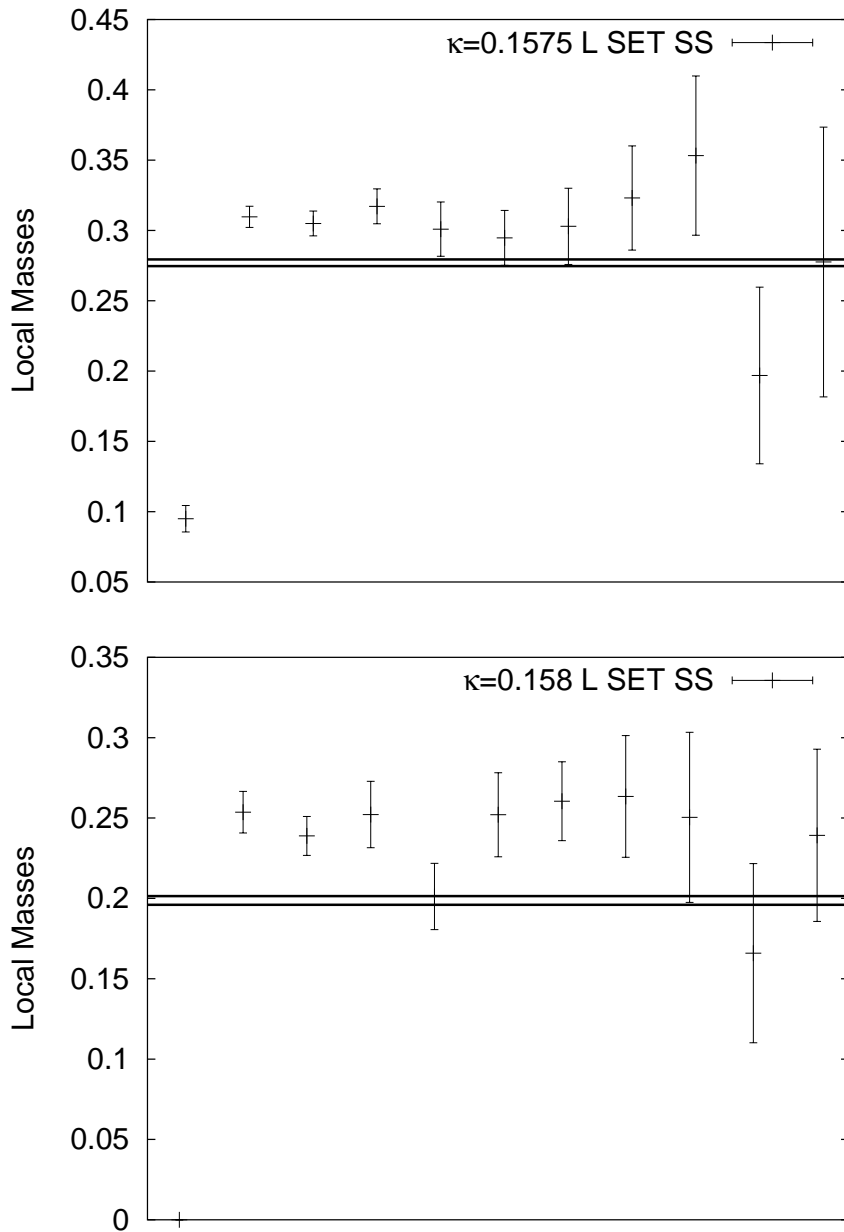


Figure 7.10: OLGA  $\eta'$  masses as derived from the stochastic estimator for smeared sinks and sources on the  $T\chi L$  lattice. The horizontal lines show the error bars for the  $\pi$  mass.

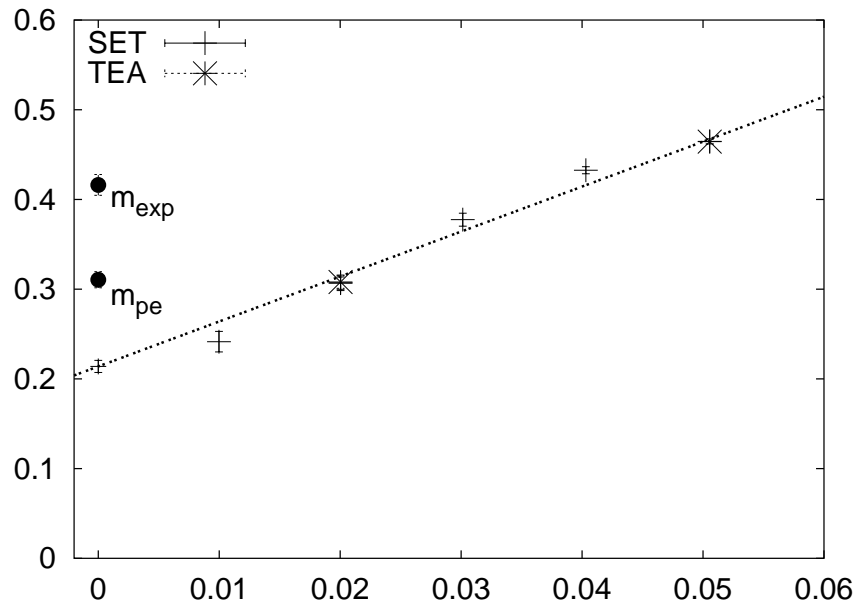


Figure 7.11: Chiral extrapolation of the  $\eta'$  masses,  $m_{\eta'}$  linear in the quark mass.

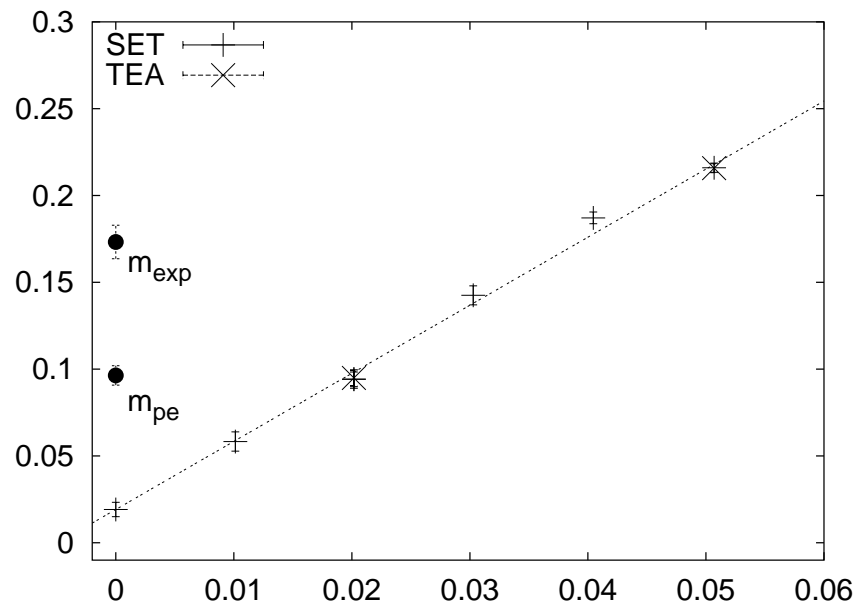


Figure 7.12: Chiral extrapolation of the  $\eta'$  masses,  $m_{\eta'}^2$  linear in the quark mass.

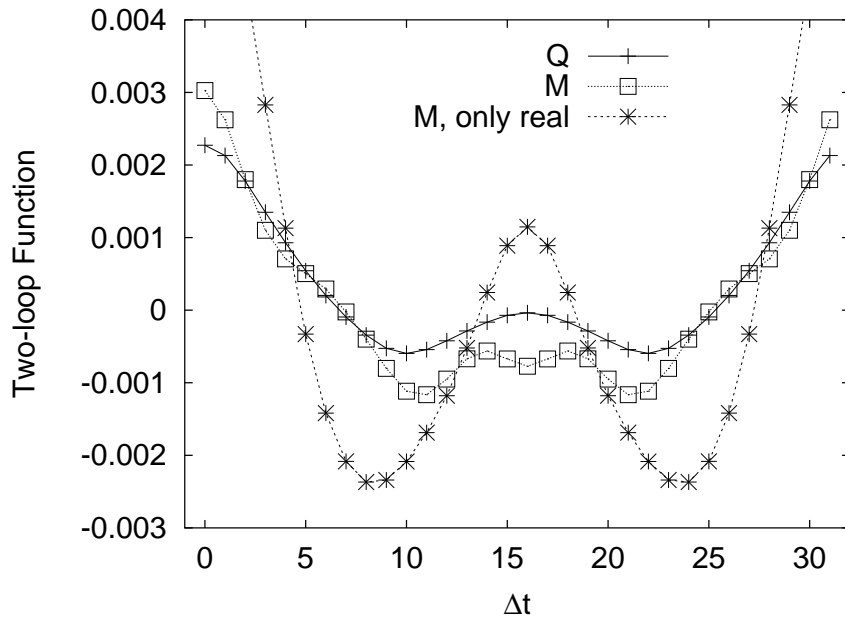


Figure 7.13: Comparison of  $T(\Delta t)$  on a single configuration for  $\kappa = 0.1575$  as provided by the Hermitian and non-Hermitian TEA.

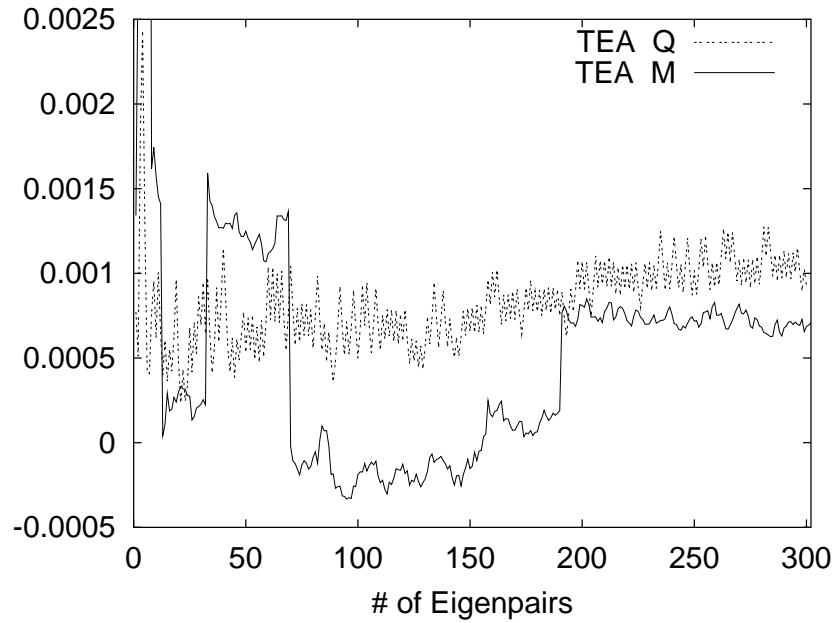


Figure 7.14: Dependence of  $T(\Delta t) = T(5)$  on the cutoff  $l$ , determined on a single configuration for  $\kappa = 0.1575$  both for the Hermitian and non-Hermitian TEA.

# Chapter 8

## Discussion and summary

In this thesis the truncated eigenmode approach (TEA) to the all-to-all propagator, i.e. the approximation of the quark propagator by low-lying Dirac eigenmodes, has been considered. It has been shown that the eigenmodes of the Hermitian Wilson-Dirac matrix  $Q$  saturate the spectral sum of  $M^{-1}$  faster, with respect to the number of eigenmodes used, than the eigenmodes of the non-Hermitian matrix  $M$ . Consequently the investigation of TEA's potential has been based on  $Q$ 's eigenmodes.

It has been demonstrated that this approach is viable in the sense that it renders satisfying results in the quark mass regime of state-of-the-art full QCD simulations like SESAM on the basis of  $\mathcal{O}(100)$  modes only. This has been verified both with respect to the topological charge and the two-loop correlator entering the  $\eta'$  propagator. Furthermore the results for the  $\pi$  correlator conveyed an impression of how TEA will perform in other cases that require an all-to-all propagator.

The required numerical effort, i.e. the number of matrix vector multiplies,  $N^{mvm}$ , per configuration in TEA compared to SET [10] for the lightest SESAM quark mass has been found to be roughly in the same ballpark. Actually the ratio  $N_{TEA}^{mvm}/N_{SET}^{mvm} \simeq 1.5$  when 300 stochastic source vectors and 300 eigenmodes were used. This is promising for future simulations employing lighter quark masses. The reason is, that the Arnoldi method does not lose efficiency when entering deeper into the chiral regime, in contrast to Krylov solvers used within stochastic estimator algorithms which suffer in convergence rate.

The concepts and improvements introduced in this thesis are

- A new and simple polynomial acceleration technique for an efficient determination of the low-lying eigenmodes of  $M$ . The acceleration factor obtained has been, on typical lattice sizes, at least of the order of 10. This method has been successfully employed in [24].
- The tuning of the Chebyshev polynomial acceleration used to calculate the eigenmodes of  $Q$ . In the space of the tuning parameters, a window of maximal rate of convergence has been located.

- A proper ordering and subsequent partial summation of  $Q$ 's eigenvalues which achieved cancellations from positive and negative eigenvalues. In this way the bulk of the higher mode contributions were shown to vanish. This led to an early onset of saturation for  $\text{Tr } Q^{-1}$  and thus to its precise determination.
- For the case of the  $\eta'$ , a ground state projection of the connected piece of the propagator. This resulted in an early plateau formation of the local masses and thus to a considerable error reduction in the  $\eta'$  mass analysis.

Addressing now TEA's prospects. What are the options to proceed?

One question concerns the improvement of TEA by estimating  $M^{-1}$  in the subspace orthogonal to the one spanned by the calculated eigenmodes. This can be done, either by the stochastic estimator technique or by improving the trace representation by use of hopping parameter expansions. This is currently under investigation and the results will appear in a forthcoming paper.

Furthermore, there are projects under way which will investigate TEA's potential for other cases that require the all-to-all propagator, namely the flavor singlet axial coupling of the proton [49] and the string breaking [50].

# Appendix A

## Eigenvalues and Eigenvectors

### A.1 The Definition of Eigenmodes

Let  $A$  be a linear map

$$A: \mathbb{C}^n \rightarrow \mathbb{C}^n, \quad (\text{A.1})$$

i.e.  $A \in \mathbb{C}^{n \times n}$ . A number  $\lambda \in \mathbb{C}$  is called eigenvalue of  $A$ , if there exists a vector  $|\psi\rangle \neq 0 \in \mathbb{C}^n$  such that

$$A|\psi\rangle = \lambda|\psi\rangle. \quad (\text{A.2})$$

Then  $|\psi\rangle$  is called eigenvector of  $A$ , corresponding to the eigenvalue  $\lambda$ . The pair  $(\lambda, |\psi\rangle)$  is referred to as an eigenmode of  $A$ .

An equivalent characterization of eigenmodes can be found by a simple transformation of Eq. (A.2)

$$(A - \lambda I)|\psi\rangle = 0. \quad (\text{A.3})$$

This shows that  $\lambda$  is an eigenvalue of  $A$  *iff* the linear system (A.3) has a solution  $|\psi\rangle \neq 0$ . This is the case *iff*  $\det(A - \lambda I) = 0$ . It follows that the eigenvalues of  $A$  are the zeros of the polynomial  $p(x) = \det(A - xI)$ .

An important conclusion from this line of reasoning is that for  $\dim(A) = n \geq 5$  eigenmode algorithms are necessarily numerical. This follows directly from the Galois theory which shows that the zeros of polynomials of degree larger than 5 cannot be calculated algebraically.

### A.2 Left and Right Eigenvectors

Let the eigenvectors of  $A$  be the columns of a matrix  $S$

$$S \equiv [|\psi_1\rangle, |\psi_2\rangle, \dots, |\psi_n\rangle]. \quad (\text{A.4})$$

Defining a matrix  $\Lambda$  with the corresponding eigenvalues on the diagonal

$$\Lambda = \text{diag} [\lambda_1, \lambda_2, \dots, \lambda_n] , \quad (\text{A.5})$$

the following equation holds

$$A S = S \Lambda . \quad (\text{A.6})$$

Apparently

$$S^{-1} A = \Lambda S^{-1} \quad (\text{A.7})$$

holds as well. This is again an eigenmode equation. The rows of  $S^{-1}$  are called  $A$ 's left eigenvectors. To be distinguishable, the above defined eigenvectors are then called right eigenvectors.

Let the rows of  $S^{-1}$  be denoted by  $\langle \phi_i |$ , i.e.

$$S^{-1} = \begin{bmatrix} \langle \phi_1 | \\ \langle \phi_2 | \\ \vdots \\ \langle \phi_n | \end{bmatrix} , \quad (\text{A.8})$$

and

$$\langle \phi_i | A = \lambda_i \langle \phi_i | . \quad (\text{A.9})$$

It follows directly from  $S^{-1}S = I$  that  $\langle \phi_i |$  and  $|\psi_i\rangle$  form a biorthogonal system

$$\langle \phi_i | \psi_j \rangle = \delta_{ij} . \quad (\text{A.10})$$

### A.3 Normal Matrices

A matrix  $A$  that satisfies the commutativity relation

$$A^\dagger A = A A^\dagger \quad (\text{A.11})$$

is called normal. The importance of this definition is based on Schur's matrix decomposition, which shows that normal matrices are diagonalizable by unitary transformations

$$U^{-1} A U = U^\dagger A U = \Lambda , \quad (\text{A.12})$$

with  $U^{-1} = U^\dagger$ .

Since the rows of  $U^\dagger$  and the columns of  $U$  are the left and right eigenvectors of  $A$ , it follows that

$$\langle \phi_i | = |\psi_i\rangle^\dagger . \quad (\text{A.13})$$

This means that the left and right eigenvectors are equal. It is then obvious that the following orthogonality relations hold

$$\langle \phi_i | \phi_j \rangle = \delta_{ij} , \quad (\text{A.14})$$

$$\langle \psi_i | \psi_j \rangle = \delta_{ij} , \quad (\text{A.15})$$

i.e. that the eigenvectors of normal matrices are orthogonal.

## A.4 Eigenmodes and Matrix Inversion

Let  $A \in \mathbb{C}^{n \times n}$  be invertible, i.e.  $A^{-1}A = AA^{-1} = I$ . What is the relationship between the eigenmodes of  $A$  and  $A^{-1}$ ?

Since

$$1 = \det I = \det(A^{-1}A) = \det A^{-1} \det A \quad (\text{A.16})$$

and

$$\det A = \lambda_1 \lambda_2 \cdots \lambda_n \quad (\text{A.17})$$

the eigenvalues of  $A$  are all different from 0. It follows then directly from (A.2) that

$$A^{-1}|\psi\rangle = \frac{1}{\lambda}|\psi\rangle. \quad (\text{A.18})$$

Thus the eigenvectors of  $A$  and  $A^{-1}$  are equal and the eigenvalues of  $A^{-1}$  are the inverses of  $A$ 's eigenvalues.

## A.5 Eigenmodes and Polynomial Transformations

Algorithms that determine eigenmodes of a matrix  $A$  can often be accelerated by polynomial transformations. This means that the algorithm determines eigenmodes of  $p(A)$ , where  $p$  is a polynomial, instead of  $A$ 's. This brings up the question of the relation between the eigenmodes of  $A$  and  $p(A)$ .

Multiplying equation (A.2) with  $A$  from the left gives

$$A^2|\psi\rangle = \lambda A|\psi\rangle = \lambda^2|\psi\rangle. \quad (\text{A.19})$$

It follows easily that

$$p(A)|\psi\rangle = p(\lambda)|\psi\rangle, \quad (\text{A.20})$$

holds as well. Since the eigenvectors of  $A$  and  $p(A)$  are equal, the eigenvalues of  $A$  can be derived from the Rayleigh quotient

$$\lambda = \frac{\langle \psi | A | \psi \rangle}{\langle \psi | \psi \rangle}. \quad (\text{A.21})$$

## A.6 Spectral Decompositions

Functions  $f$  of a matrix  $A$  can be defined through spectral representations. For this

the biorthogonality of the left  $|\phi_i\rangle$  and right  $|\psi_i\rangle$  eigenvectors is a crucial property

$$f(A) = \sum_i f(\lambda_i) \frac{|\psi_i\rangle\langle\phi_i|}{\langle\phi_i|\psi_i\rangle}. \quad (\text{A.22})$$

Two examples are

$$A = \sum_i \lambda_i \frac{|\psi_i\rangle\langle\phi_i|}{\langle\phi_i|\psi_i\rangle}, \quad (\text{A.23})$$

$$A^{-1} = \sum_i \frac{1}{\lambda_i} \frac{|\psi_i\rangle\langle\phi_i|}{\langle\phi_i|\psi_i\rangle}. \quad (\text{A.24})$$

Later extensive use of the spectral representation of  $A^{-1}$  will be made.

# Appendix B

## The Lanczos/Arnoldi Algorithm

The Lanczos method is used to determine a few of the largest and/or smallest eigenmodes of large, sparse and symmetric matrices. The Arnoldi algorithm is its counterpart for the unsymmetric case. The method will be described by means of the real symmetric case (real Lanczos), but the ideas generalize easily to complex and unsymmetric matrices.

### B.1 The Basic Idea

The problem to determine a few of the largest and/or smallest eigenmodes of a large and sparse symmetric matrix  $A \in \mathbb{R}^{n \times n}$  is to reduce its dimension  $n$  by projecting it orthogonally onto small subspaces  $U_k \subseteq \mathbb{R}^n$ , with  $k \ll n$ . This dimensional reduction turns  $A$  into being a small and dense matrix  $T_k$ . The eigenmodes of  $T_k$  can then be calculated by applying the standard  $QR$  algorithm. The reason why this algorithm is not directly applied to  $A$  is, that it determines the entire set of eigenmodes, what limits, through computer storage requirements and execution time, the dimension of the matrices treatable in this way.

Apparently the above procedure only makes sense, if the eigenmodes of the small matrices  $T_k$  carry information about the eigenmodes of the large matrix  $A$ . In other words the eigenvalues of  $T_k$  should be estimates for the eigenvalues of  $A$  and the corresponding eigenvectors of  $A$  should be constructible from the eigenvectors of  $T_k$ . This will be merely the case if the subspaces  $U_k$  are chosen in an appropriate way. There are different algorithms which differ in the way those subspaces are created, whereas the Lanczos/Arnoldi algorithm employs the Krylov subspaces.

### B.2 The Krylov Subspace

The  $k$ -dimensional Krylov subspace of a symmetric matrix  $A$ , corresponding to a

starting vector  $q$ , is defined through

$$\mathcal{K}(A, q, k) = \text{span}\{q, Aq, \dots, A^{k-1}q\}. \quad (\text{B.1})$$

Let  $q_1, q_2, \dots, q_k$  be an orthonormal basis of  $\mathcal{K}(A, q, k)$ , i.e.

$$\text{span}\{q, Aq, \dots, A^{k-1}q\} = \text{span}\{q_1, q_2, \dots, q_k\}, \quad (\text{B.2})$$

and

$$\langle q_i | q_j \rangle = \delta_{ij}. \quad (\text{B.3})$$

The orthogonal projection of  $A$  onto  $\mathcal{K}(A; q; k)$  is then defined through

$$T_k = Q_k^T A Q_k, \quad (\text{B.4})$$

where  $Q_k = [q_1, q_2, \dots, q_k] \in \mathbb{R}^{n \times k}$ .

The reason for the Krylov subspaces being a good choice for the eigenmode algorithm can be understood by considering the optimization of the Rayleigh quotient.

### B.3 The Rayleigh Quotient or why does the Lanczos Method work

The Rayleigh quotient  $R$  of  $A$  is defined through the *expectation value*

$$R(q) = \frac{q^T A q}{q^T q} \quad \text{with } q \neq 0. \quad (\text{B.5})$$

One can show that

**Theorem 1 (Minimax Theorem)**

$$\lambda_1(A) = \max_{q \neq 0} [R(q)], \quad (\text{B.6})$$

$$\lambda_n(A) = \min_{q \neq 0} [R(q)], \quad (\text{B.7})$$

where the eigenvalues are ordered according to  $\lambda_1 \geq \lambda_2 \dots \geq \lambda_n$  (the eigenvalues are real since  $A$  was assumed to be symmetric).

If  $q$  is constrained to a particular subspace  $U_k \subseteq \mathbb{R}^n$  it follows directly that

$$\{R(q) | q \in U_k\} \subseteq [\lambda_n(A), \lambda_1(A)]. \quad (\text{B.8})$$

Choosing for  $U_k$  the Krylov subspace  $\mathcal{K}(A; q; k)$ , Eq. (B.8) translates to

$$\lambda_1(A) \geq \lambda_1(T_k) \geq \lambda_2(T_k) \geq \dots \geq \lambda_{k-1}(T_k) \geq \lambda_k(T_k) \geq \lambda_n(A), \quad (\text{B.9})$$

where  $T_k$  was defined in Eq. (B.4).  $\lambda_k(T_k)$  denotes the smallest eigenvalue of  $T_k$ .

As stated above the largest eigenvalue  $\lambda_1(T_k)$  of the small matrix  $T_k$  is supposed to be an estimate for the largest eigenvalue  $\lambda_1(A)$  of the large matrix  $A$ , i.e. one wishes for

$$\lambda_1(T_k) \rightarrow \lambda_1(A) , \quad (\text{B.10})$$

as one increases  $k$ .

How can the dimension of the subspace  $\mathcal{K}(A; q; k)$  be increased such that the largest eigenvalue  $\lambda_1$  becomes a better estimate for  $\lambda_1(A)$ .

Let  $x$  be a vector linear independent of  $q_1, q_2, \dots, q_k$  and  $S_{k+1}$  the orthogonal projection of  $A$  onto  $\text{span}\{q_1, q_2, \dots, q_k, x\}$ . It follows then from Eq. (B.8) that

$$\lambda_1(S_{k+1}) \geq \lambda_1(T_k) . \quad (\text{B.11})$$

Therefore any choice of a linear independent vector  $x$  will in general help to achieve a better estimate for  $\lambda_1(A)$ , but what is the optimal choice for  $x$  ?

To see this a further consequence of the minimax theorem has to be used, namely that there actually exists a vector  $u_k \in \mathcal{K}(A; q; k)$  such that

$$R(u_k) = \lambda_1(T_k) . \quad (\text{B.12})$$

Since  $R(u_k)$  increases most rapidly in the direction of its gradient  $\nabla$ ,  $x$  is chosen such that  $\nabla R(u_k) \in \text{span}\{q_1, q_2, \dots, q_k, x\}$ . It follows from

$$\nabla R(u_k) = \frac{2}{u_k^T u_k} (A u_k - R(u_k) u_k) , \quad (\text{B.13})$$

that  $\nabla R(u_k)$  is a linear combination of  $A u_k$  and  $u_k$ . Therefore  $x$  has to satisfy the relation

$$x \in \text{span}\{q_1, q_2, \dots, q_k, A u_k\} . \quad (\text{B.14})$$

But since  $\text{span}\{q_1, q_2, \dots, q_k, A u_k\}$  is nothing but the  $(k+1)$ -dimensional Krylov subspace, corresponding to the starting vector  $q$ , Eq. (B.14) reads

$$x \in \mathcal{K}(A; q; k+1) . \quad (\text{B.15})$$

This means that with respect to the gradient the Krylov subspaces are the optimal subspace choice to be employed in an eigenmode algorithm. (The last statements only hold if  $A u_k$  is linearly independent of  $\text{span}\{q_1, q_2, \dots, q_k\}$ . If this is not the case one is faced with an invariant subspace on which one could directly determine the eigenmodes via the  $QR$  algorithm.)

The Lanczos algorithm then works as follows: One chooses a starting vector  $q$ , generates the Krylov subspaces of increasing dimension, i.e.  $\mathcal{K}(A; q; 1)$ ,  $\mathcal{K}(A; q; 2)$ ,  $\dots$ , projects the large matrix orthogonally onto those subspaces and determines the eigenmodes of the small matrices with the  $QR$  algorithm. The size of the Krylov subspaces is increased till convergence is found.

The only thing then left to do is to create the orthonormal bases for the Krylov subspaces which are required for the orthogonal projections.

Since there exists a vector,  $v_k$ , such that  $R(v_k) = \lambda_k(T_k)$  and since  $R(v_k)$  decreases most rapidly in the direction of  $-\nabla R(v_k)$ , which is again an element of  $\mathcal{K}(A; q; k+1)$ , good approximates for both the largest and the smallest eigenvalue of  $A$  are included in the spectra of the  $T_k$ s.

To see how the eigenvectors of  $A$  can be constructed from the eigenvectors of  $T_k$  a matrix  $N_k$  that diagonalizes  $T_k$  has to be introduced, i.e.

$$\Lambda_k = N_k^T T_k N_k . \quad (\text{B.16})$$

It follows directly that

$$\Lambda_k = (Q_k N_k)^T A Q_k N_k . \quad (\text{B.17})$$

It can be shown that the columns of  $Q_k N_k$  converge towards the eigenvectors of  $A$ .

## B.4 Orthonormal Bases for the Krylov Subspaces

Suppose that  $Q = [q_1, q_2, \dots, q_n]$  is orthogonal, with  $q_1, q_2, \dots, q_n$  chosen such that  $\text{span}\{q_1, q_2\} = \text{span}\{q_1, Aq_1\}$ ,  $\text{span}\{q_1, q_2, q_3\} = \text{span}\{q_1, Aq_1, A^2q_1\}$ , etc. It follows that

$$T_n = Q^T A Q \quad (\text{B.18})$$

is a tridiagonal matrix, i.e.

$$T_n = \begin{pmatrix} \alpha_1 & \beta_1 & \cdots & 0 \\ \beta_1 & \alpha_2 & \ddots & \vdots \\ \vdots & \ddots & \ddots & \beta_{n-1} \\ 0 & \cdots & \beta_{n-1} & \alpha_n \end{pmatrix} . \quad (\text{B.19})$$

Column by column  $QT_n = AQ$  reads

$$Aq_k = \beta_{k-1}q_{k-1} + \alpha_kq_k + \beta_kq_{k+1} . \quad (\text{B.20})$$

The line of reasoning can now be reversed, namely the last equation can be turned into an algorithm that determines the columns of  $Q$ :

```

 $r_0 = q_1; \beta_0 = 1; q_0 = 0; k = 0$ 
while( $\beta_k \neq 0$ )
     $q_{k+1} = r_k / \beta_k$ 
     $k = k + 1$ 
     $\alpha_k = q_k^T A q_k$ 
     $r_k = (A - \alpha_k I) q_k - \beta_{k-1} q_{k-1}$ 
     $\beta_k = \|r_k\|_2$ 
end

```

It follows directly that the Lanczos iteration after  $k$ -steps takes the form

$$AQ_k = Q_k T_k + r_k e_k^T . \quad (\text{B.21})$$

This is also called a length- $k$  Lanczos factorization.

## B.5 The Implicitly Restarted Lanczos/Arnoldi Method

In actual numerical calculations the memory size limits the dimension of the Krylov subspaces. But what if the eigenvalue estimates are still poor even though the iteration has reached the critical subspace dimension? The way out of this problem is to restart the iteration with a new starting vector. To achieve progress of convergence the new starting vector has to be *better* than the old one.

If for example the largest eigenvalue of  $A$  is searched for, then the iteration can be restarted with the new starting vector  $q_{new} = Q_k N_k e_1$  (see Eq. (B.17)), where  $Q_k N_k e_1$  is the estimate for the eigenvector corresponding to the estimate for the largest eigenvalue of  $A$ .

Or if the  $l$  largest eigenvalues are wanted and the restart is done with a Krylov subspace of size  $k > l$ , the new starting vector can be chosen to be  $q_{new} = \sum_{i=1}^l Q_k N_k e_i$ .

The implicitly restarted Lanczos/Arnoldi method is an advancement of the restarting idea. It not only determines a new starting vector  $q_{new}$  but also creates the corresponding Krylov subspace of dimension  $l$ , where  $l$  is the number of eigenmodes searched for, without performing any matrix vector multiplications involving  $A$ . In other words the Krylov subspace  $\mathcal{K}(A, q_{new}, l)$  is directly constructed from  $\mathcal{K}(A, q, k)$ . Therefore, compared to normal restarting, in each restarting step  $l$  matrix vector multiplications with  $A$  are saved.

The way implicit restarting works will be described in the remainder of this section.

Assume that one wants to determine  $l$  eigenvalues of  $A$ . The Lanczos factorization after  $k$  steps was given in Eq. (B.21), with  $k > l$ .

The set of eigenvalues  $\{\mu_1, \mu_2, \dots, \mu_k\}$  of  $T_k$  is now divided into a wanted  $S_w$  and an unwanted part  $S_u$

$$S_u = \{\mu_1, \mu_2, \dots, \mu_{k-l}\} \quad , \quad (\text{B.22})$$

$$S_w = \{\mu_{k-l+1}, \dots, \mu_k\} \quad , \quad (\text{B.23})$$

where the wanted part consists of  $l$  eigenvalues. A  $QR$  iteration with shifts is then applied to  $T_k$  in the following way:

$$T^{(1)} = T_k \quad (\text{B.24})$$

for  $i = 1, k-l$

$$T^{(i)} - \mu_i I = V_i R_i$$

$$T^{(i+1)} = R_i V_i + \mu_i I$$

end

$$T^+ = T^{k-l+1}$$

With

$$T^{(1)} - \mu_1 I = V_1 R_1 \quad , \quad (\text{B.25})$$

it follows that

$$V_1^T T^{(1)} - \mu_1 V_1^T = R_1 \quad , \quad (\text{B.26})$$

and

$$T^{(2)} = V_1^T T^{(1)} V_1 \quad . \quad (\text{B.27})$$

Hence  $T^+$  can be derived from  $T_k$  in the following way

$$T^+ = V^T T_k V \quad , \quad (\text{B.28})$$

with  $V = V_1 V_2 \dots V_{k-l}$ .

Defining  $Q^+ \equiv Q_k V$ , Eq. (B.21) takes the form

$$AQ^+ = Q^+ T^+ + r e_k^T V \quad . \quad (\text{B.29})$$

It follows directly from Eq. (B.24) that  $T^+$  is tridiagonal and that in the last row of  $V$  the first  $l$  entries are zero. A consequence of this is that the first  $l$  columns of (B.29) form a new length- $l$  Lanczos factorization

$$AQ^+(\cdot : \cdot, 1 : l) = Q^+ T^+(\cdot : \cdot, 1 : l) + r e_l^T v_{kl} \quad . \quad (\text{B.30})$$

This shows that the  $l$ -dimensional Krylov subspace  $\mathcal{K}(A, q_{new}, l)$  can indeed be constructed from  $\mathcal{K}(A, q, k)$  without any matrix vector multiplications involving  $A$ .

It remains to be shown that the new starting vector  $q_{new}$  is *better* than  $q$ , i.e. that  $q_{new}$  is close to the subspace  $\text{span}\{Q_k N_k e_{k-l+1}, Q_k N_k e_{k-l+2}, \dots, Q_k N_k e_k\}$  ( $N_k$  was defined in Eq. (B.17)).

The new starting vector  $q_{new}$  can be found in the first column of  $Q^+(\cdot : \cdot, 1 : l)$

$$Q^+(\cdot : \cdot, 1) = Q_k V e_1 \quad (\text{B.31})$$

$$= Q_k V_1 V_2 \cdots V_{k-l} e_1 \quad (\text{B.32})$$

$$= \alpha Q_k V_1 V_2 \cdots V_{k-l} R_{k-l} \cdots R_2 R_1 e_1 \quad (\text{B.33})$$

$$= \alpha Q_k (T_k - \mu_{k-l} I) \cdots (T_k - \mu_1 I) e_1 \quad (\text{B.34})$$

$$= \alpha (A - \mu_{k-l} I) \cdots (A - \mu_1 I) Q_k e_1 \quad (\text{B.35})$$

The last equation follows from (B.21) and the fact that  $e_k^T p(T_k) e_1 = 0$  for any polynomial  $p$  of degree  $k - l - 1$  or less. The new starting vector is obtained from

$$q_{new} = (A - \mu_{k-l} I) \cdots (A - \mu_1 I) q = p(A) q \quad (\text{B.36})$$

The roots of  $p(A)$  suppress the unwanted vectors  $Q_k N_k e_1, Q_k N_k e_2, \dots, Q_k N_k e_{k-l}$ . Thus  $q_{new}$  has the required property.

# Appendix C

## Gamma convention

For the  $\gamma$  matrices the following convention is used:

$$\gamma_1 = \begin{pmatrix} 0 & 0 & 0 & i \\ 0 & 0 & i & 0 \\ 0 & -i & 0 & 0 \\ -i & 0 & 0 & 0 \end{pmatrix} \quad (\text{C.1})$$

$$\gamma_2 = \begin{pmatrix} 0 & 0 & 0 & 1 \\ 0 & 0 & -1 & 0 \\ 0 & -1 & 0 & 0 \\ 1 & 0 & 0 & 0 \end{pmatrix} \quad (\text{C.2})$$

$$\gamma_3 = \begin{pmatrix} 0 & 0 & i & 0 \\ 0 & 0 & 0 & -i \\ -i & 0 & 0 & 0 \\ 0 & i & 0 & 0 \end{pmatrix} \quad (\text{C.3})$$

$$\gamma_4 = \begin{pmatrix} 1 & 0 & 0 & 0 \\ 0 & 1 & 0 & 0 \\ 0 & 0 & -1 & 0 \\ 0 & 0 & 0 & -1 \end{pmatrix} \quad (\text{C.4})$$

$$\gamma_5 = \begin{pmatrix} 0 & 0 & 1 & 0 \\ 0 & 0 & 0 & 1 \\ 1 & 0 & 0 & 0 \\ 0 & 1 & 0 & 0 \end{pmatrix} \quad (\text{C.5})$$

# Appendix D

## Properties of the Dirac matrices

- Minkowskian Dirac matrix:

1.  $\gamma_5 D \gamma_5 = -D$
2. Symmetry:  $\lambda^D \leftrightarrow -\lambda^D$ ,  $|\psi^D\rangle \leftrightarrow \gamma_5 |\psi^D\rangle$

- Euclidean Dirac matrix

1.  $\gamma_5 D \gamma_5 = D^\dagger = -D$
2.  $\gamma_5 M \gamma_5 = M^\dagger$
3. Symmetry:  $\lambda^D \leftrightarrow -\lambda^D \Leftrightarrow \lambda^D \leftrightarrow (\lambda^D)^*$ , ( $\lambda^D$  purely imaginary),  $|\psi^D\rangle \leftrightarrow \gamma_5 |\psi^D\rangle$
4. Symmetry:  $\lambda^M \leftrightarrow (\lambda^M)^*$
5. orthogonal eigenvectors  $|\psi^D\rangle, |\psi^M\rangle$ .
6. Hermitian matrix  $Q \equiv \gamma_5 M$

- Wilson Dirac matrix

1.  $\gamma_5 D \gamma_5 = D^\dagger$
2.  $\gamma_5 M \gamma_5 = M^\dagger$
3. Symmetry:  $\lambda^D \leftrightarrow -\lambda^D \leftrightarrow (\lambda^D)^* \leftrightarrow -(\lambda^D)^*$
4. Symmetry:  $\lambda^M \leftrightarrow (\lambda^M)^*$
5. right and corresponding orthogonal left eigenvectors:  $|\psi_i\rangle \leftrightarrow \langle \psi_{\bar{i}} | \gamma_5$
6. Hermitian matrix  $Q \equiv \gamma_5 M$

# Acknowledgments

First I would like to thank Prof. Dr. K. Schilling for suggesting this project and accompanying it with lively interest.

Furthermore, I wish to express my gratitude to Dr. Dr. Th. Lippert for his ideas and contributions to this project and especially for his constant support and motivation.

I am very grateful to Prof. J. W. Negele and Prof. R. Brower for the fruitful discussions, especially during my visit at the Massachusetts Institute of Technology.

The bulk of computations for this project was carried out at NIC/Jülich and NERSC/Livermore. I thank the staff of both centers for their support.

Many thanks go to all the actual and former members of the Wuppertal lattice working group for various reasons, be it discussions, support, system administration or the support of the ALiCE cluster system. In alphabetical order: Guido Arnold, Gunnar Bali, Christoph Best, Norbert Eicker, Stephan Güsken, Ivan Hip, Thomas Moschny, Boris Orth, Antonios Tsapalis, Wolfram Schroers, Achim Spitz, Thorsten Struckmann, Peer Ueberholz and Jochen Viehoff.

Furthermore I wish to thank H. Frank, S. Hoffmann and A. Wied for helping with all the bureaucratic procedures.

Finally, I want to express my gratitude to my dearest Ceci for her support and patience over the entire time.

# Bibliography

- [1] F. Jegerlehner et al., ECFA preprint ECFA/99/200 (1999).
- [2] SESAM, N. Eicker et al., Phys. Rev. D59 (1999) 014509, hep-lat/9806027.
- [3] A. Frommer, Nucl. Phys. Proc. Suppl. 53 (1997) 120, hep-lat/9608074.
- [4] UKQCD, C. McNeile and C. Michael, Phys. Rev. D63 (2001) 114503, hep-lat/0010019.
- [5] UKQCD, C. Michael and J. Peisa, Nucl. Phys. Proc. Suppl. 60A (1998) 55, hep-lat/9705013.
- [6] M. Okawa, Nucl. Phys. Proc. Suppl. 47 (1996) 160, hep-lat/9510047.
- [7] SESAM, S. Güsken et al., Phys. Rev. D59 (1999) 114502, hep-lat/9901009.
- [8] CP-PACS, A.A. Khan et al., Nucl. Phys. Proc. Suppl. 83 (2000) 162, hep-lat/9909045.
- [9] UKQCD, C. Michael and P. Pennanen, Phys. Rev. D60 (1999) 054012, hep-lat/9901007.
- [10] SESAM, T. Struckmann et al., Phys. Rev. D63 (2001) 074503, hep-lat/0010005.
- [11] K. Bitar et al., Nucl. Phys. B313 (1989) 348.
- [12] S.J. Dong, J.F. Lagae and K.F. Liu, Phys. Rev. Lett. 75 (1995) 2096, hep-ph/9502334.
- [13] SESAM, N. Eicker et al., Phys. Lett. B389 (1996) 720.
- [14] W. Wilcox, Numerical Challenges in Lattice Quantum Chromodynamics, edited by A. Frommer et al., Lecture Notes in Computational Science and Engineering, Springer Verlag, Heidelberg, 1999, hep-lat/9911013, Proceedings of the International Workshop, University of Wuppertal, August 22-24, 1999.
- [15] SESAM, J. Viehoff et al., Lattice '97, edited by C.T.H. Davies et al., Nucl. Phys. B (Proc. Suppl.) Vol. 63, pp. 269–271, North-Holland, Amsterdam, The Netherlands, 1998, Proceedings of the XVth International Symposium on Lattice Field Theory, Edinburgh, Scotland, July 22-26, 1997.

- [16] T.L. Ivanenko and J.W. Negele, Nucl. Phys. Proc. Suppl. 63 (1998) 504, hep-lat/9709130.
- [17] I.M. Barbour et al., The Recursion Method and its Applications, Solid State Sciences Vol. 58 (Springer, Berlin, Heidelberg, New York, 1985), 149.
- [18] R. Setoodeh, C.T.H. Davies and I.M. Barbour, Phys. Lett. B213 (1988) 195.
- [19] L. Venkataraman and G. Kilcup, (1997), hep-lat/9711006.
- [20] T. DeGrand and A. Hasenfratz, (2000), hep-lat/0012021.
- [21] G.H. Golub and C.F.V. Loan, Matrix computations, 3rd ed. (Johns Hopkins Univ. Press, Baltimore, 1996).
- [22] K. Maschhoff, Parallel Arnoldi method,  
[http://www.caam.rice.edu/~kristyn/parpack\\_home.html](http://www.caam.rice.edu/~kristyn/parpack_home.html).
- [23] I. Horvath et al., (2001), hep-lat/0102003.
- [24] I. Hip et al., (2001), hep-lat/0105001.
- [25] T. DeGrand and A. Hasenfratz, (2001), hep-lat/0103002.
- [26] S.J. Dong et al., (2001), hep-lat/0110037.
- [27] R.G. Edwards and U.M. Heller, (2001), hep-lat/0105004.
- [28] G.P. Lepage, (1996), hep-lat/9607076.
- [29] G.P. Lepage, Nucl. Phys. Proc. Suppl. 47 (1996) 3, hep-lat/9510049.
- [30] K. Symanzik, Nucl. Phys. B226 (1983) 187.
- [31] B. Sheikholeslami and R. Wohlert, Nucl. Phys. B259 (1985) 572.
- [32] Y. Saad, Numerical methods for large eigenvalue problems,  
<http://www-users.cs.umn.edu/~saad/books.html>.
- [33] R. Rajaraman, An introduction to solitons and instantons in quantum field theory (North-Holland Publ. CO., 1982).
- [34] R.G. Edwards, U.M. Heller and R. Narayanan, Phys. Rev. D60 (1999) 034502, hep-lat/9901015.
- [35] J.S. Bell and R. Jackiw, Nuovo Cim. A60 (1969) 47.
- [36] S.L. Adler, Phys. Rev. 177 (1969) 2426.
- [37] M. Teper, Phys. Lett. B171 (1986) 81.
- [38] M. Garcia Perez, O. Philipsen and I.O. Stamatescu, Nucl. Phys. Proc. Suppl. 83 (2000) 541, hep-lat/9909029.
- [39] SESAM, G.S. Bali et al., (2001), hep-lat/0102002, submitted to Phys. Rev. D.
- [40] B. Allès et al., Phys. Rev. D58 (1998) 071503.

- [41] R. Narayanan, Nucl. Phys. Proc. Suppl. 73 (1999) 86, hep-lat/9810045.
- [42] S. Güsken, Nucl. Phys. Proc. Suppl. 17 (1990) 361.
- [43] S. Weinberg, Phys. Rev. D11 (1975) 3583.
- [44] G. 't Hooft, Phys. Rev. D14 (1976) 3432.
- [45] UKQCD, C. McNeile and C. Michael, Phys. Lett. B491 (2000) 123, hep-lat/0006020.
- [46] E. Witten, Nucl. Phys. B156 (1979) 269.
- [47] G. Veneziano, Nucl. Phys. B159 (1979) 213.
- [48] S. Aoki, Nucl. Phys. Proc. Suppl. 94 (2001) 3, hep-lat/0011074.
- [49] S. Gusken, (1999), hep-lat/9906034.
- [50] B. Bolder et al., Phys. Rev D (2000).